OUKA
The University of Osaka
Institutional Knowledge Archive

| | |
|---|---|
| Title | Numerical assessment of solar PV and water retentive pavement as mitigation strategies for urban heat island |
| Author(s) | Cortes, Aiza Ceniza |
| Citation | 大阪大学, 2016, 博士論文 |
| Version Type | VoR |
| URL | https://doi.org/10.18910/59609 |
| rights | |
| Note | |

*The University of Osaka Institutional Knowledge Archive : OUKA*

https://ir.library.osaka-u.ac.jp/

The University of Osaka

大阪大学
OSAKA UNIVERSITY

Doctoral Dissertation

# Numerical assessment of solar PV and water retentive pavement as mitigation strategies for urban heat island

数値モデルを用いた太陽光パネル設置と保水性舗装による
都市ヒートアイランド緩和効果の評価

Cortes Aiza Ceniza

July 2016

Division of Sustainable Energy and Environmental Engineering
Graduate School of Engineering
Osaka University
M3-5F Yamada-oka 2-1 Suita City, Osaka 565-0871 Japan

# SUMMARY

The study and understanding of urban heat island or UHI phenomenon is essential because it affects outdoor air quality, energy demand, the distribution of pollutant concentration and local meteorology. This study was conducted for two main purposes: to develop a computational fluid dynamics (CFD) model for UHI simulation and to assess UHI mitigation strategies. The CFD model was chosen over other types of simulation because of its ability to predict spatial distribution of air temperature and wind speed while taking into consideration key factors like solar radiation and sky view factor. The CFD model was parameterized using the Reynolds-averaged equations of momentum, mass continuity and heat. These equations were solved numerically on a staggered grid system utilizing finite control volume with semi-implicit method for pressure-linked equations or SIMPLE method. The building envelope model was used to calculate for the surface energy budget of buildings and weather research forecasting model was used to calculate the boundary conditions. The CFD model was applied by simulating two real cities: Osaka City and Suita City. These areas were chosen because both are major cities in Japan and exhibit a typical urban set-up.

For Osaka City, solar photovoltaic (PV) panels were assessed as mitigation strategy for UHI. In the simulation, solar PV were installed on top of building surfaces mainly the roof and wall. Under clear weather conditions, installation of solar PV caused an overall cooling of building surfaces during daytime and nighttime but specific warming occurred in relation the position of the sun. During daytime, cooling effect was greater on roof surface because

of efficient thermal convection and greater sky view factor which led to air circulation. During nighttime, cooling effect was greater on wall surface because of the shading effect. The shading effect minimized the heat absorption during daytime and hence minimized heat release during nighttime. The decrease in surface temperature eventually led to cooling of urban air. Presence of solar PV had no effect on waste heat but can potentially reduce sensible heat flux. Roof PV produce greater energy output than wall PV and under the assumption that the power generated will be used for cooling, a decrease in energy consumption can be expected.

For Suita City, water retentive pavement (WRP) made from fly ash was assessed as mitigation strategy for UHI. Prior to the assessment, a clear understanding on the heat and moisture transport in WRP must be determined and modeled.

Consequently, a one-dimensional pavement transport (PT) model was developed using conservation equations for heat and soil moisture in liquid and vapor form. Using the parameters volumetric water content, matric potential and evaporation efficiency, it was identified that the WRP exhibit cooling properties. Both surface temperature and matric potential were inversely proportional to volumetric water content. On the other hand, WRP evaporation efficiency was maximum when saturated with water. It was also proven that the thermal and hydraulic performance of WRP was better than asphalt. Despite the overestimation and underestimation during specific times of the day, the PT model can numerically evaluate the diurnal variation in surface temperature with minimal estimated error. Evaporation of water from WRP occurred first in the surface and this behavior greatly influenced temporal variation of temperature and moisture profile. The increase in latent heat flux and net radiation by WRP rendered its cooling ability. The decrease in sensible and conductive heat flux by WRP can potentially cool the surrounding environment.

The developed PT model was then coupled with CFD model. In the coupling, WRP was utilized as pavement material for main street while the rest of ground surface was asphalt. Through this simulation, it was determined that WRP can cause a decrease in ground surface temperature. This was primarily due to the evaporation of water from WRP surfaces which caused an increase in latent heat flux. The increase in latent heat flux minimized the difference between air temperature and surface temperature which led to a decrease in sensible heat flux and longwave upward radiation. Other contributing factors to the cooling of main street surface include shadowing effect, increased albedo and lower thermal conductivity. The cooling of ground surface eventually led to cooling of air temperature. Although other factors such as vortex formation also contributed to air temperature cooling, the degree of air temperature cooling was proportional to the degree of surface temperature reduction.

The accurate calculation of the CFD model proved its significant application in urban heat island simulation studies. Nevertheless, the results presented are only true to the assumptions made and to the parameters set. For future studies, the following are recommend:

a. Simulation of real cities that have different weather characteristics from Osaka and Suita City.
b. Assessment of other mitigation strategies such as the use of high albedo pavements or simulating the synergistic effect of cool pavement and increased urban vegetation
c. Lengthen the calculation period, from 24-h to several days of unsteady analysis.
d. For solar PV assessment
    - Simulation of other scenarios such as varied solar panel orientation, PV albedo and generation efficiency.
    - Evaluation of the effect of solar PV when installed in roof surface only.
    - Assimilation of the effect of reflected radiation to human comfort because the current model only considered the effect of radiation due to reflection from one surface to another.
    - Determination the effect of weather and seasonal variation such as winter.
e. For WRP assessment
    - Evaluation of different water content scenario i.e. rainfall conditions.
    - Determination of the effect of seasonal variation such as winter.

# ACKNOWLEDGEMENTS

*This dissertation would not have been possible without the support and help of numerous people.*

*I would like to express my deepest gratitude to Prof. Akira Kondo, for his incomparable kindness and guidance. He has supported me even before coming to Japan and until the end of my doctoral degree. To Prof. Hikari Shimadera, who has helped me tremendously in my academic difficulties. His teachings and wisdom in numerical simulation has improved my skills significantly. To Prof. Yoshio Inoue, for helping me with my experiments. To Tomohito Matsuo, for patiently sharing his technical knowledge with me.*

*I would also like to thank the committee members: Prof. Yoshiyuki Shimoda and Prof. Akihiro Tokai for their scientific advice and invaluable comments for this dissertation.*

*To Reika Ogino, who continually assisted me in all clerical works. To the members of the Engineering for Assessing the Sustainable Environment laboratory, for their warm company. To the Ministry of Education, Culture, Sports, Science and Technology Japan for the financial support.*

*Lastly, I would like to express my deepest appreciation to my friends and family who had supported me spiritually and emotionally. Their understanding and encouragement gave me strength every day.*

# CONTENTS

# LIST OF TABLES

# LIST OF FIGURES

# 1. INTRODUCTION

## 1.1 Urban heat island phenomenon

When an urban area has higher temperature compared with its surrounding rural area, a phenomenon called urban heat island (UHI) occurs. Figure 1 shows the process of UHI formation as a result of both mesoscale and microscale interactions. The presence of infrastructures, nature of structural surfaces, amount of vegetation, anthropogenic heat etc. (Chen *et al*., 2006; Priyadarsini *et al.*, 2008; Takahashi *et al.*, 2004) all contribute to UHI phenomenon. Among these contributing factors, the warming of urban surfaces like streets and buildings, is proven to affect UHI phenomenon the most (Asaeda & Ca, 1993; Asaeda & Ca, 1996; Asaeda & Ca, 2000; Golden & Kaloush, 2006; Oke, 1982).

Rizwan, Dennis and Lui (2008) differentiates urban heat island intensity (UHII) into two: mean UHII and maximum UHII. Mean UHII is the difference in mean temperature between urban and rural areas while maximum UHII is the difference in maximum temperature between urban and rural areas. The UHII is greater at nighttime compared with daytime, especially when the sky is clear and wind speed is weak (Jauregui, 1997; Kazimierz & Fortuniak, 1999; Montavez *et al.*, 2000). UHI is also greater during winter than in summer due to greater production of anthropogenic heat from air conditioning use (Kim & Baik, 2005; Montavez *et al*., 2000), drier air and longer nighttime which increase surface temperature (Aoyagi, Kabaya & Seino, 2012). For these reasons, the occurrence of UHI in major temperate cities has been well studied. Examples included Seoul (Kim & Baik, 2005),

Lodz (Kazimierz & Fortuniak, 1999) and Paris (Lemonsu & Masson, 2002). Likewise, occurrence of UHI in warm, tropical countries has gained consideration in the most recent years. Some researches include investigation of cities like Singapore (Chow & Roth, 2006; Priyadarsini *et al.*, 2008), Granda (Montavez *et al.*, 2000), Malaysia (Elsayed, 2012), Philippines (Macapinlac, 2011) and Mexico (Jauregui, 1997).

In Japan, the Japan Meteorological Agency (JMA) mentioned in its 'Urban Heat Island Monitoring Report 2011' that the temperature of large metropolitan areas like Kyoto, Osaka, Nagoya and Tokyo had been increasing. Extensive studies have been performed, most which focused on understanding the mechanism of UHI formation (Aoyagi *et al.*, 2012; Miyatake *et al.*, 2011; Mochida *et al.*, 1997; Ohashi *et al.*, 2007) and developing mitigation strategies. These mitigation strategies are presented and discussed in section 1.2. 3.

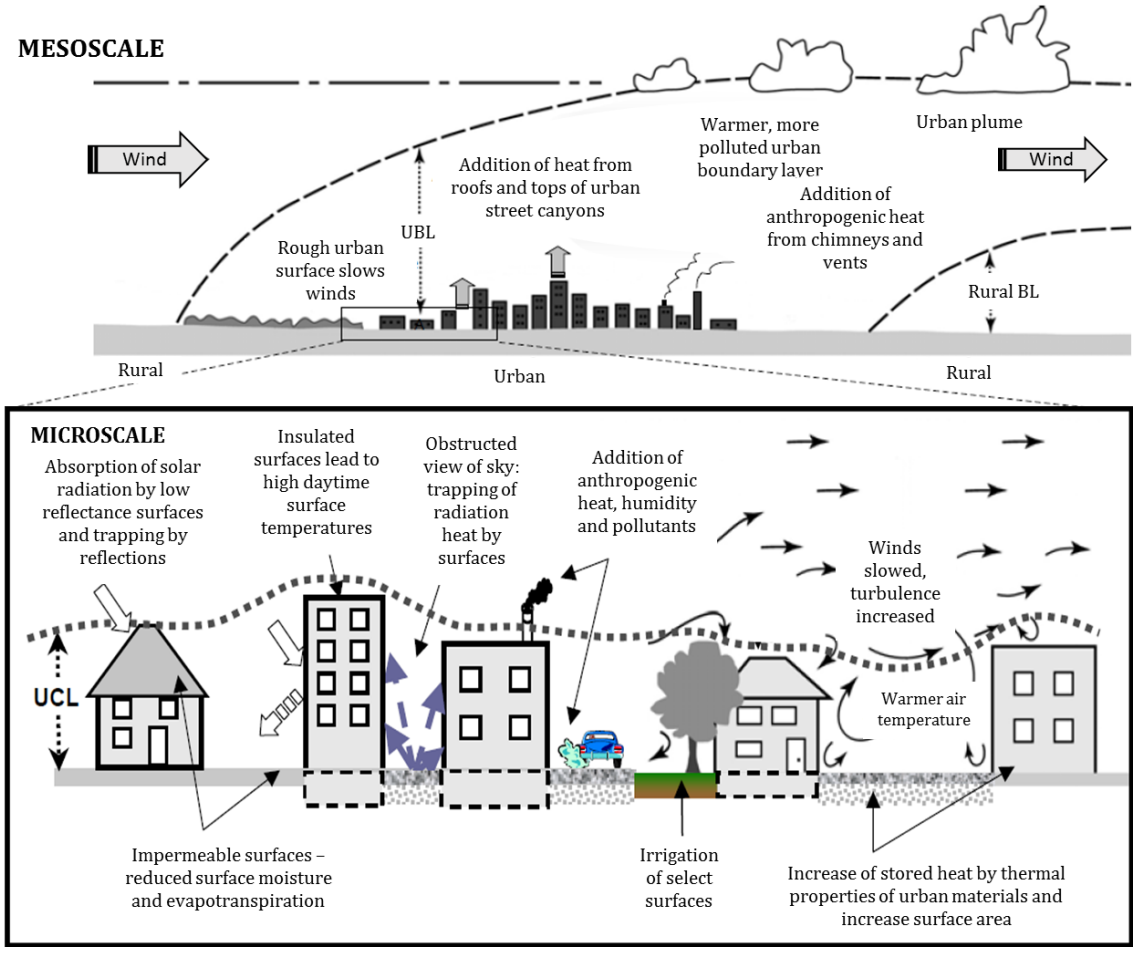


**Figure 1. The process of urban heat island adapted from Voogt (2013).**

## 1.2 Literature review

### 1.2.1 Approaches to study UHI phenomenon

Nunez and Oke (1977) recognized an urban canyon (Fig. 2) consisting of building walls and ground as the basic urban surface unit. It also contains the canyon-air volume which is the air within the canyon and the top most area forms the lower urban boundary layer (UBL).

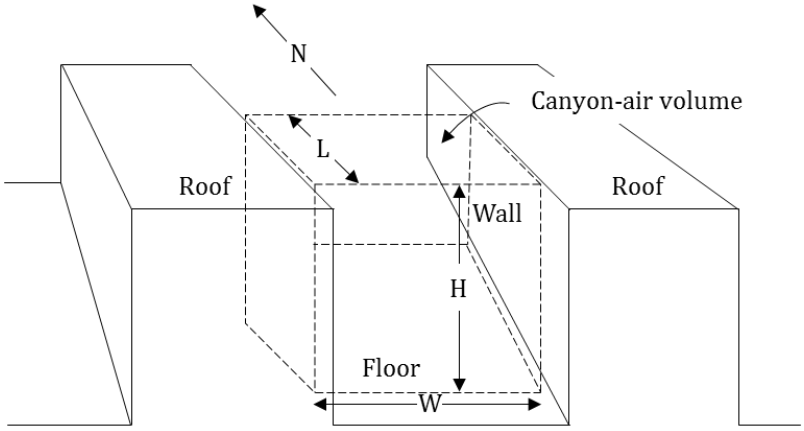


**Figure 2. Schematic diagram of urban canyon developed by Nunez and Oke (1977).**

Before discussing the parameters of urban canyon energy budget, it is important to first identify the investigative approaches to UHI phenomenon. A review by Mirzaei and Haghighat (2010) enumerated the following techniques for studying.

(a) multi-scale phenomena

In this technique, meso-scale and microscale analysis are integrated but often with discrepancies due to simplification of parameters. An example would be the significant role of Coriolis force in atmospheric interactions and thus important for meso-scale studies. However, this can be negligible in microscale analysis where anthropogenic heat release influences the system greatly.

(b) observational approaches

This technique is based on the geographical range used in studying UHI. It could either be in the form of field measurements, thermal remote sensing (Cao *et al*., 2002; Chen *et al*., 2006; Macapinlac, 2011; Voogt & Oke, 2003) and micro-scale modelling e.g. using wind tunnels. Using observation data, majority of the studies pointed that UHII is indirectly

proportional to cloud cover. This means that under clear and calm condition, UHII decreases. But this is contradictory to the study of Steinecke (1999) which Mirzaei and Haghighat (2010) attributes to weak statistical analysis.

(c) simulation methods

A computational technique that uses mathematical models to solve urban climate problems. The most common are urban canopy model (UCM) and computational fluid dynamics model (CFD) which could either be meso-scale or micro-scale. Table 1 presents a summary of these models for UHI simulation.

**Table 1. A comparison of the simulation methods for UHI obtained from Mirzaei and Haghighat (2010).**

| | Urban canopy model | CFD | |
|---|---|---|---|
| | | Meso-scale | Micro-scale |
| Maximum domain size | City | City | Building block |
| Spatial resolution | 1-10 m | 1-10 km | 1-10 m |
| Temporal resolution | Hour | Minute | Second |
| Governing equation | · Energy balance equation<br>· Surface heat conduction equation<br>· Velocity equation of the canopy layer (input assumption) | · Navier-stokes equations<br>· Monin-Obukhov for ground surface<br>· Heat conduction equation for soil | · Navier-stokes equations<br>· Monin-Obukhov for urban surface<br>· Heat conduction equation for surface |
| Limitations | · Developed velocity field from temperature and moisture<br>· Assumption of a city with similar homogenous array of buildings<br>· Limited resolution of urban geometry<br>· Advantageous for steady state solution only<br>· Atmospheric effect is neglected<br>· Empirical assumption for convective latent and sensible heat | · Roughness assumed by urban canopy layer<br>· Providing land-use land-cover database is a challenge<br>· Field measurement determines accuracy<br>· Turbulence modelling | · Exclude atmospheric phenomena<br>· Creating database for canopy details is challenging<br>· Providing boundary conditions<br>· Turbulence modelling |

### 1.2.2 Parameters

The parameters used for the approaches mentioned above were mainly based from the energetic basis of UHI. Deriving from the study of urban canyon, Nunez and Oke (1977) expressed it as:

$$Q_R + Q_{ant} = Q_H + Q_L + \Delta Q_S + \Delta Q_A \tag{1}$$

where $Q_R$ is the net radiation, $Q_{ant}$ is anthropogenic heat, $Q_H$ is sensible heat flux, $Q_L$ is latent heat flux, $\Delta Q_S$ net storage heat flux and $Q_A$ is the net advection. Therefore, the energy balance within the city is dependent on these parameters.

(a) Latent heat flux

This parameter, commonly used in UCM and CFD (Mirzaei & Haghighat, 2010), is obtained from solving moisture and velocity equations predicted by the Monin-Obukhov Similarity Theory (MOST).

$$Q_L = \ell \rho_a B C_H (q_s - q_a) \tag{2}$$

where is $\ell$ the latent heat of vaporization, $\rho_a$ is air density, $B$ is the wetness parameter of the canopy surface, $C_H$ is the local bulk transfer coefficient, $q_s$ is the saturated specific humidity for a given surface temperature and $q_a$ is the specific humidity.

(b) Sensible heat flux

Similar to the latent heat flux, this parameter can also be obtained through MOST. It is expressed in Eq. (3) and the heat exchange in and out of the canyon-air volume is shown in Fig. 3.

$$Q_H = \alpha (T_s - T_a), \qquad \alpha = \begin{cases} 6.15 + 4.18 U_a & u \le 5 \ m/s \\ 7.51 u_a^{0.78} & u > 5 \ m/s \end{cases} \tag{3}$$

where $T_s$ is the surface temperature, $T_a$ is the air temperature and $u$ is the wind velocity at a reference height $z$.

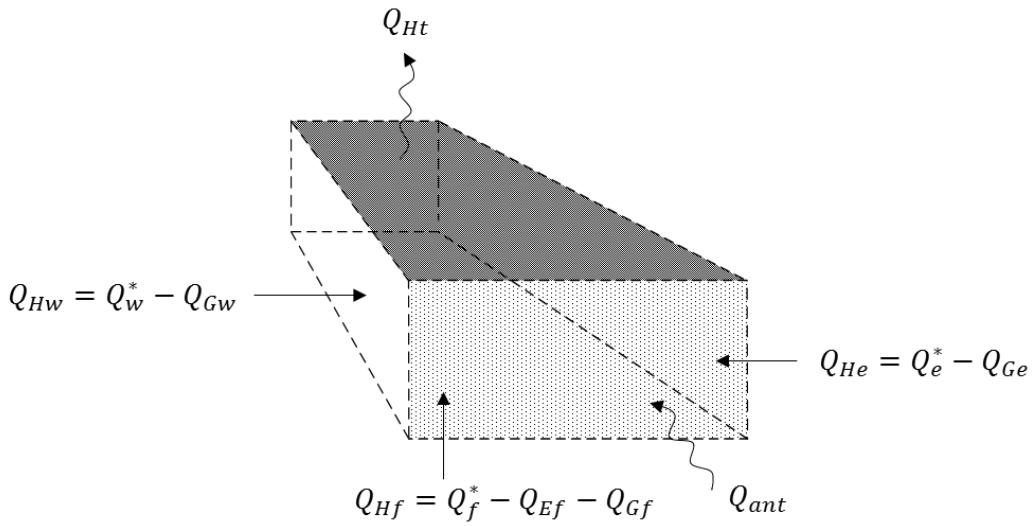


**Figure 3. Heat exchange in the canyon-air volume (Nunez & Oke, 1977).**

(c) Anthropogenic heat

This parameter is obtained by adding sink or source terms such as heat from vehicles ($Q_V$), stationary sources ($Q_{SS}$) and metabolism ($Q_M$) as shown in Eq. (4).

$$Q_{ant} = Q_V + Q_{SS} + Q_M \tag{4}$$

(d) Storage heat flux

Heat conduction in urban areas occurs in soil, pavement and infrastructure materials. Mirzaei and Haghighat (2010) used UCM and dynamic numerical models to obtain the heat diffusion equation and temperature distribution inside surfaces:

$$\rho_s c_p \frac{\partial T}{\partial t} = Q_{Gen} + \nabla \cdot (K \nabla T) \tag{5}$$

where $\rho_s$ is the soil density, $c_p$ is the surface heat capacity, $Q_{Gen}$ is the heat source and $k$ is the thermal conductivity.

(e) Radiation

While urban surfaces partly absorb shortwave radiation, some also reflect it. Moreover, incident solar radiation is also composed of diffused and directed fractions. Tracing of

reflected direct and diffused solar radiation is typically obtained by calculating the sky view factor for each surface. Other than shortwave radiation, longwave must also be considered which is more dominant in nocturnal UHI formation.

(f) Boundary conditions

Surface layer roughness is affected by the profile of wind flow, temperature and humidity over the city topography. And these profile over the urban canyon are within the surface layer of the planetary boundary layer. Mirzaei and Haghighat (2010) identified five types of boundary conditions: inflow boundary condition, outflow boundary condition, ground and soil boundary condition, building surface boundary condition and top-canopy and later boundary conditions.

### 1.2.3 Mitigation strategies

The growing public concern on health and the environmental risks due to UHI have made the development of mitigation strategies an imperative. The most common UHI mitigation strategies are greenification, evaporative cooling, use of "cool" materials and employment of bioclimatic design.

(a) Greenification

This is perhaps the most widely used and one of the most effective among all of the mitigation strategies enumerated above. It involves planting and increasing vegetation in urban areas through creation of parks and gardens (Onishi *et al.*, 2010; Wang, Berardi & Akbari, 2015; Zhou & Shepherd, 2010). This method reduces air temperature by increasing latent heat flux through evo-transpiration. The opposite of UHI, a phenomenon called negative urban heat island or cool island has also been recognized (Shigeta, Ohashi & Tsukamoto, 2009) and its occurrence is closely associated to the influence of urban greenification (Chang, Li & Chang, 2007; Mendocan, 2009).

(b) Evaporative cooling

Evaporative cooling happens when water evaporates from surfaces of inland water bodies e.g. ponds and rivers (Tominaga, Sato, & Sadohara 2015). It is important to note that evaporative cooling can also come from water retentive urban surfaces (discussed in Chapter 4). Similar to greenification, latent heat flux is also increased in this method.

(c) Cool materials

Cool materials are either building roof (Costanzo, Evola & Marletta, 2015; Lie, Bou-Zeid & Oppenheimer, 2014; Wang, Berardi & Akbari, 2015) or pavement surfaces (Dimoudi *et al*., 2014; Wang, Berardi & Akbari, 2015) which have high albedo rating. When materials have high albedo, the amount of solar radiation absorbed through building envelopes and urban structures is reduced (Taha, 1997).

(d) Bioclimatic design and ventilation

This strategy involves improvement of building orientation and wind path design to allow urban ventilation (Hathway & Sharples, 2012; He *et al.*, 2014; Kolokotroni, Giannitsaris & Watkins, 2006; Stavrakakis *et al*., 2012; Zoras *et al*., 2014).

In Japan, mitigation strategies are implemented both in national and local levels. The policy framework by Japanese Inter-Ministry Coordination Committee (Ministry of Environment, 2004) enumerates three pillars of counter measures to reduce UHI namely: reducing anthropogenic heat, improving urban surface and improving urban structure. Reduction of anthropogenic heat can be done by improving the efficiency of energy consuming equipment, traffic control measures like diffusion of low emission vehicles and encouragement of new energy. The improvement of urban surface includes greenification by tree planting to increase evo-transpiration and encourage low temperature rise of the ground. Lastly, improvement of urban structures by linking parks, rivers and roads.

Furthermore, the Bureau of the Environment in Tokyo (2005) has also released the guidelines for heat island control measures. Figure 4 shows specific issues for consideration when designing buildings as suggested for Tokyo model.

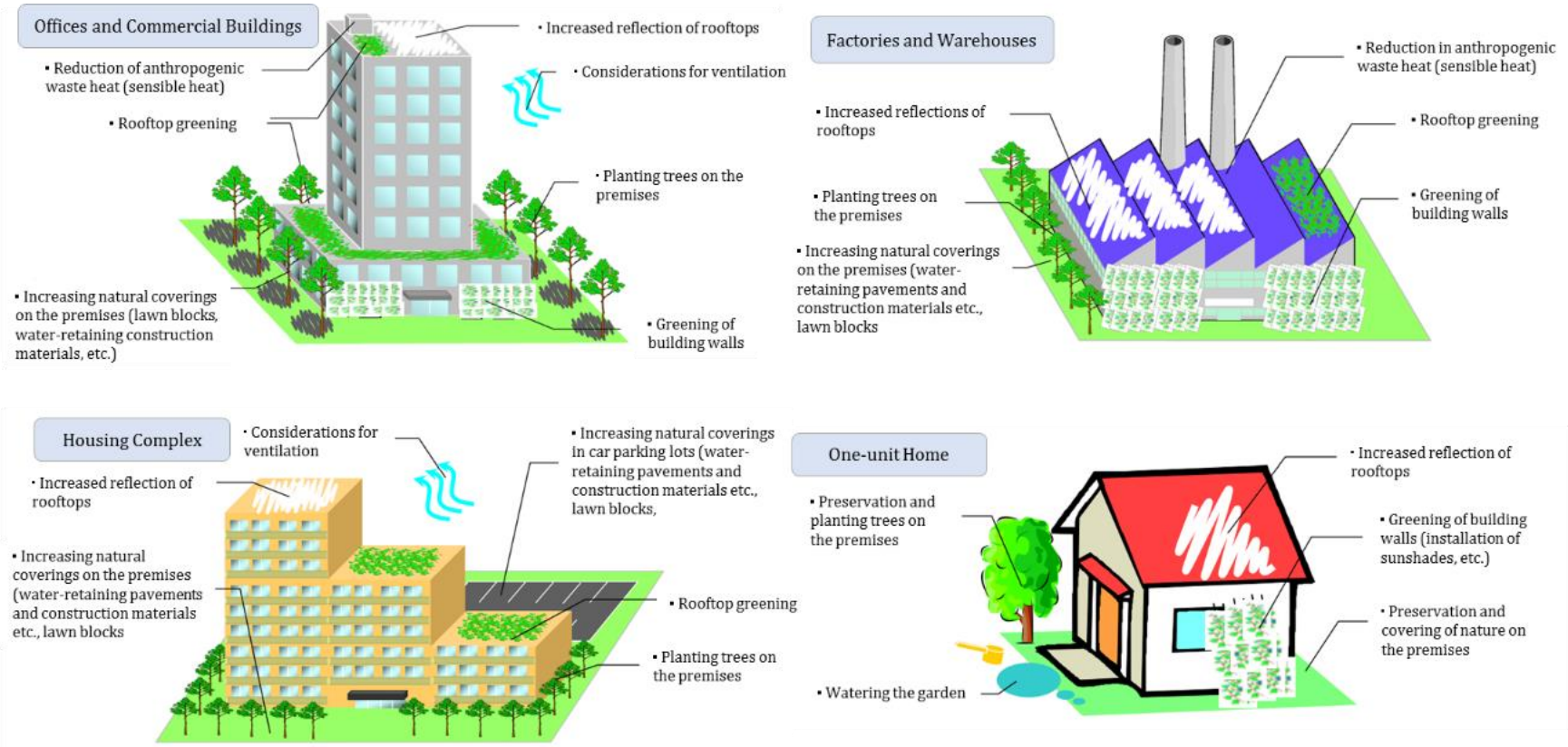


**Figure 4. Issues for consideration when designing buildings framed by the Bureau of the Environment, Tokyo Metropolitan Government (2005).**

### 1.3 Rationale and objectives

The study and understanding of UHI phenomenon is essential because it affects outdoor air quality, energy demand especially during summer, the distribution of pollutant concentration and local meteorology.

This study was conducted for two main purposes: (1) development of a CFD model for UHI simulation and (2) assessment of solar photovoltaic (PV) panels and water retentive pavement (WRP) as mitigation strategies for UHI. The CFD model was chosen over other types of simulation because of its ability to predict spatial distribution of air temperature and wind speed while taking into consideration key factors like solar radiation and sky view factor. By using CFD simulation, factors such as shadow effect, wind vortex formation and anthropogenic waste heat production in each building can be examined more closely. Moreover, our CFD model simulates urban environment in an unsteady state. Unsteady state analysis is more practical and realistic over steady state analysis because it considers changes in the rate of heat flow and temperature of a system with time. And this is one of the most important cases in an urban scenario.

Below are the specific objectives arranged in order as they appear in the paper:

1) Develop a building envelop model (hereafter referred to as BEM) to simulate heat transfer from building surface to the atmosphere
2) Develop a model for calculating anthropogenic waste heat
3) Predict diurnal variation in air temperature, wind speed and direction
4) Predict diurnal variation in building surface temperature
5) Predict diurnal variation in building surface energy fluxes
6) Develop a one-dimensional model for the heat and moisture pavement transport (hereafter referred to as PT model)
7) Couple the PT model with the CFD model
8) Predict diurnal variation in ground surface temperature and surface water content
9) Predict diurnal variation in ground surface energy fluxes

Due to limited calculation speed of the computers used, the simulations conducted in this study were only limited to a 24-hour (hr) unsteady state analysis. Furthermore, the calculation period chosen was characterized by a clear and calm weather. The seasonal variations, effect of rain and clouds were not accounted.

### 1.4 Conceptual framework and chapter organization

In the next chapter, the modelling parameterization and basic equations that comprise the CFD model are shown. It also discusses the BEM used to calculate for the surface energy budget of buildings and the weather research forecasting (WRF) model used to calculate the boundary conditions. Chapter 3 discussed the application of the developed CFD model by modelling a real city, in this case Osaka City. The mitigation strategy evaluated was solar PV panels. The effect of solar PV installation on anthropogenic heat and its energy output is also presented. Another mitigation strategy evaluated was the use of WRP as ground material for the main street. Before it can be assessed, a clear understanding on the heat and moisture transport in WRP must be determined and modeled. As a result, PT model was developed and discussed in Chapter 4. Finally, Chapter 5 discussed the coupled CFD-PT model where Suita City was used as real city model. The coupling of numerical models mentioned and concept of the study are presented in Fig. 5 and 6 respectively.

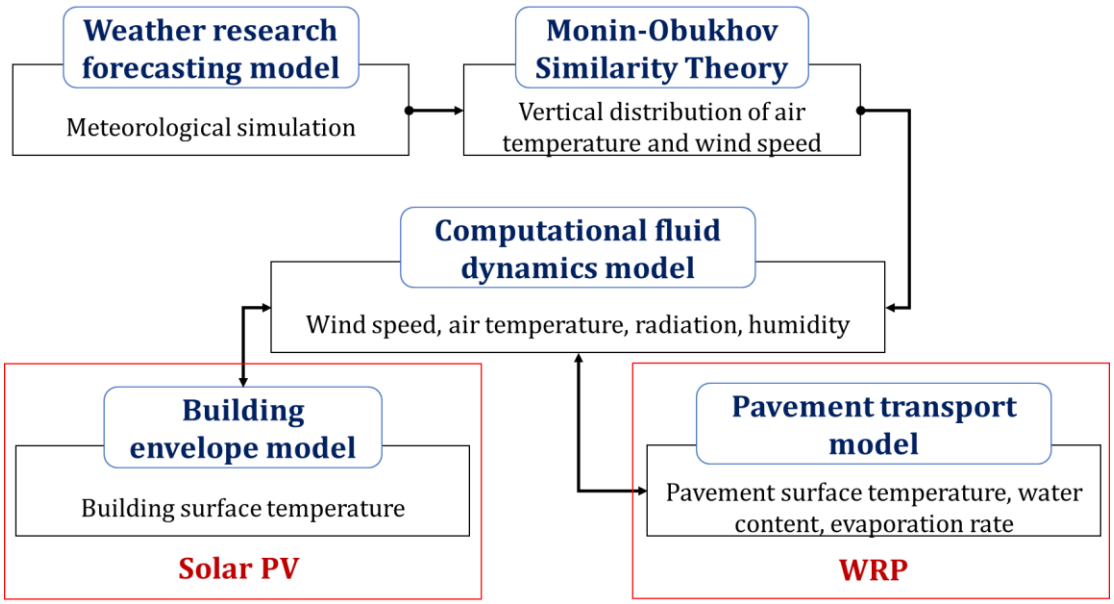


**Figure 5. Coupling of numerical models.**

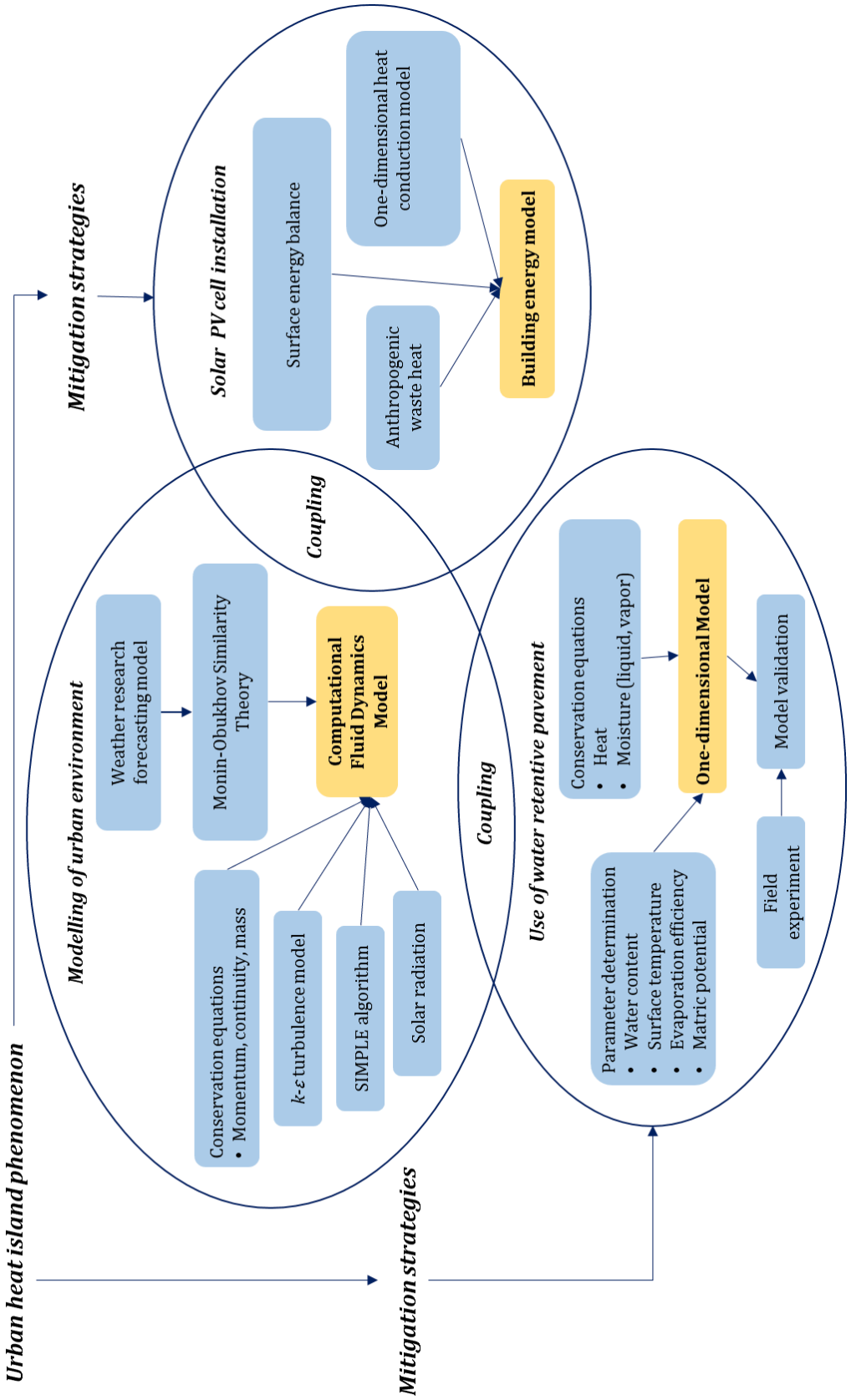


**Figure 6. Conceptual framework.**

# 2. MODELLING OF URBAN ENVIRONMENT USING CFD MODEL

## 2.1 Introduction

In Chapter 1, the numerous investigative approaches to understanding UHI and the limitations of each approach were presented. It was also stated that CFD model was used as the numerical simulation method. The CFD model is a significant tool for studying not only urban flow but also dispersion. Most studies dwell on understanding the fluid and dynamic process of urban flow and dispersion of pollutants (Baik, Kim & Fernando, 2013; Blocken, Stathopoulos & Carmeliet, 2007; Peng *et al.*, 2016; Tominaga & Stathopoulos, 2013). Baik, Kim & Fernando (2013) stressed that local meteorological conditions and roughness elements strongly influence urban flow. Likewise, roughness elements e.g. urban structures, vehicles, trees, etc. also affect urban roughness sublayer, its mechanical and thermal characteristics. Eventually this led to the commonality of CFD and building simulation (Bartak *et al*. 2002; Ramponi & Blocken, 2012; Zhai & Chen, 2004). In relation to UHI, CFD models are used predict UHI circulation (Wang & Li, 2016) and to assess mitigation strategies for improving thermal comfort. These mitigation strategies include: use of cool materials (Dimoudi *et al*., 2014; Fintikakis *et al.*, 2011; Georgakis, Zoras, & Santamouris, 2014; Maragkogiannis *et al.*, 2014; Zoras *et al*., 2014), evaporative cooling from water surfaces (Tominaga, Sato, & Sadohara 2015) and employment of bioclimatic design (He,

Yang, & Ye, 2014; Stavrakakis *et al*., 2012; Zoras *et al.*, 2014). With advances in technology, it is now possible to simulate building scale flow in real urban venue. This chapter presents the methods of developing the CFD model, the general equations used and setting boundary conditions. The main objectives are: (1) define methods of CFD model parametrization, (2) establish a calculation domain, (3) determine boundary conditions of the analytical area and (4) develop an energy budget model.

## 2.2 Basic equations

This section shows the parametrization of the CFD model. The governing equations were the Reynolds-averaged equations of momentum, mass continuity, heat and other scalar quantity expressed in Eq. (6)–(9) respectively. The eddy diffusivity approach (Eq. 10–12) was used to parameterize Reynolds stresses and turbulent fluxes in Eq. (6), (8) and (9). Equation 13 was used to relate eddy viscosity to $k$ and its dissipation rate $\varepsilon$. The effective Prandtl number and Schmidt number were defined using Eq. (14) and (15).

$$\frac{\partial U_i}{\partial t} + U_j \frac{\partial U_i}{\partial x_j} = -\frac{1}{\rho_0}\frac{\partial P^*}{\partial x_i} + \delta_{i3} g \frac{T^*}{T_0} + v\frac{\partial^2 U_i}{\partial x_j \partial x_j} - \frac{\partial}{\partial x_j}\left(\overline{u_i u_j}\right) \tag{6}$$

$$\frac{\partial U_j}{\partial x_j} = 0 \tag{7}$$

$$\frac{\partial T}{\partial t} + U_j \frac{\partial T}{\partial x_j} = K\frac{\partial^2 T}{\partial x_j \partial x_j} - \frac{\partial}{\partial x_j}\left(\overline{T' u_j}\right) + S_h \tag{8}$$

$$\frac{\partial C}{\partial t} + U_j \frac{\partial C}{\partial x_j} = D\frac{\partial^2 C}{\partial x_j \partial x_j} - \frac{\partial}{\partial x_j}\left(\overline{c u_j}\right) + S_c \tag{9}$$

$$-\overline{u_i u_j} = K_m\left(\frac{\partial U_i}{\partial x_j} + \frac{\partial U_i}{\partial x_j}\right) - \frac{2}{3}\delta_{ij}k \tag{10}$$

$$-\overline{T' u_j} = K_h \frac{\partial T}{\partial x_j} \tag{11}$$

$$-\overline{c u_j} = K_c \frac{\partial C}{\partial x_j} \tag{12}$$

$$K_m = C_\mu \frac{k^2}{\varepsilon} \tag{13}$$

$$Pr = \frac{v + K_m}{D + K_c} \tag{14}$$

$$Sc = \frac{v + K_m}{D + K_c} \tag{15}$$

The standard $k$-$\varepsilon$ model was used to simulate flow characteristics for incompressible viscous flow. The governing equations for turbulent energy and energy dissipation rate are shown below. In Eq. (16) the first and second terms on the right side of the equation represent shear and buoyancy production respectively. For simplicity, the definition of all variables in this section are arranged in Table 2.

$$\frac{\partial k}{\partial t} + U_j \frac{\partial k}{\partial x_j} = -\overline{u_i u_j} \frac{\partial U_i}{\partial x_j} + \frac{\delta_{3j} g}{T_0} \overline{T' u_j} + \frac{\partial}{\partial x_j}\left(\frac{K_m}{\sigma_k} \frac{\partial k}{\partial x_j}\right) - \varepsilon \tag{16}$$

$$\frac{\partial \varepsilon}{\partial t} + U_j \frac{\partial \varepsilon}{\partial x_j} = -C_{\varepsilon 1} \frac{\varepsilon}{k} \overline{u_i u_j} \frac{\partial U_i}{\partial x_j} + C_{\varepsilon 1} \frac{\varepsilon}{k} \frac{\delta_{3j} g}{T_0} \overline{T' u_j} + \frac{\partial}{\partial x_j}\left(\frac{K_m}{\sigma_\varepsilon} \frac{\partial \varepsilon}{\partial x_j}\right) - C_{\varepsilon 2} \frac{\varepsilon^2}{k} \tag{17}$$

The set of governing equations were solved numerically on a staggered grid system utilizing finite control volume with the semi-implicit method for pressure-linked equations (SIMPLE) method (Pantakar, 1980). The velocity components were extrapolated with an assumed pressure deviation field for every time step. The pressure deviation was then calculated using the Pressure-Poisson equation and the velocity components were adjusted with pressure corrections. Basing on Fig. 7, the velocity component ($U$, $V$, $W$) was defined at the center of each face of a control volume and scalar quantities ($P^*$, $T$, $C$, $k$, $e$ ) are defined at the center of the control volume.

**Table 2. A summary of variable definition used in Eq. (6) – (17).**

| Variable : definition |
|---|
| $t$ : time |
| $x_i$ : $i$th Cartesian coordinate |
| $U_i$ : $i$th mean velocity component |
| $P^*$ : pressure derivation from its reference value |
| $T$ : mean temperature |
| $C$ : mean concentration of species in air |
| $u_i$, $T'$, and $c$ : fluctuations from means $U_i$, $T$, and $C$ respectively |
| $\rho_0$ : air density |
| $T_0$ : reference temperature |
| $T^*$ : temperature derivation from its reference value $(= T - T_0)$ |
| $\delta_{ij}$ : Kronecker delta |
| $g$ : gravitational acceleration |
| $v$ : kinematic viscosity of air |
| $K$ : thermal diffusivity |
| $D$ : molecular diffusivity |
| $S_h$ : source heat |
| $S_c$ : source concentration |
| $K_m$ : eddy diffusivity of momentum |
| $K_h$ : eddy diffusivity of heat |
| $K_c$ : eddy diffusivity of mass concentration |
| $k$ : turbulent kinetic energy |
| $\varepsilon$ : dissipation rate |
| $\sigma_k$, $\sigma_\varepsilon$, $C_{\varepsilon 1}$, $C_{\varepsilon 2}$ : empirical constants |

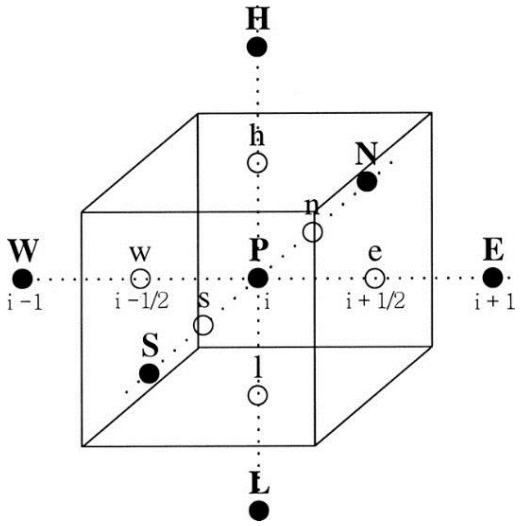


**Figure 7. A diagram of the staggered grid system and finite control volume (Baik, Kim & Fernando, 2003).**

The symbol $P$ denotes control volume center point; $W$, $w$, $e$ and $E$ are surrounding points in the $x$ direction; $S$, $s$, $n$ and $N$ are surrounding points in the $y$ direction; $L$, $l$, $h$ and $H$ are surrounding points in the $z$ direction.

## 2.3 Calculation domain

After the fundamental equations of the CFD model were established, a calculation domain was created. The calculation domain is the area of CFD analysis, here, real cities were chosen (discussed in Chapter 3 and 4). Parameters such as building height, coverage and energy consumption are necessary. Prior to simulation, a three dimensional or 3D model of the analysis area was created. The 3D model was then divided into meshes with a horizontal grid interval of 5 m. The size of the analysis area was set to 400 × 400 × 150 m and the buildings were within the smaller analytical area. Figure 8 shows a sample 3D model with one building and the analytical area in relation to the analytical range with meshes in $x$, $y$ and $z$ directions.

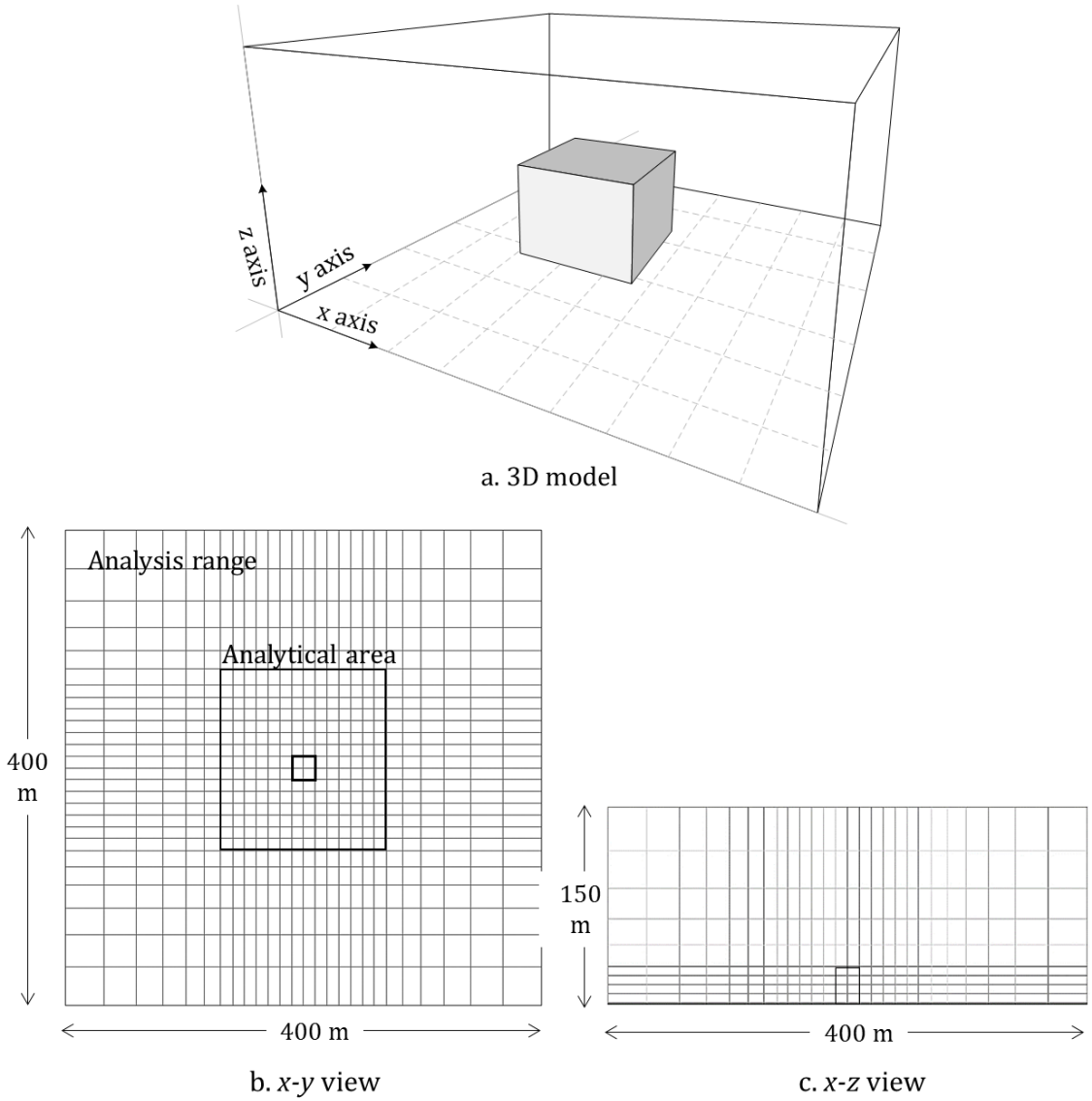


**Figure 8. A sample 3D model and mesh view of the calculation domain.**

## 2.4 Boundary conditions

The WRF model version 3.5.1 (Skamarock & Klemp, 2008) was used to determine the boundary conditions of the domain. For the application of the CFD model in both Chapter 3 and 5, the calculation period was August 8–9, 2011. This period was chosen because there was clear and calm weather brought by the high pressure system that formed above Japan (Fig. 8). Simulation of other weather scenarios such as overcast and winter conditions was not conducted.

The WRF configurations were similar to Shimadera *et al.* (2015) except the calculation period. Two WRF domains were established: Domain 1 (D1) for the larger Kinki Region and

Domain 2 (D2) for Osaka Prefecture. The maps of D1 and D2 with respect to Japan geography are presented separately in Chapters 3 and 5. The size of D1 was set to be 90 × 90 grid cells with 3 km horizontal grid resolution and D2 was 90 × 90 grid cells with 1 km horizontal grid resolution. Online one-way nesting in the two domains was used to consider the synoptic effect. The vertical resolution was 28 m, 92 m and 190 m. The meteorological fields in the Kinki region covering the analytical area was calculated for 24 h from 05:00 JST August 8, 2011 to 05:00 JST August 9, 2011. The spin-up period was August 1–7, 2011.

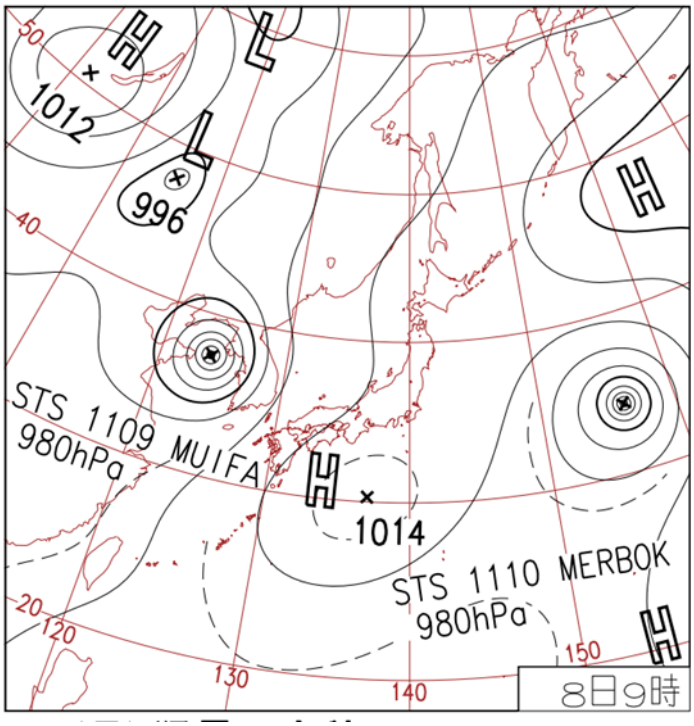


**Figure 9. Pressure system above Japan on August 8–9, 2011 (JMA, 2014).**

Due to coarser vertical resolution of WRF model compared with CFD, MOST was employed to determine the vertical distribution of air temperature and $u$, $v$ wind components. Under MOST, Eq. (18) to (20) were used to calculate friction velocity, temperature and Obukhov length respectively. The WRF data at heights 28 m and 92 m were used with a roughness length of 0.1 m. Then the vertical distribution obtained every hour were set in the unsteady boundary conditions for CFD analysis. Linear interpolation was used to calculate for the values in between each hour.

$$u_* \equiv (-\overline{u'}\overline{w'})^{\frac{1}{2}} \tag{18}$$

$$\theta_* \equiv \frac{(\overline{\theta'}\overline{w'})}{u_*} \tag{19}$$

$$L = -\frac{u_*^3 \bar{\theta}}{\mathcal{K} g \theta' w'} \tag{20}$$

Here, $\overline{u'}\overline{w'}$ are fluctuations from the mean velocity components, $\overline{\theta}$ is the mean temperature, $\overline{\theta'}$ is the fluctuation from the mean temperature and $\mathcal{K}$ is the van Karman constant (=0.40).

## 2.5 Energy budget model

### 2.5.1 Ground surface model

The ground surface model expressed in Eq. 21 was used to calculate the heat transfer from the ground of urban canyon to the atmosphere. Force restore method (Eq. 22) was used to simulate diurnal variations of ground temperature.

$$(1-\alpha_g)S\downarrow - \varepsilon'\sigma T_g^4 + f_{i,sky}R\downarrow + \sigma\sum f_{i,j}T_j^4 - Q_H = Q_G \tag{21}$$

$$\frac{\partial T_g}{\partial t} = 2\sqrt{\pi}\frac{Q_G}{\rho_{soil}c_{soil}d} - 2\pi\frac{T_g - T_s}{t_1} \tag{22}$$

where $\alpha_g$ is the ground albedo, $S\downarrow$ is the shortwave radiation, $\varepsilon'$ is the emissivity, $\sigma$ is Stefan-Boltzmann constant, $T_g$ is ground surface temperature, $f_{i,sky}$ is sky view factor from element $i$, $R\downarrow$ is downward longwave radiation, $f_{i,j}$ is view factor of each surface element *j* from element *i*, and $T_j$ is temperature of surface *j*, $Q_G$ is heat flux into the ground, $\rho_{soil}c_{soil}$ is heat capacity of the soil near ground surface, $d$ is soil depth, $T_s$ is soil temperature at $d$, $t_1$ is 86400 s.

The solar radiation and view factor were calculated following the method of Ikejima *et al.* (2011). The solar radiation was considered using parallel projection from the direction of sunlight. "A unique red-blue-green value was given to each mesh element on the surfaces of buildings and roads. Then parallel project from the direction of sunlight was drawn with computer graphics. The total number of pixels $n_i$ which has the same color ($i$ is the mesh element number) is counted for every mesh element. By comparing $n_i$ with $N_i$, which is the number of the pixels corresponding to a mesh element on the screen without any shield, a shielded mesh element can be distinguished. $N_i$ can be calculated also theoretically".

Direct and diffused solar radiation was calculated using Eq. (23) and (24).

$$S_{diff} = (0.66 - 0.32\,sin(h))E_{e0}sin(h)(1 - P^{cosech}) \times \left(0.5 + (0.4 - 0.3P)\,sin(h)\right) \quad (23)$$

$$S_{dir} = E_{e0}P^{cosech}l_i \quad (24)$$

where $S_{diff}$ means diffused solar radiation, $h$ is the solar zenith angle, $E_{e0}$ is the solar constant, $P$ is atmosphere transparency and $S_{dir}$ is direct solar radiation. Diffused solar radiation is divided into each surface by view factor from sky. "The view factor $dF$ between the unit area at the origin $O$ (view point) and an area $dS$ located in 3D space was calculated by the solid angle of $dS$". It is given by the equation below.

$$dF = \frac{dS'cos\theta}{\pi} \quad (25)$$

where $dF$ is view factor between the unit area at point $O$ and $dS$ (see Fig. 10), $dS'$ is projection of $dS$ on the surface of the hemisphere with unit radius and $\theta$ is the angle between the view line $OA$ and $z$-axis. For a detailed discussion of solar radiation and sky view factor, refer to Ikejima *et al.* (2011).

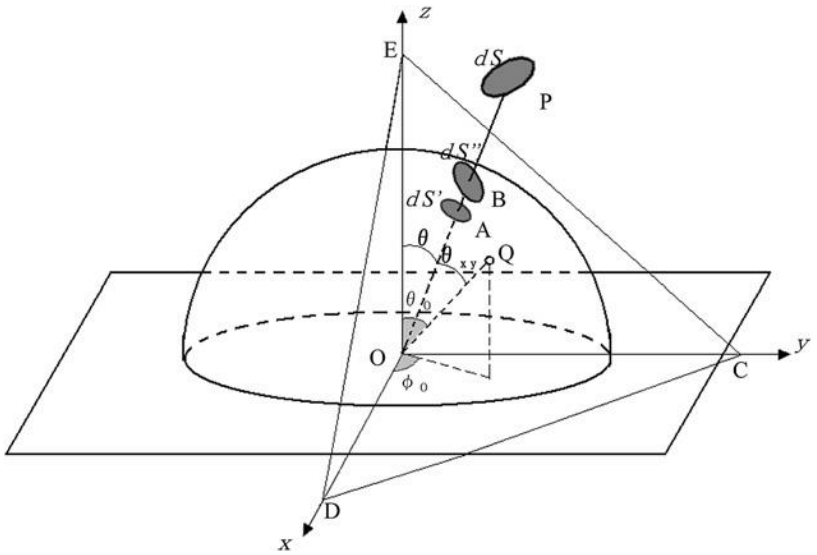


**Figure 10. The pyramid projection method.**

### 2.5.2 Building envelope model

The BEM illustrated in Fig. 11 was used to calculate the heat transfer from building surface to atmosphere. Unless otherwise specified, the term building surface could either mean roof or wall. For future reference, a general symbol *bs* was used in the succeeding sections to signify either roof or wall. Roof and wall were distinct from each other based on layer compositions (Table 3) and these were accounted into the CFD model. As shown in the BEM diagram, boundary condition *A* was established to calculate for the energy balance between outdoor air and building surface (Eq. 26).

$$-\varepsilon\sigma T_{bso}^4 + \sigma \sum f_{i,j} T_j^4 + (1-\alpha_{bs})\ S\downarrow\ +\ \rho_0 c_p C_H u(T_{bso}\ - T_{ao}) = Q \tag{26}$$

where $T_{bso}$ is the temperature of outer building wall, $\alpha_{bs}$ is building surface albedo, $c_p$ is specific heat at constant pressure, $c_H$ is bulk heat transfer coefficient, $T_{ao}$ is temperature of air above $T_{bso}$ and $Q$ is heat flux.

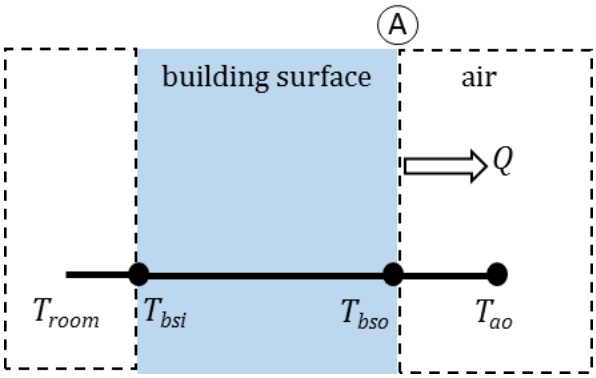


**Figure 11. The building envelope model showing mechanism of heat exchange.**

**Table 3. The layer composition of each surface and its corresponding characteristics.**

| | Material | Thickness (mm) | Conductivity (W/m·K) | Density (kg/m$^3$) | Specific Heat (J/kg·K) |
|---|---|---|---|---|---|
| Roof | Insulator [bsi] | 12 | 0.06 | 300 | 840 |
| | Gypsum board | 9 | 0.17 | 700 | 1471 |
| | Closed air | 10 | 0.03 | 1.16 | 1007 |
| | Concrete | 150 | 1.4 | 2300 | 839 |
| | Asphalt roofing | 10 | 0.11 | 1000 | 920 |
| | Polystyrene board | 25 | 0.04 | 50 | 1300 |
| | Mortar [bso] | 60 | 1.5 | 2100 | 757 |
| Wall | Gypsum board [bsi] | 12 | 0.17 | 700 | 1471 |
| | Closed air | 10 | 0.03 | 1.16 | 1007 |
| | Styrene foam | 25 | 0.04 | 25 | 1400 |
| | Concrete | 150 | 1.4 | 2300 | 839 |
| | Mortar | 20 | 1.5 | 2100 | 757 |
| | Tile [bso] | 8 | 1.3 | 2400 | 838 |

[bsi] means building surface innermost layer; [bso] means building surface outermost layer

## 2.6 Conclusions

This section presents a summary rather than a conclusion because this chapter was devoted in defining the methods of analysis. The CFD model was parametrized using the Reynolds-averaged equations of momentum, mass continuity and heat. These equations were solved numerically on a staggered grid system utilizing finite control volume with SIMPLE method. The CFD model has the ability to simulate real urban city which becomes the analysis range and the focus of calculation domain.

# 3. NUMERICAL ASSESSMENT OF SOLAR PV

## 3.1 Introduction

This chapter focuses on application of the developed CFD model into a real city scenario and the numerical evaluation on the effects of solar PV installation. For this mitigation strategy, Osaka City was chosen as model because it had the highest number of nights with temperature exceeding 30 °C from 1970 to 2000 (Ministry of Environment, 2014). Furthermore, Osaka City is one of the mega-cities in Japan in terms of population size. A study by Ono (2013) proved that it also has a high incidence of heat stroke, an illness which is strongly correlated to daily maximum temperature. These suggest that understanding Osaka City's UHI dynamics and assessing possible solutions are extremely essential.

Numerous studies examined the effect of solar PV installation on urban temperature. Mason *et al*. (2014) showed that solar panels reduce UHI up to 0.2 °C in daytime and 0.3 °C in nighttime but Taha (2013) pointed that PV conversion efficiency affects cooling. A study on the microclimate of Tianjin showed that integrated photovoltaics has a significant effect on building surface temperature but not on urban canyon air (Wang *et al*., 2006). Moreover, installation of PV panels also reduces energy consumption for air conditioning by about 10% (Genchi *et al*., 2013; Mason *et al*., 2014). In this chapter, the main interest is in determining the maximum impact of solar PV installation. Other scenarios such as installing solar PV to specific building surfaces was not determined. The objectives of this chapter are: (1) predict diurnal variation in urban canyon air temperature, wind speed and building

surface temperature (2) compare building surface energy fluxes and (3) predict power generation of solar PV.

## 3.2 Methods of analysis

### 3.2.1 WRF configuration and calculation domain

Figure 12 shows the results of WRF calculation for Osaka City on August 8–9, 2011 compared to the observed data from JMA Osaka meteorological observatory. In 2011, Osaka had an annual mean global solar radiation of 14.1 MJ/m$^2$ and mean cloud amount of 6.9. Figure 13 shows established D1 for the larger Kinki Region and D2 for Osaka Prefecture.

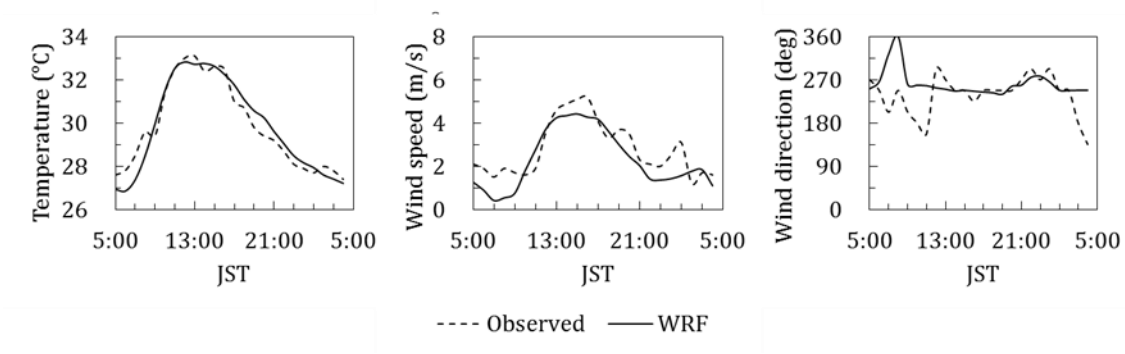


**Figure 12. Diurnal variations in air temperature, wind speed and wind direction on August 8–9, 2011.**

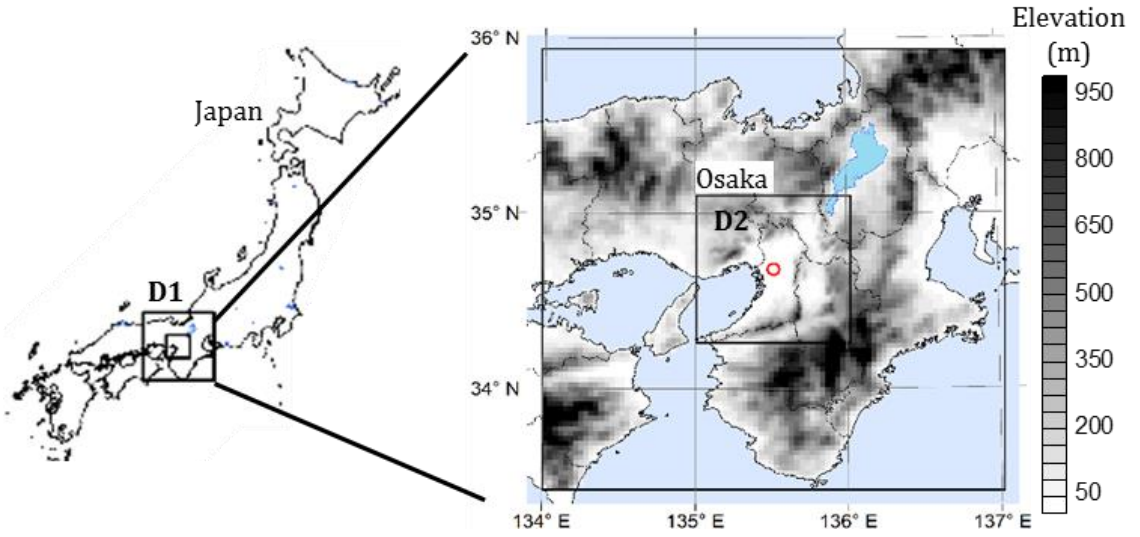


**Figure 13. Map of Kinki region showing D1 and D2 WRF domains.**

Figure 14 shows the vertical distribution of air temperature and *u*, *v* wind components obtained from MOST. Air temperature was warmer in the surface layer. The wind direction was north-east at 08:00 JST then shifted south-west from 12:00 to 20:00 JST. Wind speed was weakest in the morning but gradually increased during 12:00–16:00 JST. Average wind speed above the surface layer reached up to 3.3 m/s. The diurnal variation of wind speed and wind direction indicated that sea breeze developed well on August 8-9, 2011. These boundary conditions were applied to lateral boundaries of the CFD model, updated at every CFD time step.

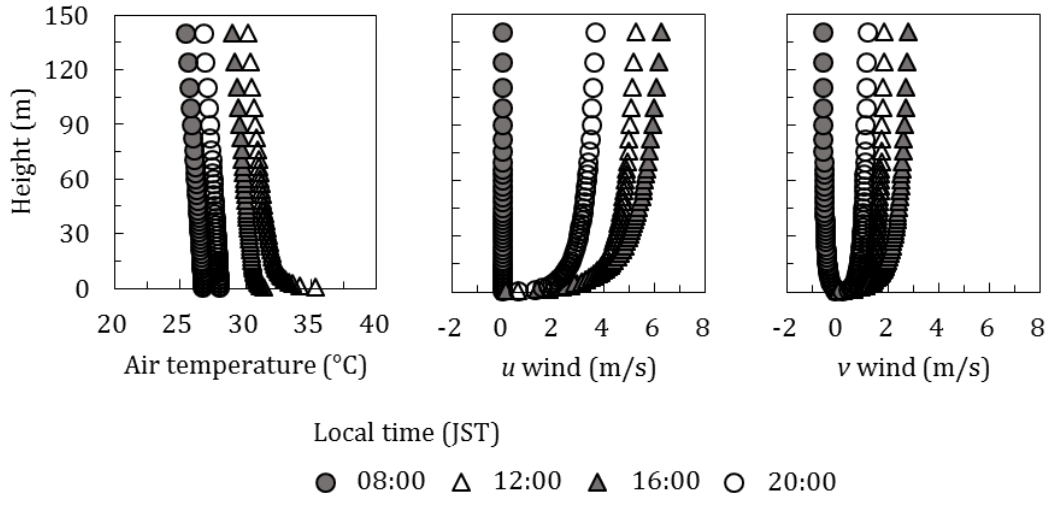


**Figure 14. The boundary conditions applied to lateral boundaries of the CFD model.**

The area of CFD analysis was 6-6 Fukushimaku, Osaka City, Japan (Fig 15). This area was chosen because it is in the center of Osaka City and exhibits a typical urban set up. The analysis range had mesh numbers 48 × 44 × 47 in the *x*, *y*, and *z* direction respectively (Fig. 16). The buildings were within the 200 × 200 × 69 m analytical area with a horizontal grid interval of 5 m.

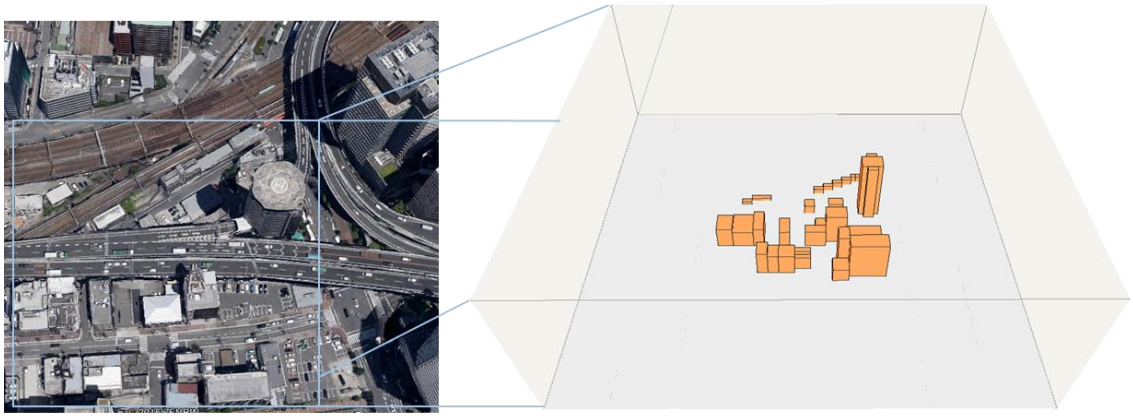

**Figure 15. The calculated domain of Fukushimaku district, Osaka City and its corresponding 3D model.**

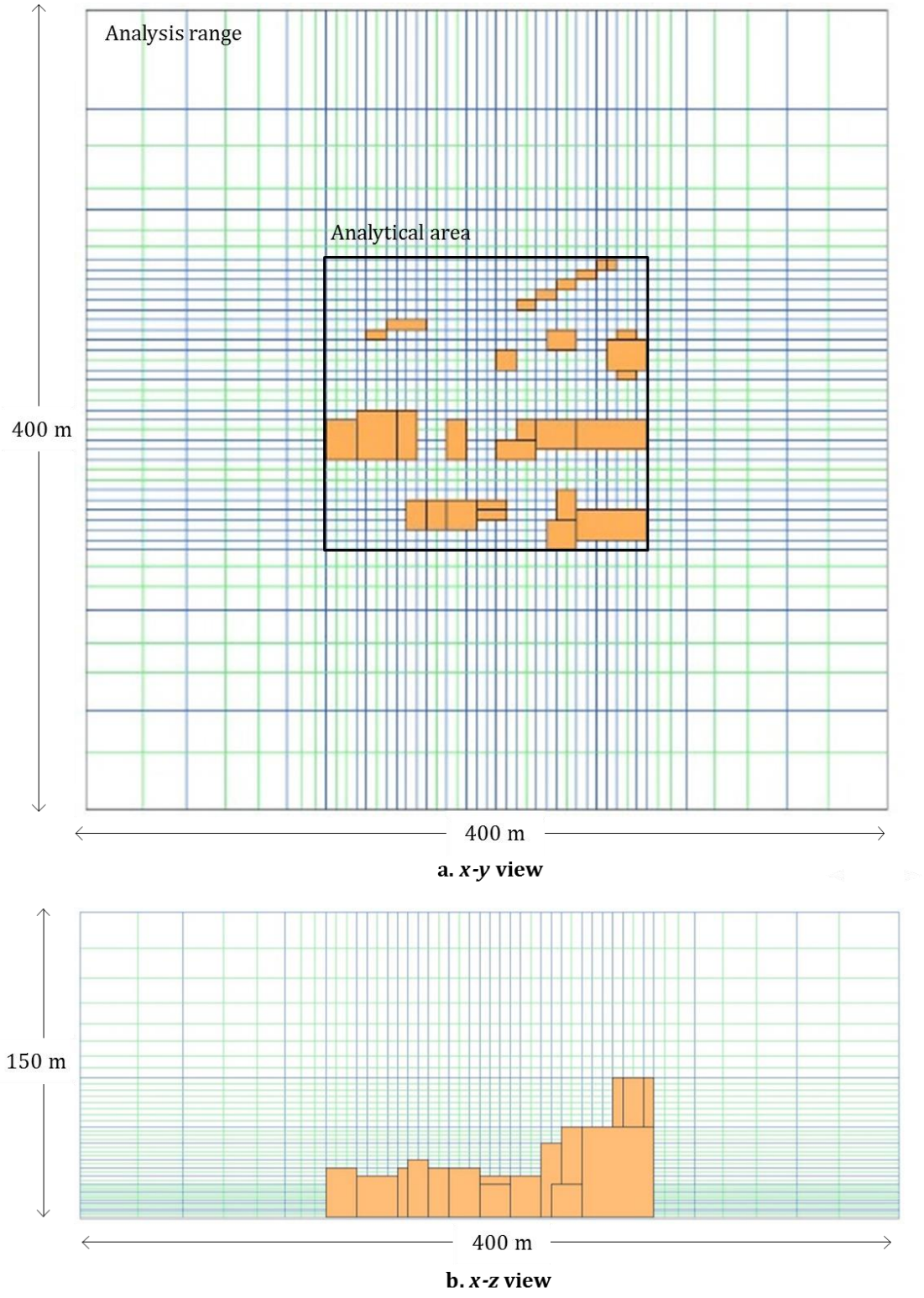


**Figure 16. Mesh view of the calculated domain.**

### 3.2.2 Modified BEM

Two cases of 24-h unsteady analysis were simulated: case 1 ($c_1$) for the current condition without solar PV (w/o PV) and case 2 ($c_2$) if solar PV were installed (w/ PV). In $c_2$, we assumed that the buildings were 100% covered with solar PV and the panels were installed 60 mm away from the surface. Similar to building walls and roof, solar PV layers were also distinguished (Table 4).

The boundary condition shown in Fig. 11 (Chapter 2) was used for $c_1$; for $c_2$ boundary conditions *A*, *B* and *C* were established (Fig. 17). Boundary condition *A* was used to calculate the energy balance between solar PV and the air above it (Eq. 27). Boundary condition *B* was used to calculate the energy balance between solar PV and the air beneath it (Eq. 28). Boundary condition *C* was used to calculate the energy balance between building surface and the air beneath the solar PV (Eq. 29).

$$-\varepsilon\sigma T_{pvo}^4 + \sigma \sum f_{i,j} T_j^4 + \ (1-\alpha_{pv})S\downarrow + \ \rho c_p c_H u(\ T_{pvo}\ - T_{aa}) = Q \tag{27}$$

$$-\varepsilon\sigma T_{pvi}^4 + \varepsilon\sigma T_{bso}^4 + h\ (T_{bso} - T_{ab}) = 0 \tag{28}$$

$$\varepsilon\sigma T_{pvi}^4 - \varepsilon\sigma T_{bso}^4 - h(T_{bso} - T_{ab}) = 0 \tag{29}$$

Here, $T_{pvo}$ is the outer surface temperature of solar PV, $\alpha_{pv}$ is albedo of PV cell, $T_{aa}$ is temperature of air above the solar PV, $T_{pvi}$ is inner surface temperature of solar PV, $T_{ab}$ is temperature of air beneath the solar PV and $h$ is convective heat transfer coefficient.

**Table 4. The layer composition of solar PV and its corresponding characteristics.**

| | Material | Thickness (mm) | Conductivity (W/m·K) | Density (kg/m$^3$) | Specific Heat (J/kg·K) |
|---|---|---|---|---|---|
| Solar PV | Glass [pvi] | 0.1 | 0.78 | 3000 | 500 |
| | EVA | 0.5 | 0.12 | 1200 | 1250 |
| | Silicon | 0.35 | 168 | 2330 | 677 |
| | EVA | 0.5 | 0.12 | 1200 | 1250 |
| | Glass [pvo] | 3.2 | 0.78 | 3000 | 500 |

[pvi] means PV innermost layer; [pvo] means PV outermost layer

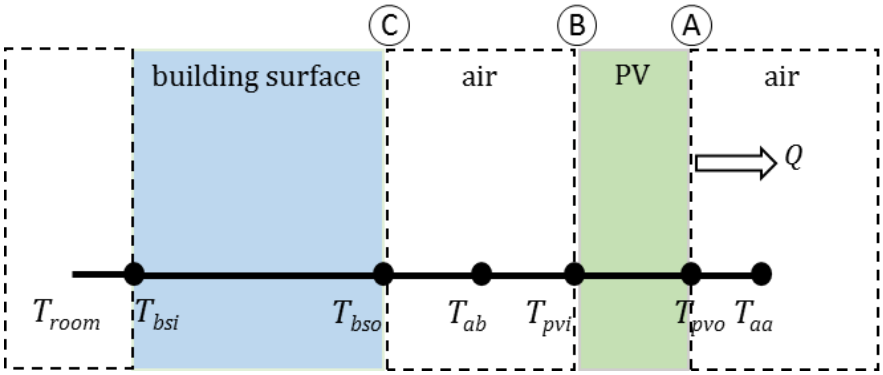


**Figure 17. The layer composition of solar PV and its corresponding characteristics.**

The one-dimensional heat conduction model (Eq. 30) was coupled with CFD to calculate for the surface temperature of roof, walls and solar PV. The power generated by PV panels (Eq. 31) and the anthropogenic waste heat (Eq. 32) due to cooling of buildings were also determined and incorporated into the model.

$$c_v \frac{\partial T_i}{\partial t} = K\left(\frac{\partial T_i^2}{\partial^2 x}\right) - PV_{output} \tag{30}$$

$$PV_{output} = \eta \ \left(-\varepsilon\sigma T_{pvo}^4 + \sigma \sum f_{i,j} T_j^4 + \ (1-\alpha_{pv})S\downarrow\right) \tag{31}$$

$$Q_{ant} = \left(1 + \frac{1}{COP}\right)(H_{out}) \tag{32}$$

where $c_v$ is the PV heat capacity, $PV_{output}$ is power generated by solar PV, $\eta = 0.18$ which is the PV power generation efficiency, $COP$ is air conditioner coefficient of performance and $H_{out}$ is sensible heat pumped out of the building for cooling. The method for estimating $H_{out}$ can obtained be from Ohashi *et al*. (2007). In this study latent heat was assumed be zero. The values of the parameters mentioned from Eq. (27) to (32) are listed in Table 5.

**Table 5. Value of the parameters used for solar PV assessment.**

| Parameter | Value |
|---|---|
| Ground albedo | 0.1 |
| Roof albedo | 0.1 |
| Wall albedo | 0.1 |
| Albedo of PV glass layer | 0.073 |
| Albedo of PV silicon layer | 0.03 |
| Room temperature inside the building | 28 °C |
| Bulk transfer coefficient | 0.0075 |
| Convective heat transfer coefficient | 8.3 W/m²·K |
| Emissivity | 0.9 |

## 3.3 Results and discussion

### 3.3.1 Effect on urban surface temperature

The surface temperature was distinguished into four types: $T_w(w/o\ PV)$ for the walls in $c_1$, $T_w(w/\ PV)$ for the walls in $c_2$, $T_r(w/o\ PV)$ for the roofs in $c_1$ and $T_r(w/\ PV)$ for roofs in $c_2$. Figure 18 shows the temperature difference on each building surface computed as: $\Delta T_w = T_w(w/o\ PV) - T_w(w/\ PV)$ for wall and $\Delta T_r = T_r\ (w/o\ PV) - T_r\ (w/\ PV)$ for roof. In calculating for the mean surface temperature, building walls were further differentiated into east, west, north and south walls respectively. Figure 19 shows the diurnal variation in mean surface temperature for two cases and their difference. Results showed similarity in both cases. From 06:00 to 08:00 JST, the east surface had the maximum average surface temperature: $T_w(w/o\ PV)$ = 36.3 °C and $T_w(w/\ PV)$ = 38.0 °C. At noon, roof surface had the maximum average surface temperature: $T_r(w/o\ PV)$ = 52.4 °C and $T_r(w/\ PV)$ = 49.1 °C. At 18:00 JST, west surfaces were warmest: $T_w(w/o\ PV)$ = 40.9 °C and $T_w(w/\ PV)$ = 37.7 °C. It can be seen from the mean surface temperature difference (Fig. 19c) that installation of solar PV caused specific warming of walls and roof, however it occurred at different times of the day. The average warming were the following: 0.4 °C for the roof from 08:00 to 10:00 JST, 2.6 °C for east walls from 08:00 to 11:00 JST, 0.9 °C for south walls from 10:00 to 12:00 JST, 0.1 °C for north walls from 11:00 to 12:00 JST and 0.8 °C for west walls from 13:00 to 16:00 JST. These results imply that while one side of the building had warmer surfaces, other sides had cooler surfaces. In fact, if average surface temperature difference into daytime (06:00-17:00 JST) and nighttime (18:00-05:00 JST) are distinguished, calculated values indicated that installation of solar PV caused an overall cooling. The average daytime cooling was up to

0.8 °C for walls and 2.1 °C for roof while average nighttime cooling was up to 4.3 °C for walls and 1.4 °C for roof.

The ability of an urban structure to absorb or reflect solar radiation depends highly on its heat capacity, heat conductivity and albedo. The albedo effect cannot be established; even if the different albedo of solar PV glass layer and silicon layer (Table 5) was accounted, the total albedo of solar PV was equivalent to roof and wall albedo respectively. On the other hand, solar PV have a lower thermal capacity and higher thermal conductivity compared with building roof and wall. This means that in building surfaces w/ PV, surface temperature is easily raised by solar radiation and stored heat is released faster compared with building surfaces w/o PV. But presence or absence of solar radiation is not the only driving force of temperature changes in surfaces w/ PV, the position of the sun also plays a great role. As the sun rises in the east, east walls receive solar radiation which cause warming on that side of the building. As the sun sets in the west, west walls receive solar radiation which cause warming on that side of the building. Under partial or full overcast weather conditions, it can be predicted that specific warming during daytime will be minimized and average cooling will be increased because solar radiation is prevented from hitting the solar PV directly.

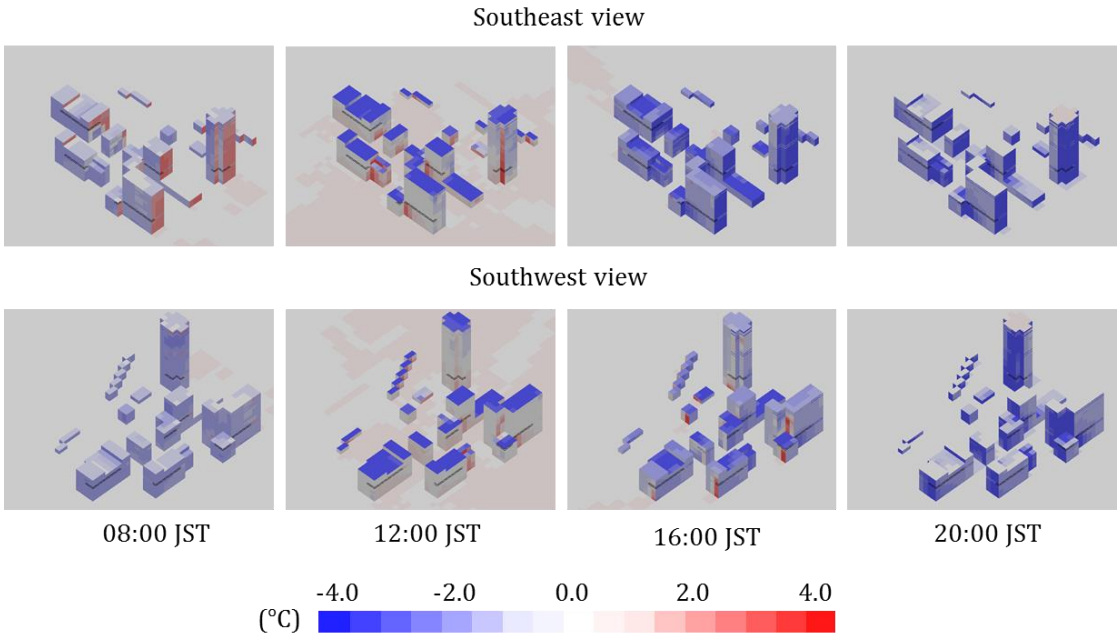


**Figure 18. The effect of solar PV installation on building surface temperature.**

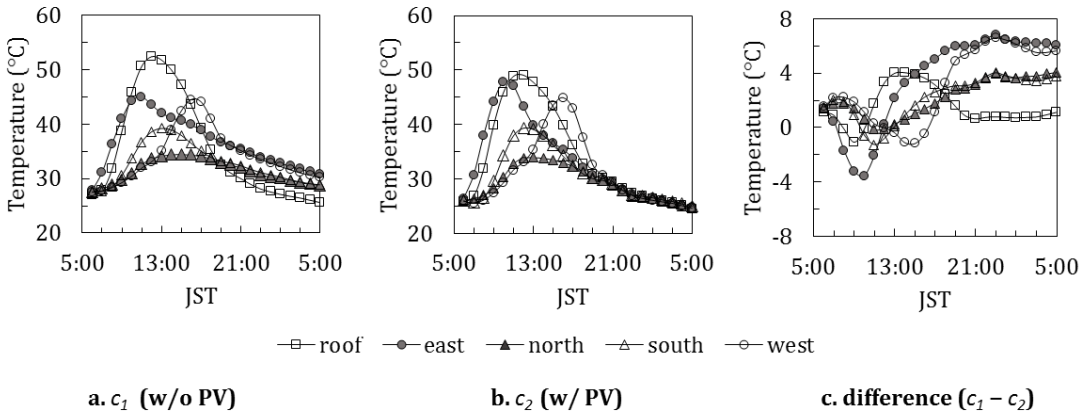


**a. $c_1$ (w/o PV)** **b. $c_2$ (w/ PV)** **c. difference ($c_1 - c_2$)**

**Figure 19. The effect of solar PV installation on building surface temperature.**

Comparing building surfaces, cooling effect of solar PV was greater on roof during daytime but greater on walls during nighttime. The greater cooling on roof during daytime was attributed to the more efficient thermal convection and greater sky view factor which led to air circulation. The greater cooling effect of solar PV on wall during nighttime can explained by examining the temperature profile of each surface layer (Fig. 20). Profiling was from inner room air at 0.0 mm thickness until the outermost air. For walls w/o PV, temperature increased gradually from the gypsum board and reached a plateau in the concrete layer. On the other hand, for walls w/ PV, the temperature of layers did not increase. For roof, temperature increase occurred in the mortar layer regardless of the presence or absence of solar PV. These results imply that presence of solar PV shaded the wall surface but not the roof. This shading effect on wall decreased the amount of heat absorbed during the day and hence decreased the amount of heat released at night. Masson *et al.* (2014) and Genchi *et al*. (2003) had already proved the shading effect and emphasized that it could also lead to a reduction in energy consumption.

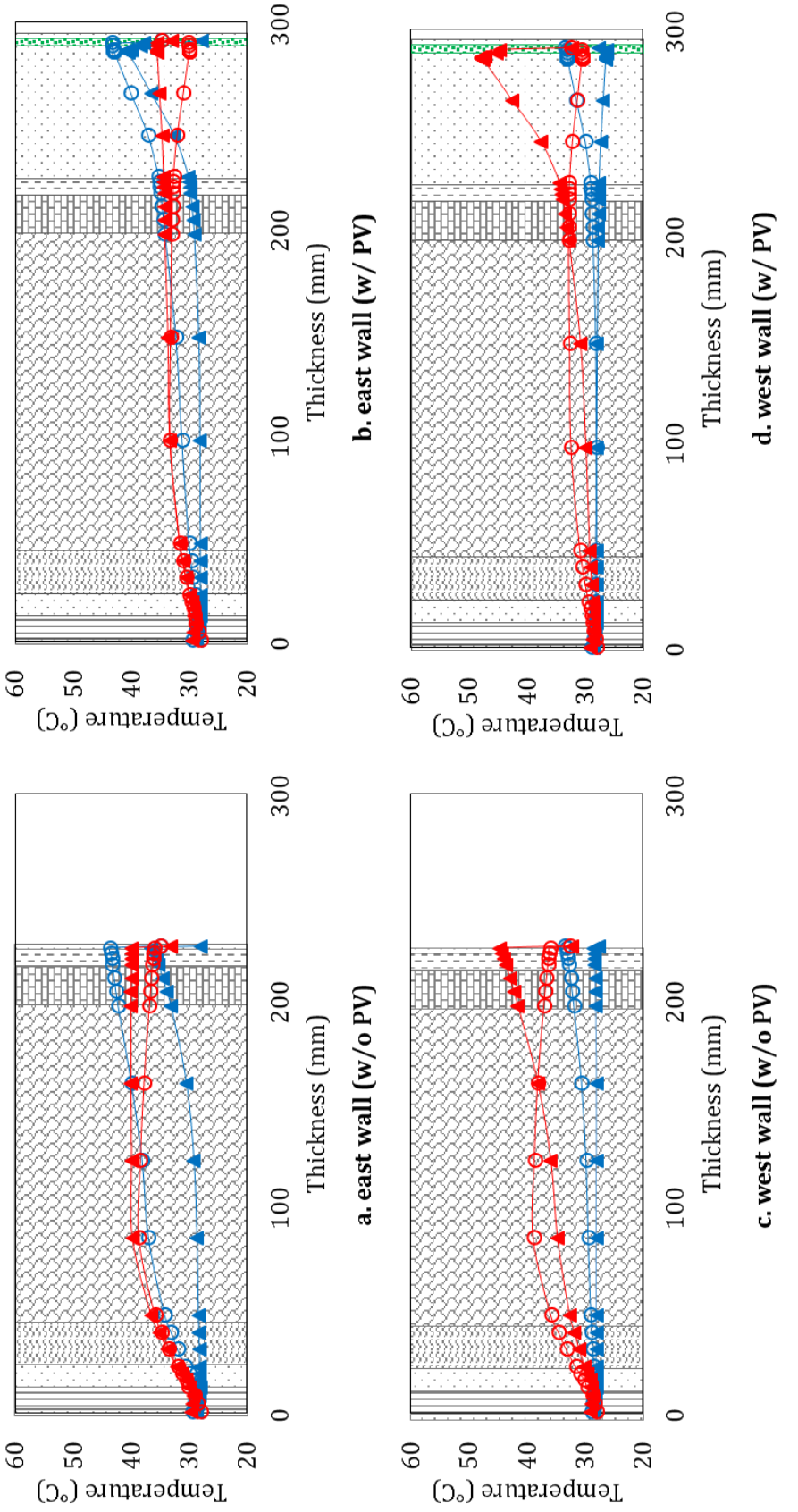


**Figure 20. The temperature profile of building surfaces in $c_1$ and $c_2$ (*continued*).**

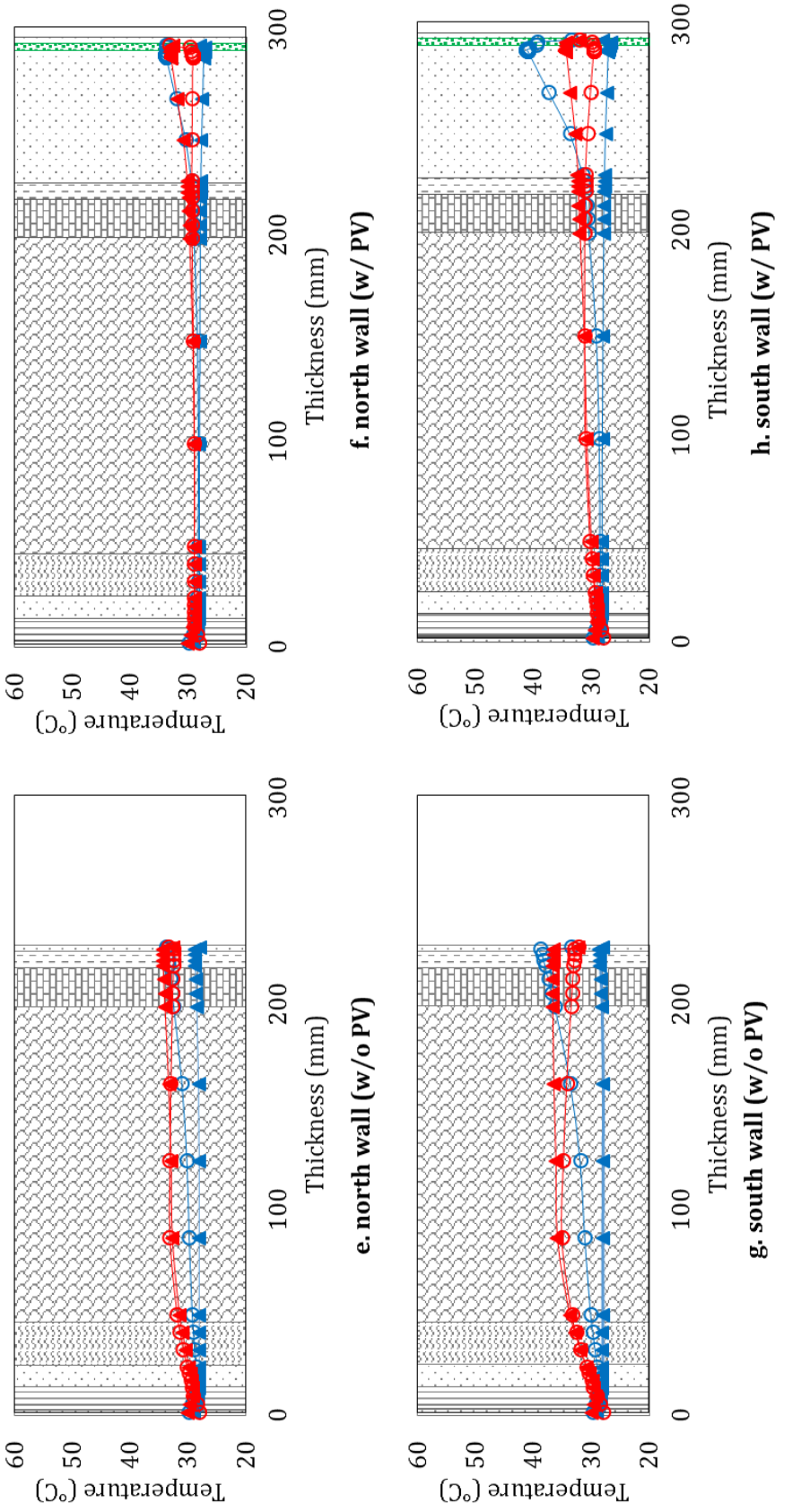


**Figure 20. The temperature profile of building surfaces in $c_1$ and $c_2$ (*continued*).**

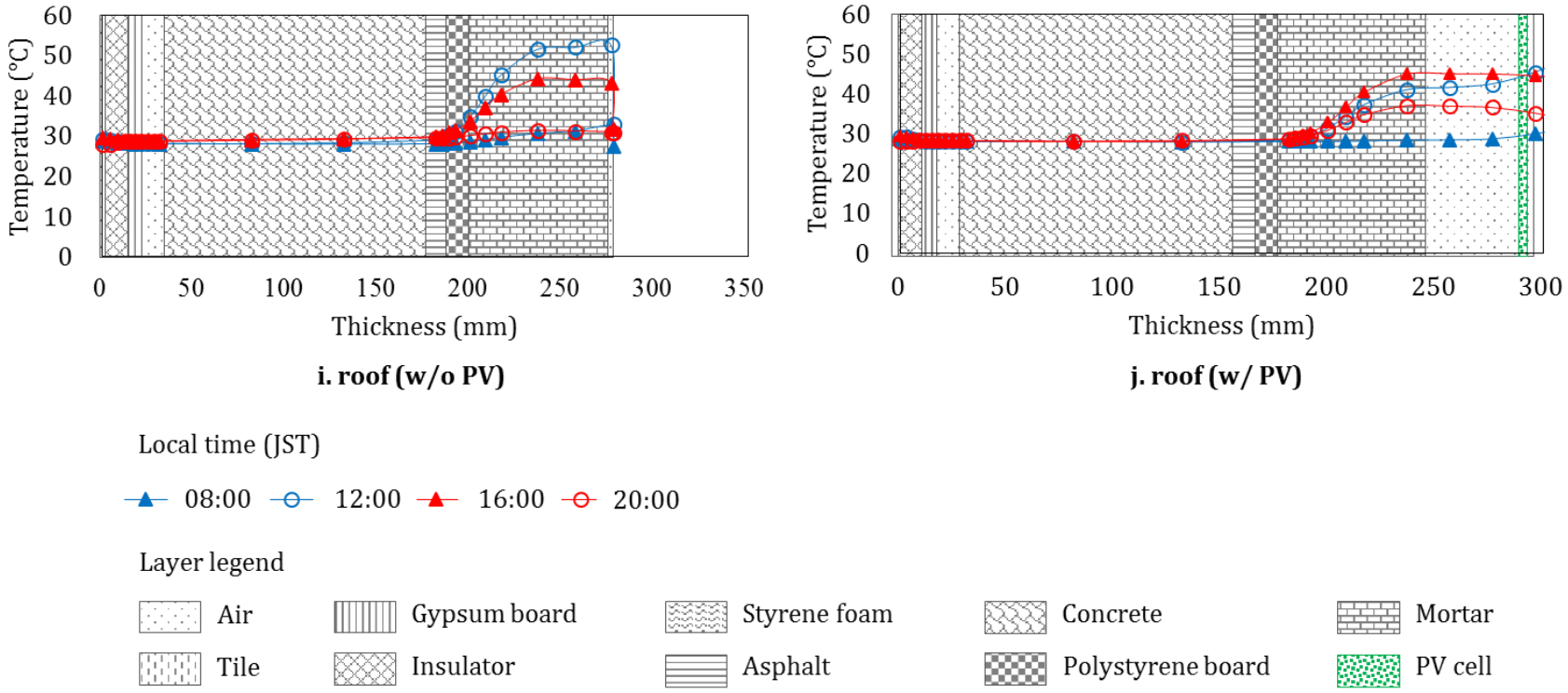


**Figure 20. The temperature profile of building surfaces in $c_1$ and $c_2$.**

### 3.3.2 Effect on air temperature and flow field

Figure 21 shows the flow field and air temperature difference computed as: $\Delta T_a = T_a(w/o\ PV) - T_a(w/\ PV)$. Wind pattern was south-west and maximum wind velocity occurred from 12:00 to 16:00 JST. Results of air temperature difference at 1.5 m above actual street level and above the roof showed equal average cooling of 0.1 °C from 08:00 to 20:00 JST. The *x-y* section shows that maximum cooling of about 0.4 °C was observed in the southeast area at 20:00 JST.

Taha (2013) proved that PV power generation efficiency ($\eta$) and effective albedo can affect air temperature. But in this study, the direct effect of these factors cannot be established. The simulation was at $\eta = 0.18$ only and as mentioned in the previous section, PV albedo did not affect overall albedo of the area. Instead, Eq. (30) and (31) express that generation efficiency and albedo affects surface temperature and this indirectly affects air temperature. The presence of solar PV led to the decrease in surface temperature that eventually affected urban air temperature. And this was intensified by the lee wind which brought cool air further into the urban canopy.

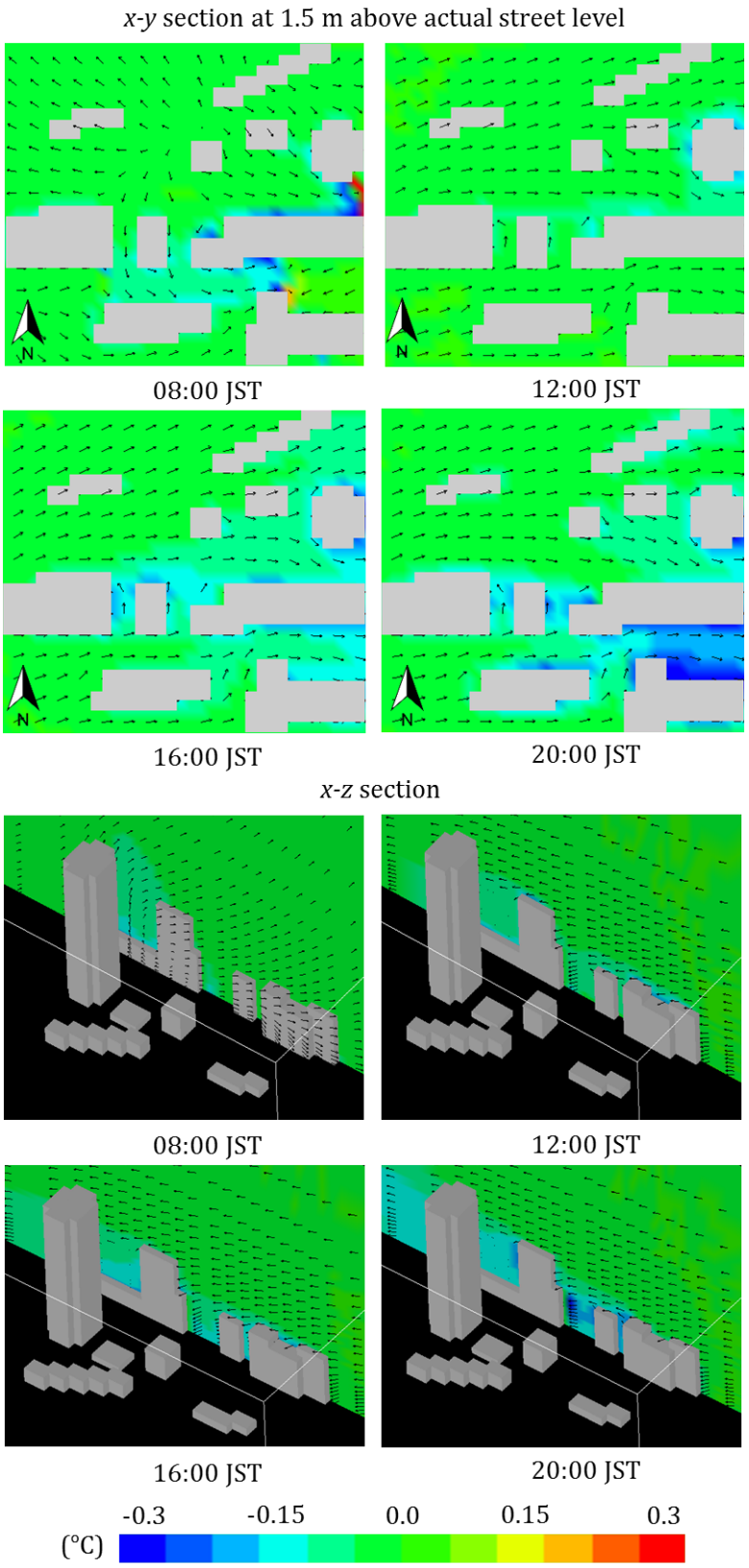


**Figure 21. The wind field and air temperature difference.**

### 3.3.3 Comparison on surface energy flux and power generation

The anthropogenic heat waste was assumed to be released from rooftop only. The decrease in surface temperature as a result of PV installation is expected to decrease the need for room cooling and eventually the waste heat. But results in Fig. 22 show no significant difference between waste heat in $c_1$ and $c_2$. Masson *et al*. (2014) had similar findings and noted that thermal type of solar cells has the greater ability to decrease waste heat compared with solar PV. In the same figure, it can be seen that $c_2$ had higher net radiation due to decreased upward longwave radiation (which is also an effect of surface cooling). There was also lower sensible heat flux and ultimately an increase in net heat flux. Tien *et al.* (2007a) noted that deployment of solar PV reduced sensible heat flux as a consequence of different roof albedo and wind speed.

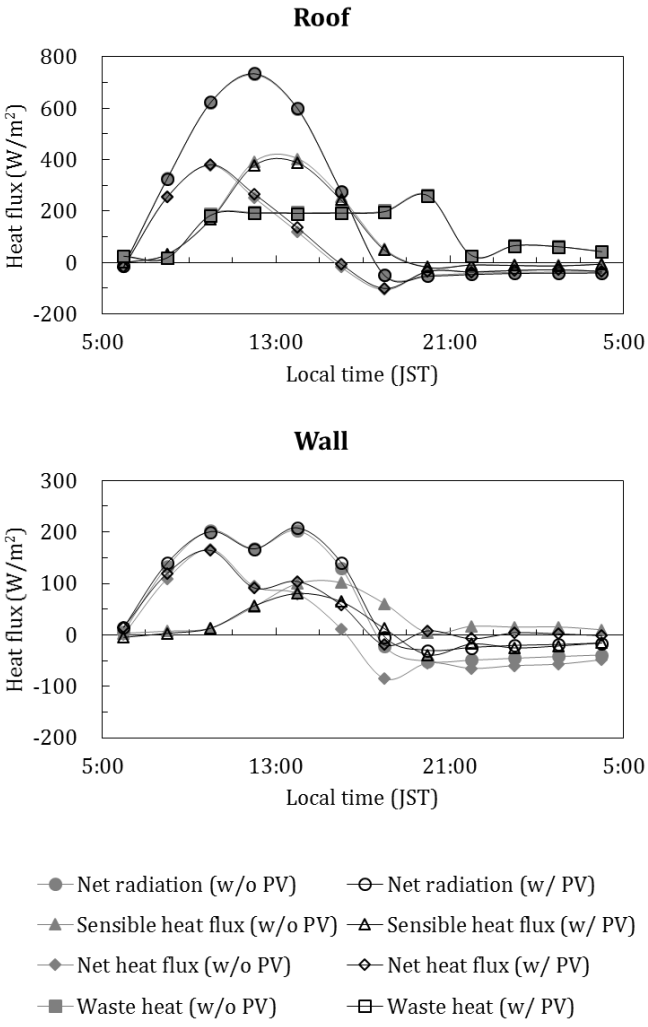


**Figure 22. A comparison of energy fluxes between $c_1$ and $c_2$.**

Results of hourly PV output showed that roof PV produced 63.5% more power compared with wall solar PV (Fig. 23). At 06:00 JST, roof PV were not able to generate power while wall PV generated 3 W/m$^2$. This minimal generation of electricity from PV walls was due to the sun's radiation hitting the east walls. At 12:00 JST, roof PV produced 132 W/m$^2$ of power, which was 77% more efficient compared with the output of wall PV.

Tian *et al*. (2007b) stressed that power output of PV is indirectly proportional to module temperature and that high module temperature is a result of high ambient temperature and low wind speed. The high ambient temperature of walls and low wind speed within the urban canopy (Fig. 21), resulted to decreased power output. It was assumed that PV output will be used for room cooling purposes only so that greater PV output is projected to decrease building energy consumption. It must be noted that PV output presented in this section is generally true for the summer season of Osaka. The trend in power output may change due to factors like ambient temperature which is lower in winter, angle of the sun and length of sunshine hours. Although heat loss due to power generation was not considered, findings of Boer (2001) claimed that extraction of electric power in PV cells will result to a decrease in temperature. He estimated a 10 °C decrease in temperature for PV cells with 20% efficiency. Based on the findings of this study, greater heat loss would potentially occur in roof PV.

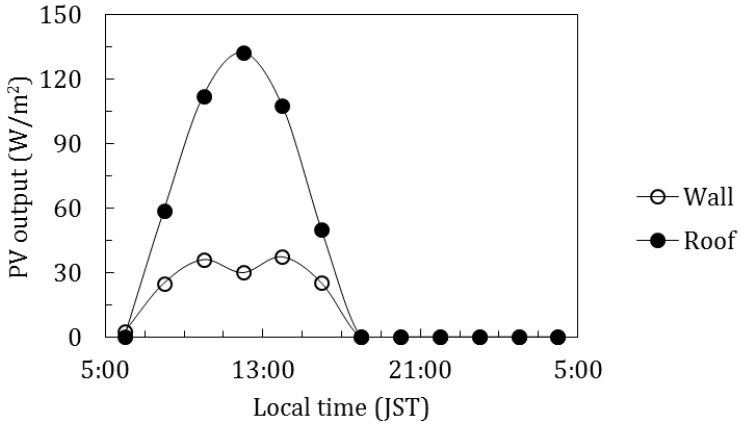


**Figure 23. The hourly power output of solar PV installed on walls and roofs.**

## 3.4 Conclusions

Under clear weather conditions, installation of solar PV cause an overall cooling of building surface during daytime and nighttime but specific warming may occur depending on the position of the sun. During daytime, cooling effect is greater on roof surface because of efficient thermal convection and greater sky view factor which led to air circulation. During nighttime, cooling effect is greater on wall surface because of the shading effect. The shading effect minimizes the heat absorption during daytime and hence minimizes heat release during nighttime. The cooling of surface temperature eventually leads to cooling of urban air. Presence of solar PV has no effect on waste heat but can reduce sensible heat flux. Roof PV produce greater PV output than wall PV and under the assumption that the power generated will be used for cooling, a decrease in energy consumption can be expected.

# 4. HEAT AND MOISTURE TRANSPORT IN PAVEMENT SURFACE

## 4.1. Introduction

According to Yamamoto *et al*. (2006) up to 20% of the total surface area in Japan have asphalt pavements. A review by Santamouris (2013) confirms that the reduction in surface temperature and sensible heat flux through use of cool pavements is one of the most important mitigation strategies against UHI. Cool pavements are of several kinds, however this study focused on water retentive pavements (WRP). Retention pavements are made from several materials; Takahashi and Yabuta (2009) assessed blast furnace slag as water retaining material and it led to a 10 °C decrease in surface temperature compared with asphalt. On a similar study, Takebayashi and Moriyama (2012) showed that asphalt with water-retaining materials could reduce sensible heat flux up to 150 $W/m^2$. Cement concrete with water-retaining material can reduce sensible heat flux up to 100 $W/m^2$ during daytime and 20 $W/m^2$ during nighttime. They account these to the differences in albedo, evaporation rate and thermal mass. On the other hand, Nakayama and Hashimoto (2011) studied WRP made from steel by-products and owed the cooling capacity to evaporation, reflectance and water volume. Nakayama and Fujita (2010) proved that air temperature above the pavement is 1-2 °C lower compared with lawn. They also found out that cooling effect decreased with evaporation. Outdoor experiments of Kubo *et al*. (2006) showed that after

rain, WRP has the ability to reduce air temperature at 1.5 m up to 1 °C. The evaporation rate is proportional to the evaporation efficiency of water retentive material (Kinoshita et al., 2012). However, Misaka *et al*. (2009) pointed out that the evaporation efficiency increases when surface temperature is greater than 25 °C. A secondary effect of using WRP would be addressing the storm water management issues (Li *et al.*, 2013) because it can hold runoff volume due to its permeability.

This chapter evaluates the use of WRP made from fly ash, a residue from coal combustion and mainly used as concrete additive. The addition of fly ash into the pavement contributes to material porosity and thus its ability to hold water (Fig. 24). Due to the nature of fly ash as an industrial product, the WRP used in this research could also contribute to material recycling. The main objective is to develop a PT model examining the heat and moisture characteristics of WRP. The development of a PT model is important in order to assess the performance of a material before it can be fully employed in an urban set up. Furthermore, the developed model could also be applied to the assessment of new pavement materials. The specific objectives are: (1) determine the evaporation efficiency, volumetric water content, and matric potential of WRP, (2) create a temperature and moisture content profile from surface to bottom layer (3) calculate heat fluxes, (4) validate the accuracy of the PT model by comparing it with field experiment and (5) compare the performance of WRP with asphalt.

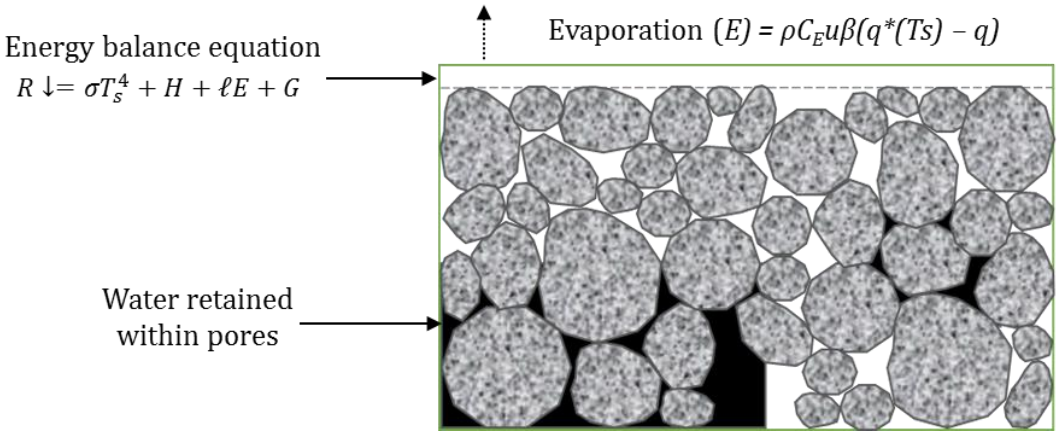


**Figure 24. A schematic diagram on the porous nature of WRP.**

## 4.2 Methods of analysis

### 4.2.1 Parameters

The parameters used for simulation were volumetric water content ($\theta$), evaporation efficiency ($\beta$) and matric potential ($\psi$). In this study, the pavement materials in focus are WRP and asphalt but for comparison purposes the thermal and water performance of two brick types (Brick A and Brick B) were also determined. The pavement materials tested had a volume of 0.15 × 0.15 × 0.05 m each. In order to determine $\theta$, the pavement was first soaked in water for 24 hr, then wrapped with a wet towel and transferred into a sealed plastic container to ensure a fully wet condition (Fig. 25). The $\theta$ was computed using Eq. (33). The detailed procedure can be obtained from Karasawa *et al.* (2006), Ueno and Tamaoki (2009) and Yamamoto *et al*. (2006).

$$\theta = \frac{volume\ \ of\ \ water\ \ absorbed\ \ (ml)}{volume\ \ of\ \ pavement\ \ (ml)} \tag{33}$$

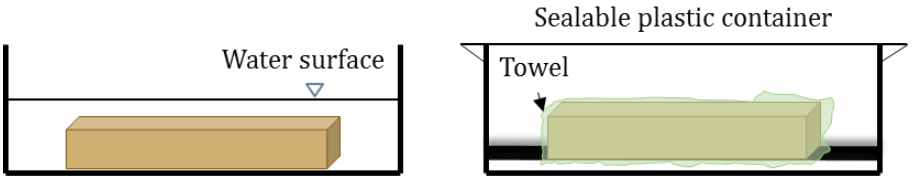


**Figure 25. A diagram of the volumetric water content measurement.**

The $\beta$ was calculated using the evaporation equation for bare soil developed by Kondo *et al.* (1990) and expressed as:

$$E = \rho_0 C_E u \beta [q_s(T_s) - q_a] \tag{34}$$

Here, $E$ is evaporation rate, $C_E$ is bulk coefficient of evaporation and $q_s$ is specific humidity at surface temperature $T_s$. Values of $\beta$ indicate that if $\beta < 0$ condensation occurs, $\beta = 1$ means maximum evaporation and $\beta = 0$ means no evaporation.

In order to measure the evaporation rate, the saturated pavement material ($\theta = \theta_{sat}$) was enclosed in an impermeable casing made of polystyrene board that acted as insulator against heat and water. The impermeable casing with the pavement material inside it was placed in a controlled chamber (Fig. 26). Temperature and humidity of the chamber were

maintained at 30 °C and 50% respectively. The change in weight was monitored using A&D balance GX-K Series while four T-type thermocouples were embedded on the pavement surface to measure $T_s$.

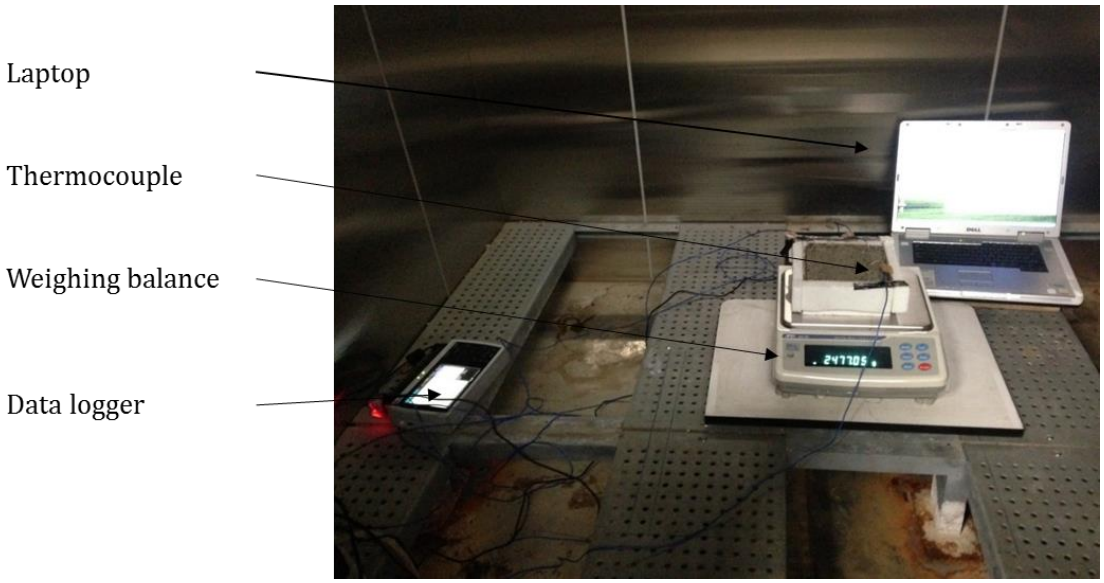


**Figure 26. Actual set-up inside the chamber.**

The parameter $\psi$ is a measure of water molecule adhesion to the pores of the pavement material. To determine $\psi$ a block of saturated WRP ($\theta = \theta_{sat}$) was placed in a vessel and subjected to different pressure. Figure 27 shows the schematic diagram of the experimental set up. The water within the material was forced out upon the application of pressure. This volume of water extracted was measured and the matric potential was calculated as a function of the volumetric water content obtained from the experiment. The relationship between $\psi$ and $\theta$ was expressed using the van Genuchten model (van Genuchten, 1980) shown in Eq. (35) and the hydraulic conductivity, $K_w$, was estimated using the Mualem model (Mualem, 1976) shown in Eq. (36). In this study, the matric potential of asphalt and bricks were not measured due to very low water content.

$$\theta = \theta_{sat}\left\{1 + \left(\frac{x}{|\psi|}\right)^{n}\right\}^{-m} \tag{35}$$

$$K_w = K_{sat}\left(\frac{\theta}{\theta_{sat}}\right)^{0.5}\left\{1 - \left(1 - \left(\frac{\theta}{\theta_{sat}}\right)^{\frac{1}{m}}\right)^{m}\right\}^{2} \tag{36}$$

where $\theta_{sat}$ is saturated volumetric water content, $x$ and $n$ are van Genuchten curve-fitting parameters, $\psi$ is matric potential, $m = 1 - (1/n)$ and $K_{sat}$ is saturated hydraulic conductivity.

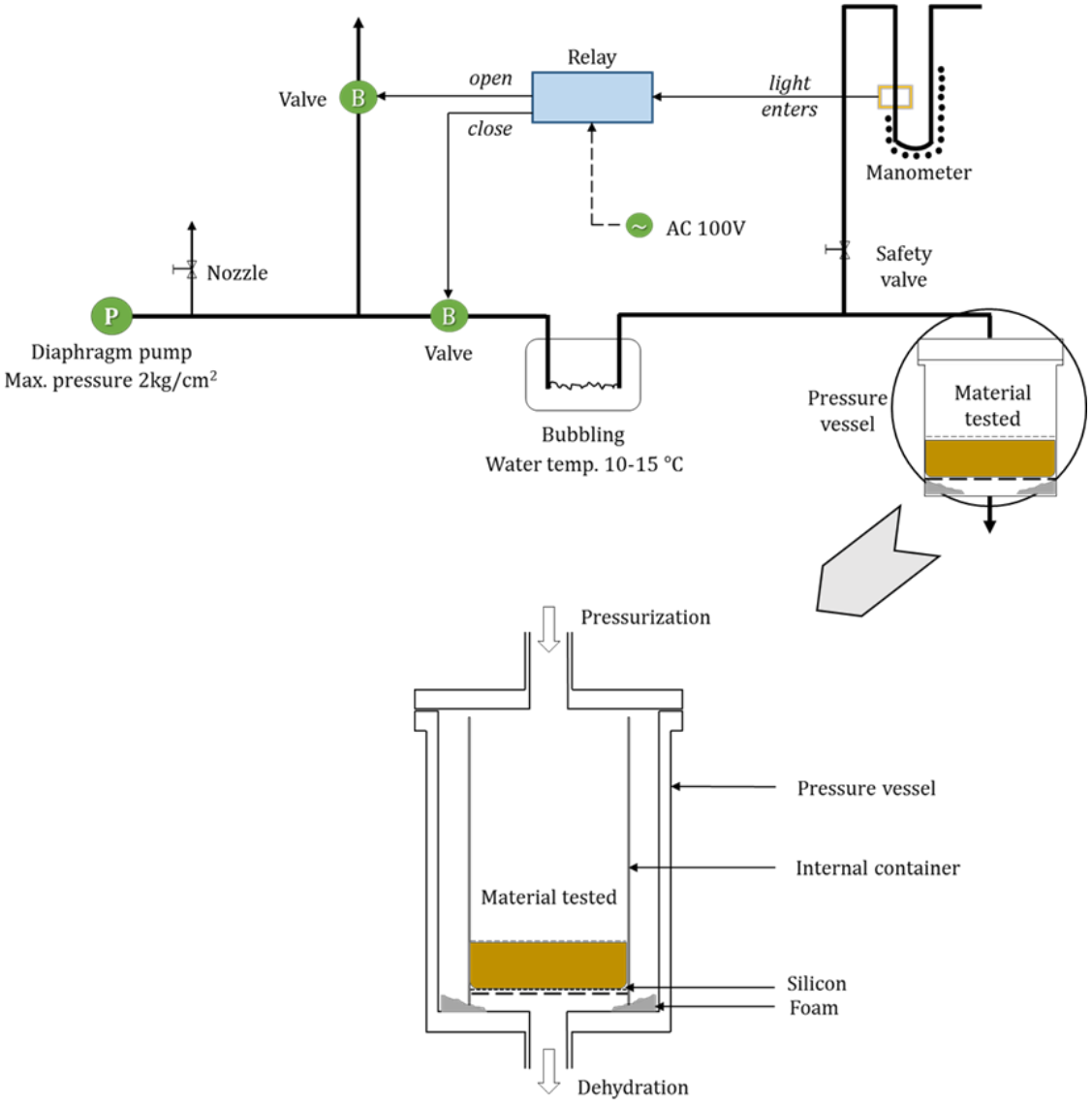


**Figure 27. Schematic diagram of the matric potential set-up.**

### 4.2.2 Governing equations

The PT model was composed of the following equations also obtained from Kondo *et al.* (1990): the one-dimensional conservation equations for soil moisture in liquid form (Eq. 37), soil moisture in vapor form (Eq. 38) and heat (Eq. 39).

$$\rho_w \frac{\partial \theta}{\partial t} = -\frac{\partial Q_{\theta,liq}}{\partial z} - E_{soil} \tag{37}$$

$$\frac{\partial \{\rho_{vap}(\theta_{sat} - \theta)\}}{\partial t} = \frac{\partial Q_{\theta,vap}}{\partial z} + E_{soil} \tag{38}$$

$$C \frac{\partial T}{\partial t} = -\frac{\partial Q_h}{\partial z} - \ell E_{soil} \tag{39}$$

where $\rho_w$ is liquid water density, $Q_{\theta,liq}$ is moisture flux, $z$ is depth, $E_{soil}$ is evaporation from soil surface, $\rho_{vap}$ is water vapor density, $Q_{\theta,vap}$ is water vapor flux, $C$ is the volumetric heat capacity and $Q_h$ is heat flux. The variables $E_{soil}$, $C$ and heat fluxes $Q_{\theta,liq}$, $Q_{\theta,vap}$ and $Q_h$ are given by the following:

$$E_{soil} = \rho D_{atm} \frac{q_s(T_s) - q_a}{R(\theta)} \tag{40}$$

$$D_{atm} = D_0 \left(\frac{T_s}{273.15}\right)^{1.75} \tag{41}$$

$$R(\theta) = \Delta F(\theta) \tag{42}$$

$$F(\theta) = D_{atm} \left(\frac{1}{C_E u \beta} - \frac{1}{C_E u}\right) \tag{43}$$

$$C = (1 - \theta_{sat}) C_{soil} + \theta C_{water} \tag{44}$$

$$Q_{\theta,liq} = -\rho_w K \frac{\partial \psi}{\partial \theta} \frac{\partial \theta}{\partial z} - \rho_w K \frac{\partial \psi}{\partial \theta} \frac{\partial T_s}{\partial z} - \rho_w K \tag{45}$$

$$Q_{\theta,vap} = -\rho D_{atm} f(\theta) \frac{\partial q}{\partial z} \tag{46}$$

$$f(\theta) = 0.66(\theta_{sat} - \theta) \tag{47}$$

$$Q_h = -\lambda \frac{\partial T_s}{\partial z} \tag{48}$$

where $D_{atm}$ is the diffusion coefficient for water vapor in the air, $R(\theta)$ is surface resistance, $D_0 = 0.3 \times 10^{-4}$, $F(\theta)$ is the resistance of the material's pores in the surface to vapor transport, $C_{soil}$ is the heat capacity of soil and $C_{water}$ is the heat capacity of water, $f(\theta)$ is tortuosity factor and $\lambda$ is pavement thermal conductivity.

### 4.2.3 Boundary conditions

The heat and moisture fluxes at the land surface were set as boundary condition and expressed below:

$$S(1-\alpha) + L\downarrow - \varepsilon'\sigma T_s^4 = H + \ell E + G \tag{49}$$

where $S$ is shortwave radiation (W/m$^2$), $\alpha$ is albedo, $L\downarrow$ is downward longwave radiation, $H$ is sensible heat flux, $\ell E$ is latent heat flux and $G$ is heat flux into the soil. The components $H$, $\ell E$, and $G$ can be written as:

$$H = \rho c_p C_H u(T_s - T_a) \tag{50}$$

$$G = -\lambda\left(\frac{\partial T}{\partial z}\right) \tag{51}$$

$$\ell E = \rho C_E u \frac{q_s(T) - q_a}{\left\{1 + \frac{C_E u F(\theta)}{D_{atm}}\right\}} \tag{52}$$

where $c_p$ is specific heat of air, $T_a$ is air temperature and $C_H$ is bulk coefficient for the sensible heat flux. Similar to the study of Kondo *et al.* (1990), $C_H$ was assumed to be equal to $C_E$. The values of the constants mentioned from Eq. (37) to (52) are listed in Table 6.

**Table 6. Initial constant values for transport model.**

| | Constants | | |
|---|---|---|---|
| | $\alpha$ | $\lambda$ | $C$ |
| WRP | 0.18 | 0.16 | $2.0\times10^6$ |
| Asphalt | 0.1 | 0.18 | $1.4\times10^6$ |

### 4.2.4 Model validation

In order to validate the model, outdoor experiment was performed on October 29–30, 2014 in Osaka University, Suita City (Fig. 28). Prior to the experiment, the pavement materials were prepared in a similar manner described in section 4.2.1. The change in

weight was monitored using A&D balance GX-K Series while surface temperature was measured using four T-type thermocouples. Surface temperature was also captured using FLIR infrared thermal camera. The shortwave and long wave radiation were measured using M-40 Longwave Shortwave Radiometer. Wind velocity at a height of 2 m near the observation site was measured using ultrasonic anemometer. Relative humidity at a height of 1.5 m near the observation site was measured using T&D humidity sensor. Air temperature readings were obtained from JMA-Toyonaka City observations (Japan Meteorological Agency, 2014). Due to the unavailable data for Suita City, observations in Toyonaka City were obtained which is closest to Suita City. A detailed description of the outdoor experiment can be found in Nakayama and Fujita (2010).

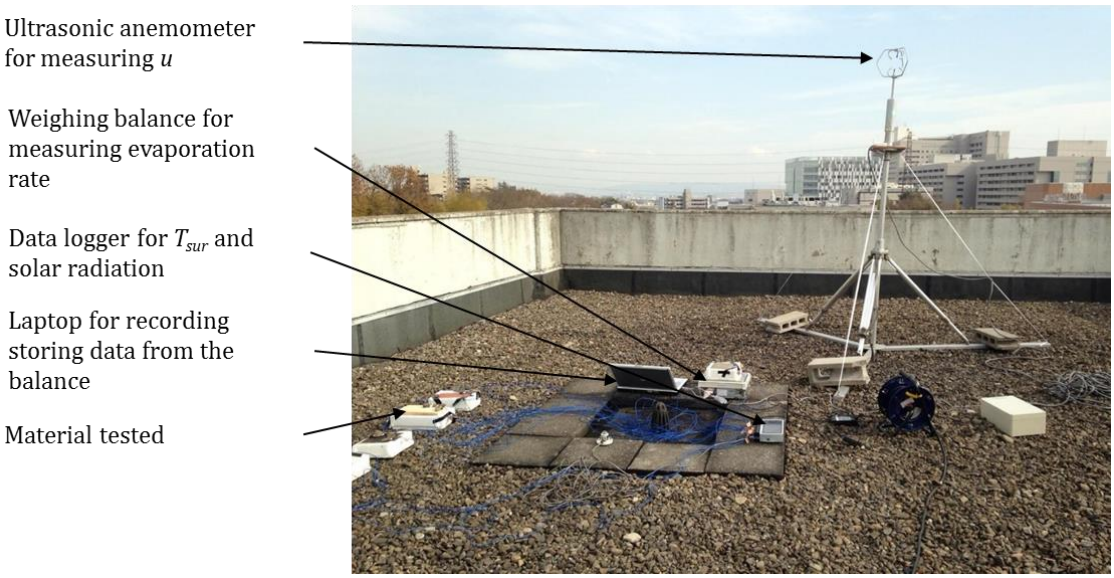


**Figure 28. Actual set-up of outdoor experiment on October 29–30, 2014.**

## 4.3 Results and discussion

### 4.3.1 Parameters

The WRP and Brick B had highest water content ($\theta_{sat} = 0.09$) compared with asphalt ($\theta_{sat} = 0.02$) and Brick A ($\theta_{sat} = 0.03$). This implies that WRP exhibit the same moisture holding capacity as Brick B. Naturally bricks are porous because of the clay composition which render its ability to attract water. Similarly, Li *et al.* (2013) attributes the water-holding characteristic of WRP to presence of numerous pores and that the fly ash additive improved water retention capacity.

In terms of the thermal and moisture performance, the $\theta$ decreased through time but

the rate of change was greater in WRP and Brick A, especially in the first 10 hr (Fig. 29). The $T_s$ increased through time but the rate of change was greater in asphalt and Brick B. Nevertheless, as $\theta$ decreased the $T_s$ of each pavement increased through time implying that these two parameters are inversely proportional.

The coefficient $\beta$ was calculated by first assuming a value of 1.0 at $t < 3$ where $\theta = \theta_{sat}$ and $T_s$ was constant. Using Eq. (1), the mean observed $C_E u$ for WRP was approximately 0.02. This $C_E u$ was used to calculate for $\beta$ at $t > 3$ and the $F(\theta)$ in Eq. (43). Figure 30 shows that $\beta$ and $\theta$ of WRP were directly proportional i.e. $\beta$ decreased as $\theta$ decreased. For asphalt, there was no significant change in $\theta$ because it did not have a water-retaining ability similar with that of WRP.

The behavior of $\beta$ is opposite to the behavior of $F(\theta)$ i.e. at $F(\theta) = 1$ resistance to evaporation is greatest while $F(\theta)$ near zero means least resistance to evaporation. It can be seen in Fig. 31 that $F(\theta)$ and $\theta$ were also inversely proportional similar to the relationship between $T_s$ and $\theta$. This implies that when a material contains water near its saturation value, resistance to evaporation is very weak. Therefore, water can easily be transported from material's surface to the atmosphere.

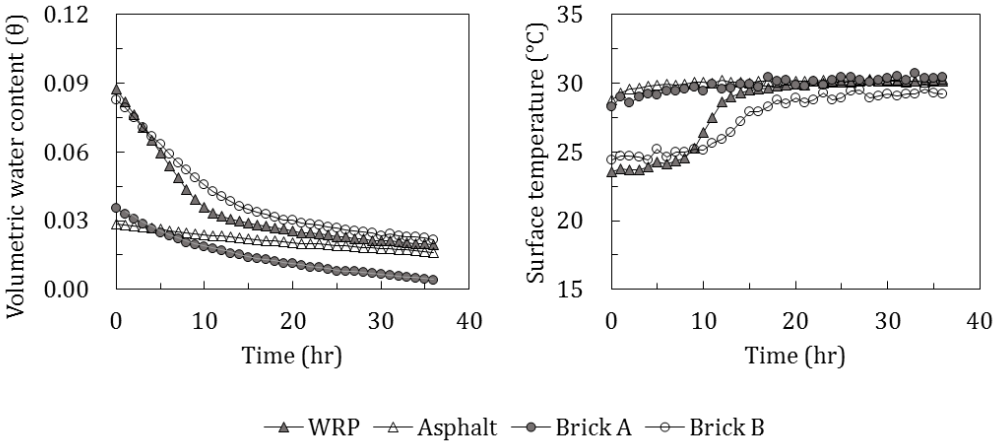


**Figure 29. The moisture and thermal performance of pavement materials.**

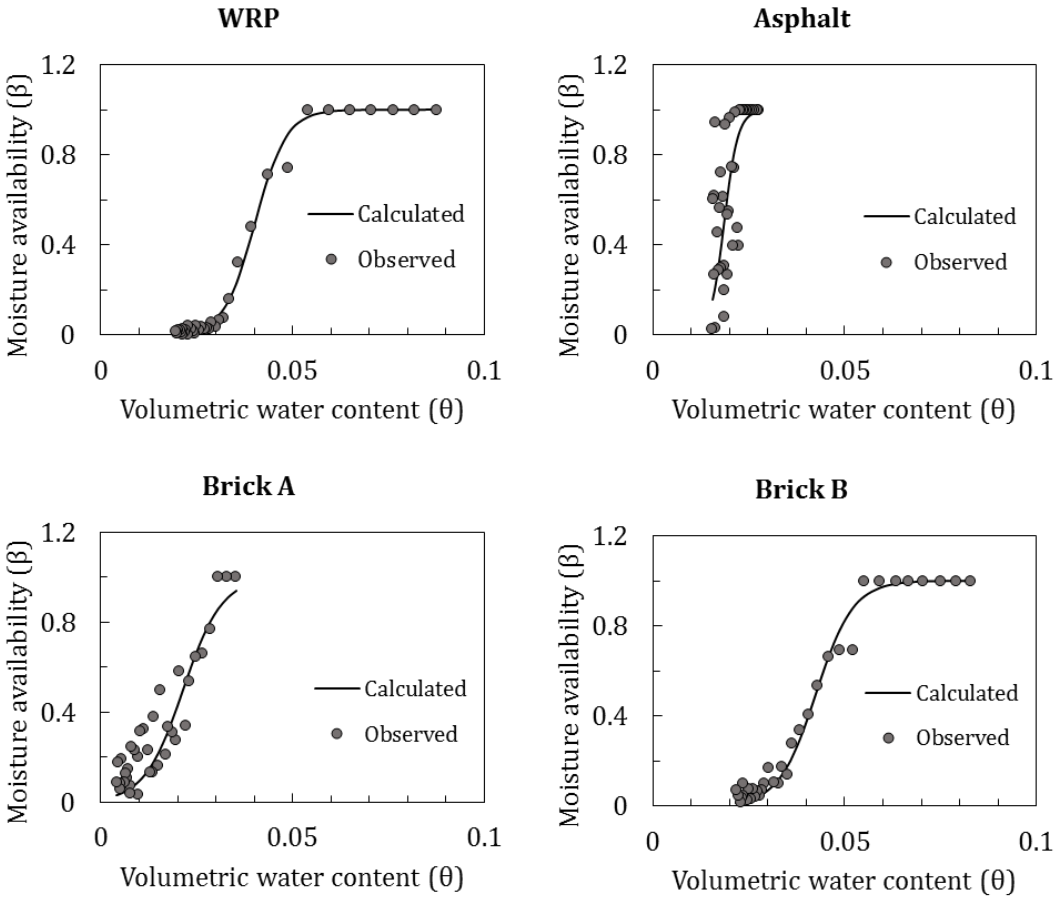


**Figure 30. The relationship of evaporation efficiency and water content.**

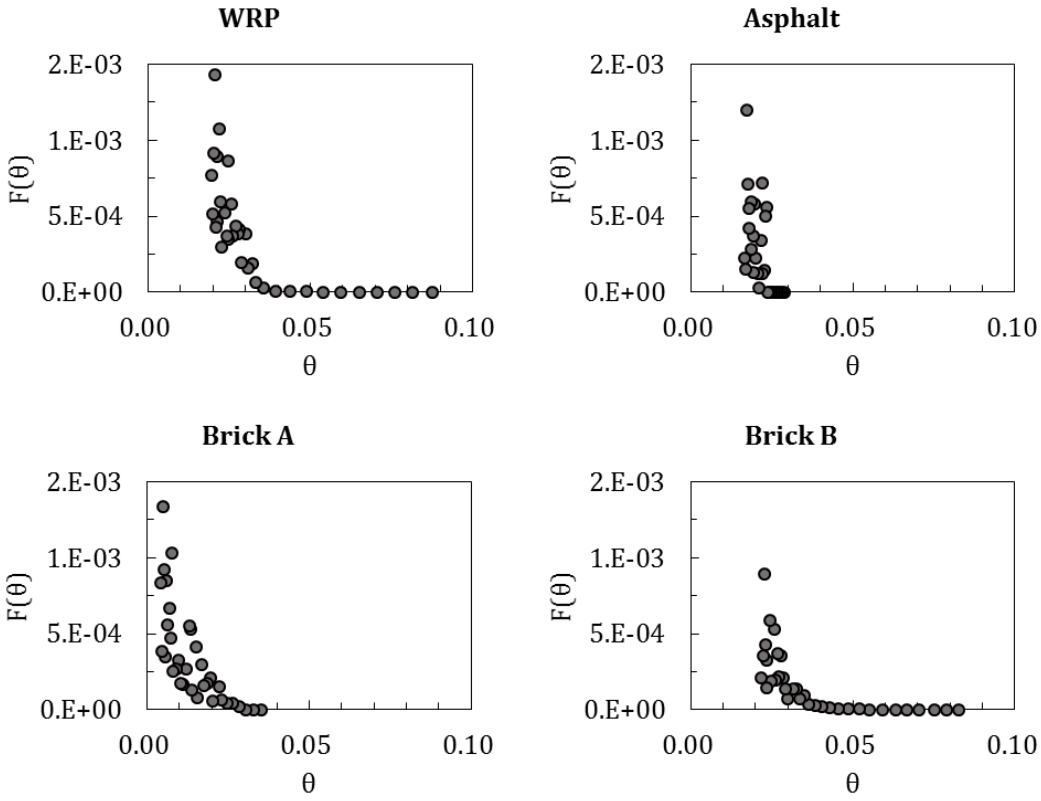


**Figure 31. The relationship of vapor transport resistance and water content.**

Results of the matric potential experiment showed that similar to $\beta$ and $F(\theta)$, $\psi$ was also greatly affected by $\theta$ (Fig. 32). The matric potential of WRP was near zero during saturation, which implies that water can easily be transported during this time. The findings of Daamen and Simmonds (1996) demonstrated that matric potential is a function of $\theta$ and $K$. A summary of the initial parameter values set for the calculation of heat and moisture transport is listed in Table 7.

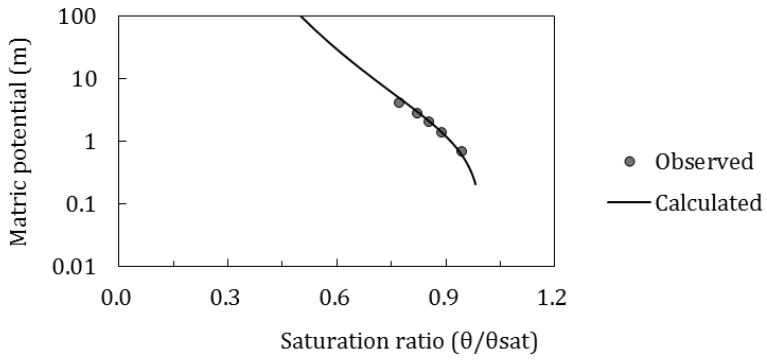


**Figure 32. Effect of water saturation ratio on matric potential.**

**Table 7. Values of parameters used for transport model**

| | Measured values | | | | | | |
|---|---|---|---|---|---|---|---|
| | At the start of outdoor experiment | | From chamber experiment | | From matric potential experiment | | |
| | $\theta$ | $T_s$(°C) | $\theta_{sat}$ | $C_E u$ | $x$ | $n$ | $m$ |
| WRP | 0.07 | 5.5 | 0.09 | 0.02 | 1 | 1.1 | 0.1 |
| Asphalt | 0 | 5.5 | 0.02 | - | - | - | - |

### 4.3.2 Outdoor observations

For outdoor observations, only asphalt and WRP were observed. Figure 33 shows the weather measurements on October 29-30, 2014 that were used as input data for the model. This period was mostly sunny, however, it was also the start of autumn so that there was a large difference between daytime (06:00-17:00 JST) and nighttime (18:00-05:00 JST) air temperature. Maximum ambient air temperature during daytime was 32.1 °C; minimum ambient air temperature at nighttime was 6.9 °C. Average specific humidity and wind speed were 5.7 × $10^{-3}$ g/kg and 2.6 m/s respectively. Under these conditions, the evaporation rate of WRP was measured every 30 min for 36 hr (Fig. 34). Results show that evaporation rate significantly increased from 10:00 JST and reached a peak during noontime.

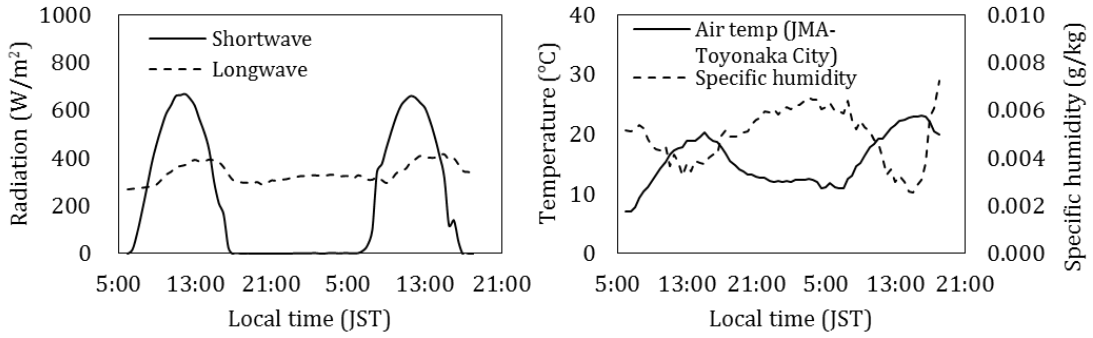


**Figure 33. Diurnal variation in radiation, air temperature and specific humidity on October 29–30, 2014.**

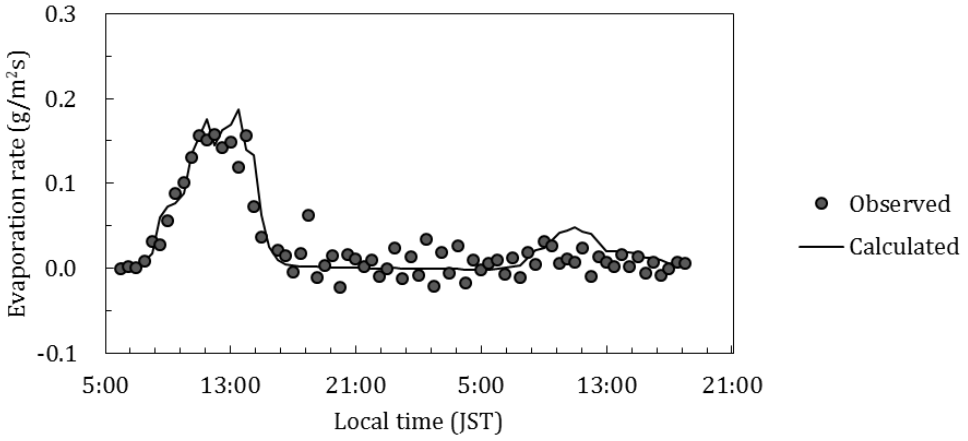


**Figure 34. Diurnal variation in WRP evaporation rate.**

Figure 35 shows the surface temperature measured from thermocouple and thermal camera. The infrared thermal camera readings shown at every 6 hr agree with the measured values from thermocouple. Comparing pavement materials, asphalt had warmer surfaces than WRP. There was maximum surface temperature difference from 10:00 JST to 15:00 JST, with asphalt 9.1 °C warmer than WRP. Minimum surface temperature difference was observed from 22:00 to 06:00 JST, with asphalt 0.3 °C warmer than WRP. Comparing the time of day, surface temperature of both pavements were warmer during daytime compared with nighttime. As the solar radiation heated up the pavement, the water within the material evaporated which eventually led to cooling. The greater water content in WRP led to higher evaporation rate compared with asphalt; this explains the large surface temperature difference between the two pavements during daytime. Higher albedo can also account for the lower temperature of WRP (Nakayaman & Fujita, 2010; Takebayashi & Moriyama, 2012). In this study, the higher albedo of WRP (Table 6) was made obvious by its gray color compared with the black asphalt.

### 4.3.3 Results of the transport model

Figure 36 shows the comparison between observed values of surface temperature ($T_{s,obs}$) and calculated values ($T_{s,calc}$). For WRP, the model underestimated the surface temperature at an average of 2.0 °C from 13:00 JST to 07:00 JST. For asphalt, the model underestimated the surface temperature at an average of 4.0 °C from 13:00 JST to 17:00 JST and overestimated at an average of 2.2 °C from 17:00 JST to 05:00 JST. The estimated error ($EE$) based on Kinoshita *et al*. (2012) was used to evaluate the overall accuracy of the model (Eq. 53). Average $EE$ were 10.6% and 15.7% for WRP and asphalt respectively, which implies

that the simulation results were accurate.

$$EE = \frac{T_{s,obs} - T_{s,calc}}{T_{s,obs}} \times 100 \tag{53}$$

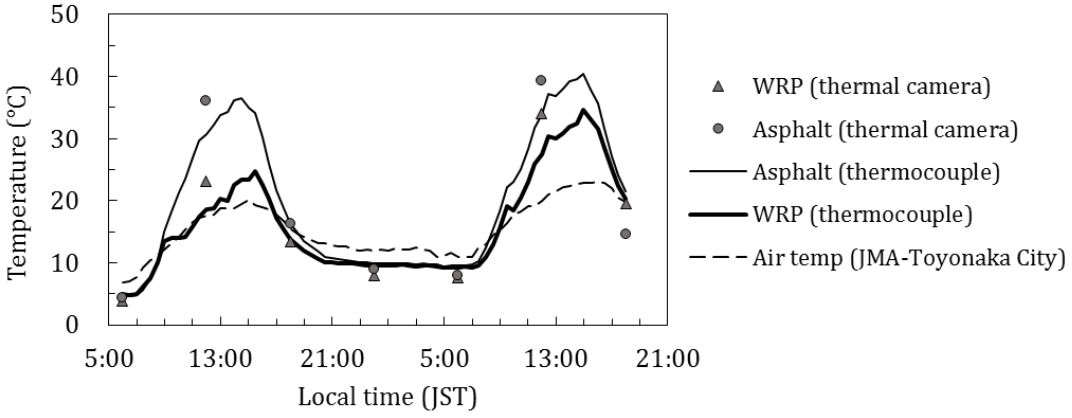


**Figure 35. Observed surface temperature on WRP and asphalt on October 29–30, 2014.**

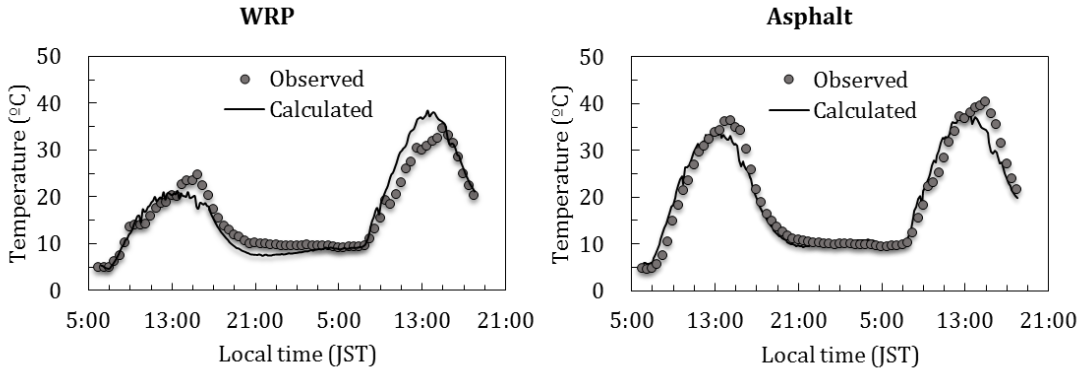


**Figure 36. Comparison on the observed and calculated surface temperature.**

Figure 37 shows the temporal change in temperature profile within WRP and asphalt every 4 hr. Temperature profile for both pavements were similar, i.e. surface temperature was higher compared with the underlying layers during daytime. This can be further validated by looking at the volumetric water content profile (Fig. 38), where $\theta$ of the surface was significantly lower than the underlying layers.

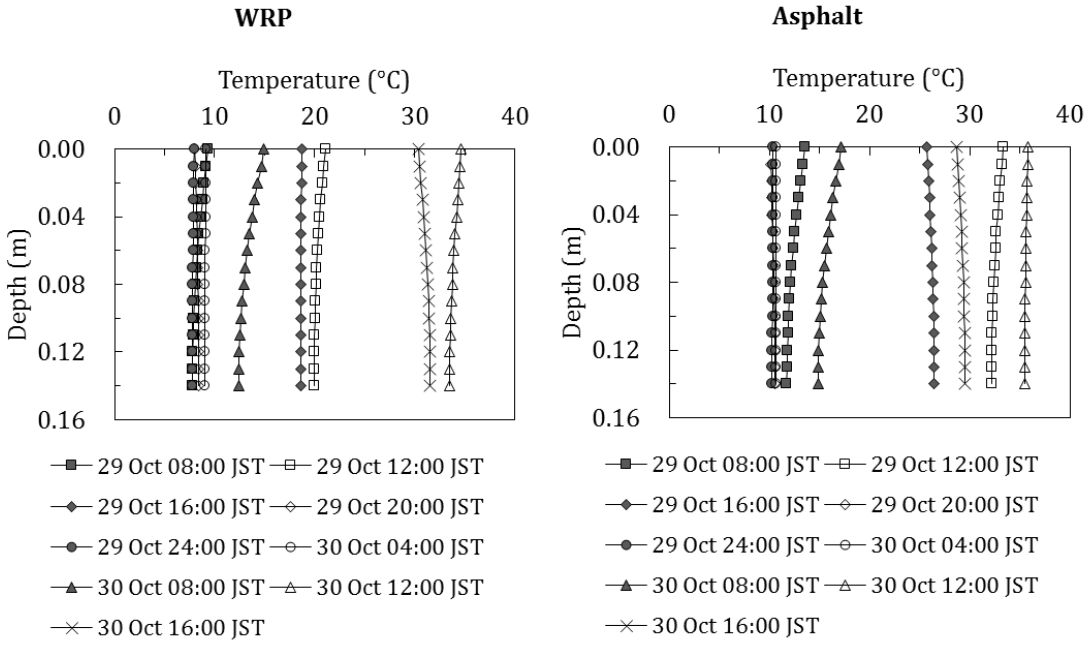


**Figure 37. Diurnal variation in temperature profile within the pavement material.**

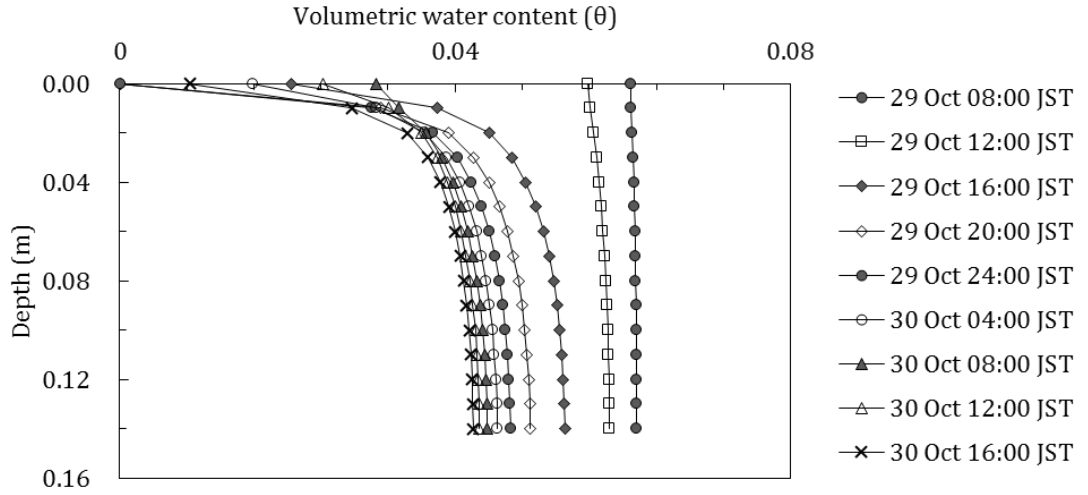


**Figure 38. Volumetric water content profile from surface to bottom layer.**

Results of the temperature and water content profile imply that evaporation occurs first on the surface; this coincides with the findings of Kinoshita *et al.* (2012). In contrast, surface layer had cooler temperature compared with the underlying layers during nighttime. It can be attributed to the pavement heat capacity and the low ambient air temperature during the night where $T_a < 14$ °C. The high heat capacity of WRP and asphalt allowed heat to be absorbed during daytime and released later at night. The absorbed heat was only able to

heat the underlying layers because during nighttime the drop of ambient air temperature highly influenced the surface temperature. The heat transfer was delayed from the inner of the pavement towards the surface, making the surface cooler at night. Water vapor condensation may have also occurred on the surfaces of the pavement which was most likely promoted by the high moisture content in the air (Fig. 33).

Calculation results of the heat fluxes in WRP (Fig. 39) showed an average latent heat flux of 113 W/m$^2$ and 42 W/m$^2$ during the first and second day respectively. Average sensible heat flux was 0.8 W/m$^2$ during the first day and increased to 57 W/m$^2$ on the second day. Average daytime net radiation was 328 W/m$^2$ during the first day and decreased to 293 W/m$^2$ on the second day. Average nighttime net radiation was -41 W/m$^2$. Average conductive heat flux during nighttime was 28 W/m$^2$.

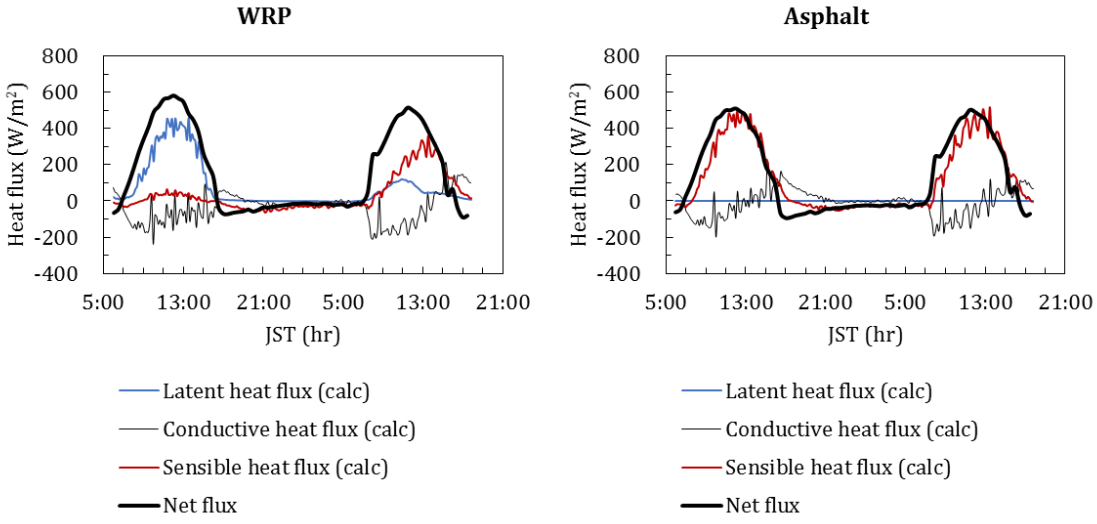


**Figure 39. Estimated surface heat budget for WRP and asphalt.**

In case of asphalt, latent heat flux was assumed to be zero throughout the experiment, implying that evaporation did not occur. As a consequence, sensible heat flux was similarly high on both days with an average of 171 W/m$^2$. Average daytime net radiation was 269 W/m$^2$ during the first day and decreased to 256 W/m$^2$ on the second day. Average nighttime net radiation was -62 W/m$^2$. Average conductive heat flux during nighttime was 38 W/m$^2$. Based on the estimated heat fluxes mentioned above, the reduction in daytime sensible heat flux by WRP compared with asphalt was 142 W/m$^2$. Reduction in nighttime conductive heat flux by WRP compared with asphalt was 31 W/m$^2$. Average increase in daytime net radiation by WRP compared with asphalt was 59 W/m$^2$ while average increase in nighttime net radiation was 21 W/m$^2$. Sensible and conductive heat flux reduction was considered to be

influenced by surface temperature. Meanwhile, overall increase of net radiation was considered to be influenced by the significant decrease in longwave radiation and albedo.

## 4.4 Conclusions

Using the parameters volumetric water content, matric potential and evaporation efficiency, it is now known that the WRP made from fly ash has cooling properties. Surface temperature and matric potential are indirectly proportional to volumetric water content. On the other hand, WRP evaporation efficiency is maximum when water content is at saturation. It is also proven that the thermal and hydraulic performance of WRP is better than asphalt. Despite the overestimation and underestimation during specific time of the day, the model can numerically evaluate the diurnal variation in surface temperature with minimal estimated error. Evaporation of water from WRP occurs first in the surface and this behavior greatly influence the temporal variation of temperature and moisture profile. The increase in latent heat flux and net radiation by WRP render its cooling ability. The decrease in sensible and conductive heat flux by WRP can potentially cool the surrounding environment.

# 5. NUMERICAL ASSESSMENT OF WRP

## 5.1. Introduction

As mentioned in Chapter 1, the warming of urban surfaces such as streets and buildings has been proven to be one major contributing factor to urban heat island or UHI phenomenon (Asaede and Ca, 1993; Asaede and Ca, 1996; Asaeda and Ca, 2000; Golden & Kaloush, 2006; Oke, 1982). Thus, mitigation strategies that improve urban surfaces could be most effective in moderating UHI. For example, the use of "cool pavements" have been gaining popularity. A pavement is considered "cool" if it has high albedo and high emissivity or it has high latent heat of evaporization (Santamouris, 2013). A number of studies investigated the thermal and moisture characteristics of pavement materials with high latent heat flux of evaporization, referred to as water retentive pavement or WRP (Asaeda & Ca, 2000; Cortes *et al.*, 2016; Kinoshita *et al.*, 2012; Misaka *et al.*, 2009; Takebayashi & Moriyama, 2012; Ueno & Tamaoki, 2009; Yamamoto *et al.*, 2006). Other studies also evaluated the thermal performance and effectiveness of high albedo, reflective pavements (Guntor *et al.*, 2014; Kawakami & Kub, 2008; Wan & Hien, 2012). The combined effect of both reflective and permeable pavements as UHI mitigation was also examined (Li *et al.*, 2012; Takebayashi *et al.*, 2014). Very few studies evaluated the performance of these pavements in an urban set-up. Nayakama and Fujita (2010) coupled the NIES Integrated Catchment-based Eco-hydrology model with urban canopy model to evaluate the role of

retentive pavements in UHI mitigation. They found out that air temperature above the WRP is much lower than the air temperature above lawn or building rooftop. Georgakis *et al.* (2014) evaluated cool pavements and roof coated with high reflection paints as UHI mitigation. They used CFD model to calculate surface temperature and air temperature within the urban canyon. Their model estimated a 7-8 °C decrease in surface temperature at ground level. However, none of the existing studies evaluated the pavement performance when used in a real city. In this chapter, the effect of using WRP as material for main street in a real city block was evaluated. Suita City was chosen for analysis because important parameter information such as building height and coverage were available. Suita City is also one of the main cities in Osaka Prefecture and its urban environment has not been modeled yet. Here, CFD model was used to examine energy balance in the building canopies and coupled it with the PT model previously discussed in Chapter 4. The PT model calculated for ground surface energy balance, ground surface temperature and ground surface water content. This chapter aims to (1) predict diurnal variation in air temperature, wind speed, ground surface temperature and water content; (2) compare ground surface energy fluxes.

## 5.2 Methods of analysis

### 5.2.1 Area of analysis

The Suita City government had selected two regions within the city where UHI mitigation strategies shall be implemented (Suita City, 2016). One of these regions is Esaka, the analysis area, which is a highly urbanized district with major roads, residential and industrial buildings. Prior to simulation, a 3D model of Esaka was created as shown in Fig. 40. The 3D model was then divided into meshes with a grid interval of 5 m. Figure 41 shows the domain size and the analyzed area surrounded by the solid line. There were 22 buildings with the highest building being 56 m. The total mesh number in the CFD model was 80 × 77 × 47 including the virtual space. For the PT model, which is one dimensional, the total mesh number was 16 with a grid interval of 0.01 m.

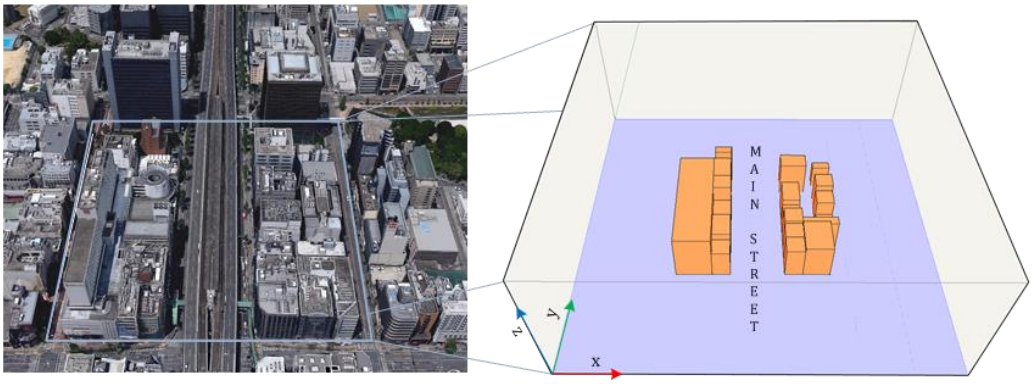


**Figure 40. Esaka district as seen from Google Earth (2015) and its corresponding 3D model.**

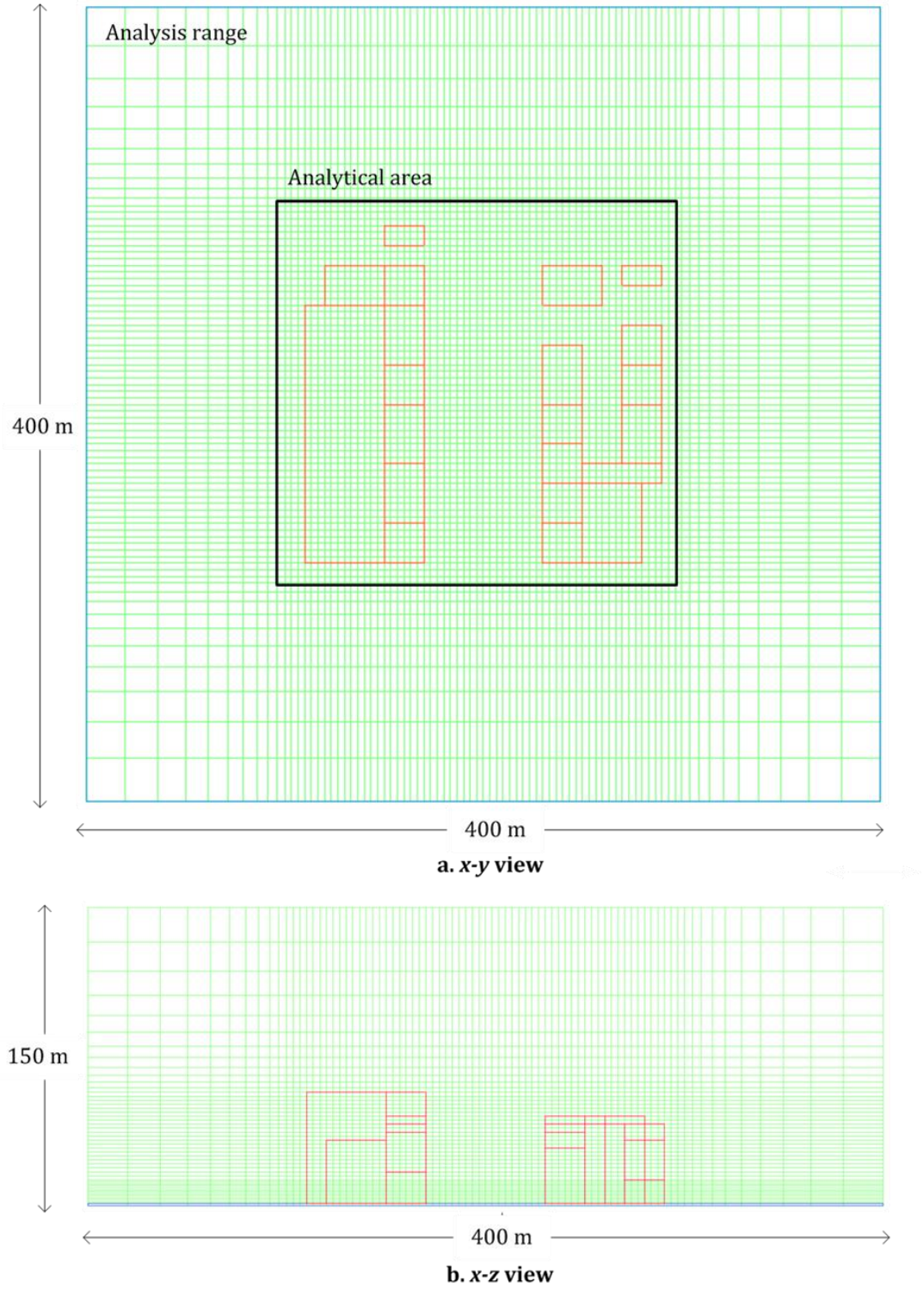


**Figure 41. Mesh view of the calculated domain.**

### 5.2.2 Boundary conditions

Two WRF domains were established, first the larger Kansai region as D1 and Osaka Prefecture as D2 (Fig. 42). Results of the WRF simulation for Suita City are shown in Figure 43.

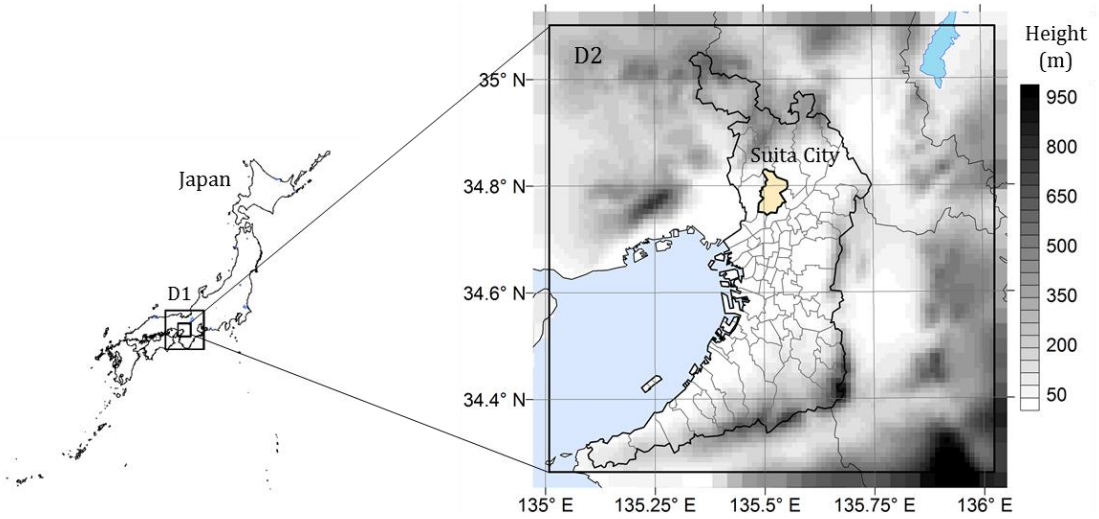


**Figure 42. The WRF domains showing Kansai region as D1 and Osaka as D2.**

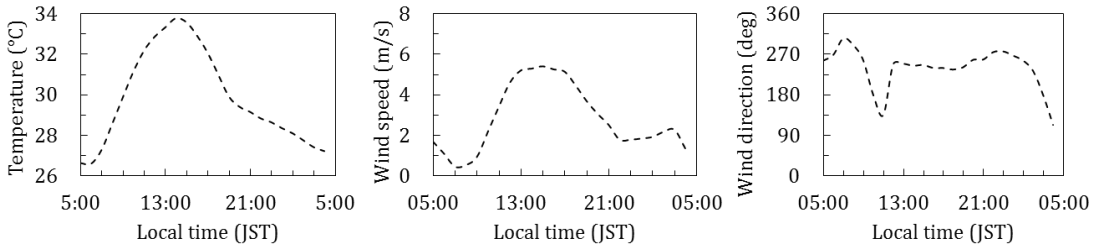


**Figure 43. Diurnal variation in air temperature, wind speed and wind direction in Suita City on August 8–9, 2011.**

Owing to the coarser vertical resolution of WRF model compared with CFD, MOST was applied. Figure 44 shows the vertical distribution of air temperature and $u$, $v$ wind components. Air temperature was warmer in the surface layer especially during noon. Wind direction was south-west throughout the day. Wind speed was weakest at 08:00 JST and strongest at 16:00 JST.

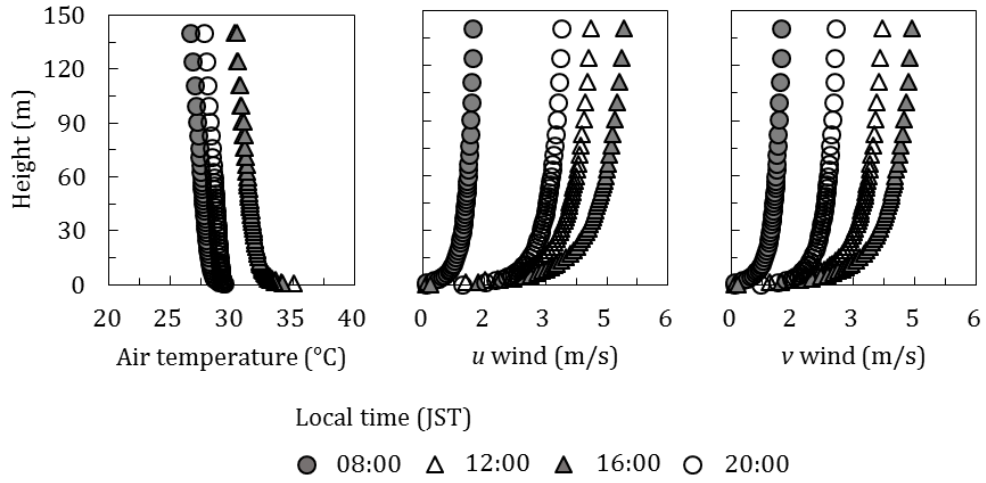


**Figure 44. Vertical distribution of air temperature and *u*, *v* wind components.**

### 5.2.3 The CFD-PT Model

The CFD model was composed of the conservation equations for momentum, continuity and mass described in Chapter 2. The CFD model calculated for air temperature, wind speed, air humidity, downward longwave radiation and shortwave radiation and supplied these parameters to the PT model.

There were two surface energy budget model incorporated into the CFD model. One is the BEM, used to calculate heat transfer from building surface to atmosphere. Second is the PT model which simulates heat transfer from ground surface to the atmosphere. The PT model was composed of conservation equations for heat and soil moisture presented in Chapter 4. The PT model calculation time step was 60 s.

In this study we were interested in determining the maximum performance of WRP hence the initial $\theta$ was set at saturation level (Table 1) and we did not consider other scenarios like varying initial $\theta$. The ground surface energy balance was solved using Eq. (49). The initial values of parameters used in CFD-PT model are listed in Table 1. Two cases of 24-h unsteady analysis were simulated. In case 1 ($c_1$), asphalt was used as the pavement material of all ground surface. In case 2 ($c_2$), WRP was used as the pavement material of the main street and asphalt for the rest of the ground surface.

**Table 8. Value of the parameters used for WRP assessment.**

| Parameter | Value | |
|---|---|---|
| | **Asphalt** | **WRP** |
| Pavement thickness | 0.15 m | 0.15 m |
| Albedo | | |
| Ground | 0.1 | 0.14 |
| Building roof | 0.1 | 0.1 |
| Building wall | 0.1 | 0.1 |
| Heat capacity | | |
| Water | $4.2\times10^6$ J/m$^3$K | $4.2\times10^6$ J/m$^3$K |
| Ground | $1.4\times10^6$ J/m$^3$K | $2.0\times10^6$ J/m$^3$K |
| van Genuchten-Mualem model constants | | |
| $n$ | - | 1.15 |
| $m$ | - | 0.13 |
| $x$ | - | 1.01 |
| Water content | | |
| Initial | 0.01 | 0.09 |
| Saturation | 0.02 | 0.09 |
| Thermal conductivity | 0.18 W/mK | 0.14 W/mK |
| Roughness layer | 0.0003 m | 0.0003 m |
| Convective heat transfer coefficient | 0.83 W/ m$^2$K | 0.83 W/ m$^2$K |
| Emissivity | 0.90 | 0.90 |
| Initial temperature | | |
| Room | 28 °C | 28 °C |
| Ground | 28 °C | 28 °C |

## 5.3 Results and discussion

### 5.3.1 Effect on ground surface temperature

Examining the average diurnal variation in ground surface temperature within the analysis area (Fig. 45), it can be seen that $T_s$ in $c_2$ was consistently lower throughout the day. As Cortes *et al.* (2016) pointed out, the cooling property of WRP compared with asphalt can be attributed to three factors namely water content, albedo and thermal conductivity. However, by creating a graphical representation of the diurnal variation in $T_s$, it was discovered that shadow effect also contributed to a decrease in surface temperature (Fig.

46). True for both $c_1$ and $c_2$, $T_s$ on the western side of the buildings decreased at 08:00 JST. During this time the shadow formed on the west as the sun rose in the east.

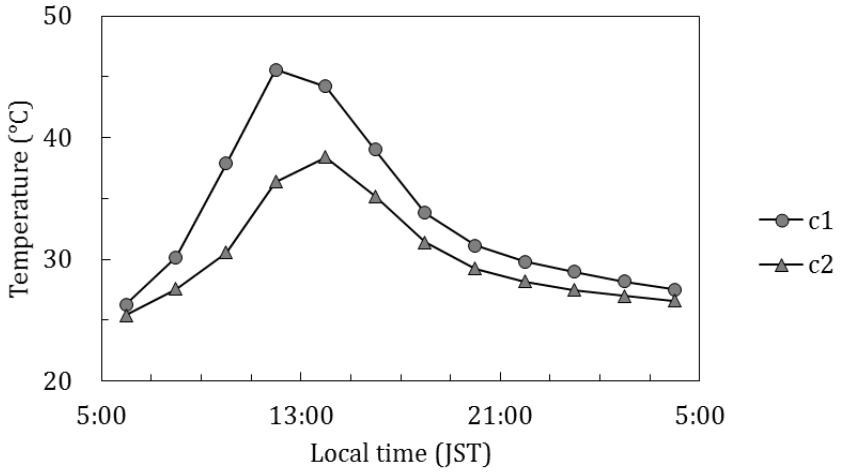


**Figure 45. The diurnal variation in ground surface temperature, *Ts*, within the analysis range for 24-h time period.**

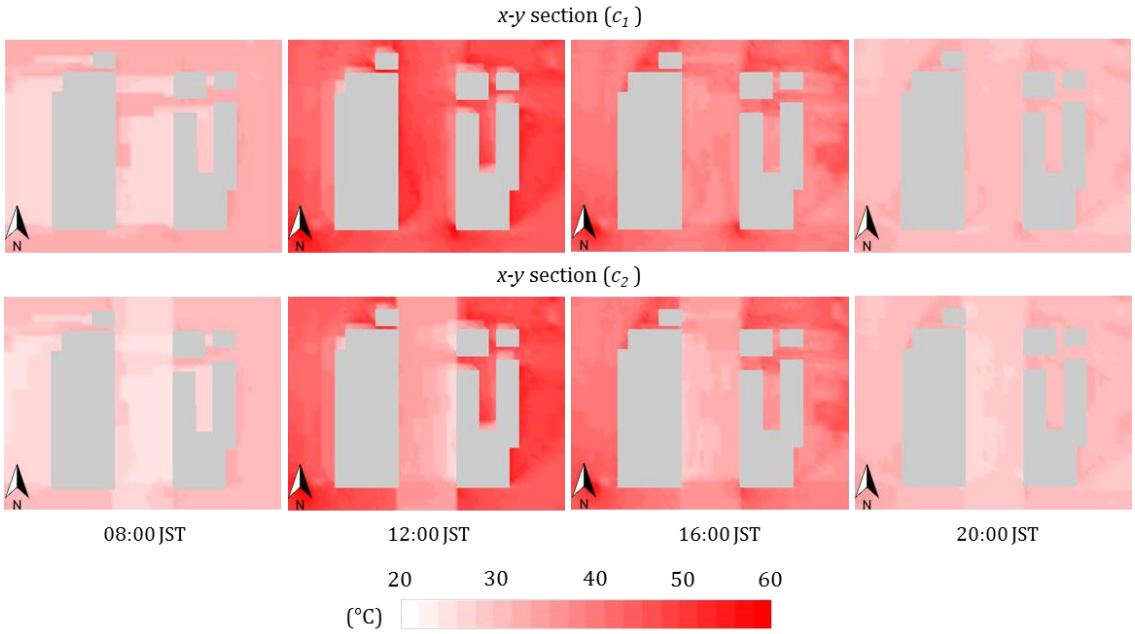


**Figure 46. The *x-y* view of ground surface temperature, *Ts*, in each case.**

Here we focus the discussion to the difference between main street $T_s$ in $c_1$ and $c_2$. Results show that $T_s$ in $c_2$ main street decreased by 3.1 °C at 08:00 JST. We attribute this to the greater water content of WRP compared with asphalt which led to evaporative cooling and

increased latent heat flux (discussed in section 5.3.3). This agrees with the study of Asaeda (1993) on evaporation in bare soil where the transport of water vapor inside soil affects subsurface distribution of temperature greatly. Due to evaporation, bare soil is cooler than covered surfaces such that increase in thickness of the covering material cause temperature increase and higher heat stored. Similar to bare soil, the ability to hold water and the porosity of WRP allows for water transport thus affecting subsurface distribution of temperature.

It can be seen in Fig. 47 that at 08:00 JST, the average water content of WRP was 0.08 which still near to the saturation level of 0.09. At 12:00 JST the water content decreased to 0.05, the greatest change throughout the day. This can be expected because at noontime, the sun was most intense. Increased solar radiation further promoted evaporation of water from surfaces. It also explains the greatest difference in $T_s$ between $c_1$ and $c_2$ too; during this time, $T_s$ in $c_2$ main street decreased by 13.8 °C. From 16:00 JST to 20:00 JST the surface water content remained at 0.04 but the surface temperature continued to decrease. At 16:00 JST and 20:00 JST, $T_s$ of $c_2$ main street decreased by 5.7 °C and 2.9 °C. respectively. We attribute this to both higher albedo and lower thermal conductivity of WRP compared with asphalt (Table 8). Both factors allowed reflection of sunlight during daytime and minimized the release of heat during night time. These estimates of main street $T_s$ between $c_1$ and $c_2$ were proximate to the observations of Cortes *et al.* (2016) on the behavior of asphalt and WRP in an outdoor set-up (see section 4.3.2).

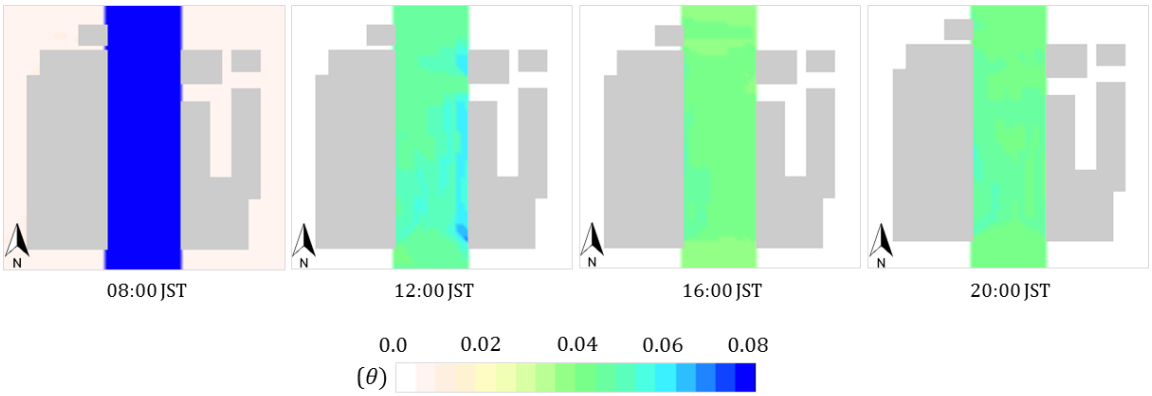


**Figure 47. Diurnal variation in water content, $\theta$, in $c_2$ main street surface.**

### 5.3.2 Effect on air temperature

This section discusses the effect of WRP on diurnal variation in air temperature. The CFD-PT model estimated an overall decrease in air temperature at 1.5 m within the analysis area (Fig. 48). The average air temperature difference over main street was computed as $c_1 T_{air} - c_2 T_{air}$ (Fig. 49). Results show that air temperature in $c_2$ decreased by 0.05 °C at 0800 JST, 0.3 °C at 12:00 JST, 0.1 °C at 16:00 JST and 0.06 °C at 20:00 JST. The air temperature decrease was most pronounced at 12:00 JST which is proportional to the degree of surface temperature cooling. Looking at the *x-y* section, the decrease is particularly noticeable on the western side of the main street area. This can be attributed to the stronger wind towards north-west direction which is evident in the wind profile. By examining the *x-z* section, it can be seen that there was greater air temperature decrease above WRP surface of main street compared with asphalt surface of none main street areas, confirming the occurrence of evaporative cooling. Moreover, there was also vortex formation within the street canyon. This vortex allowed for mixing of air that eventually caused cooler air from the ground to rose.

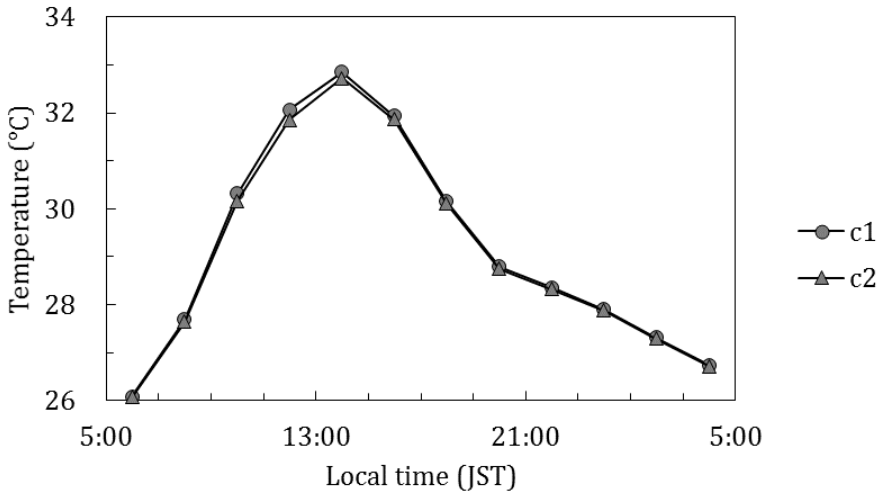


**Figure 48. The diurnal variation in air temperature at 1.5 m above ground surface.**

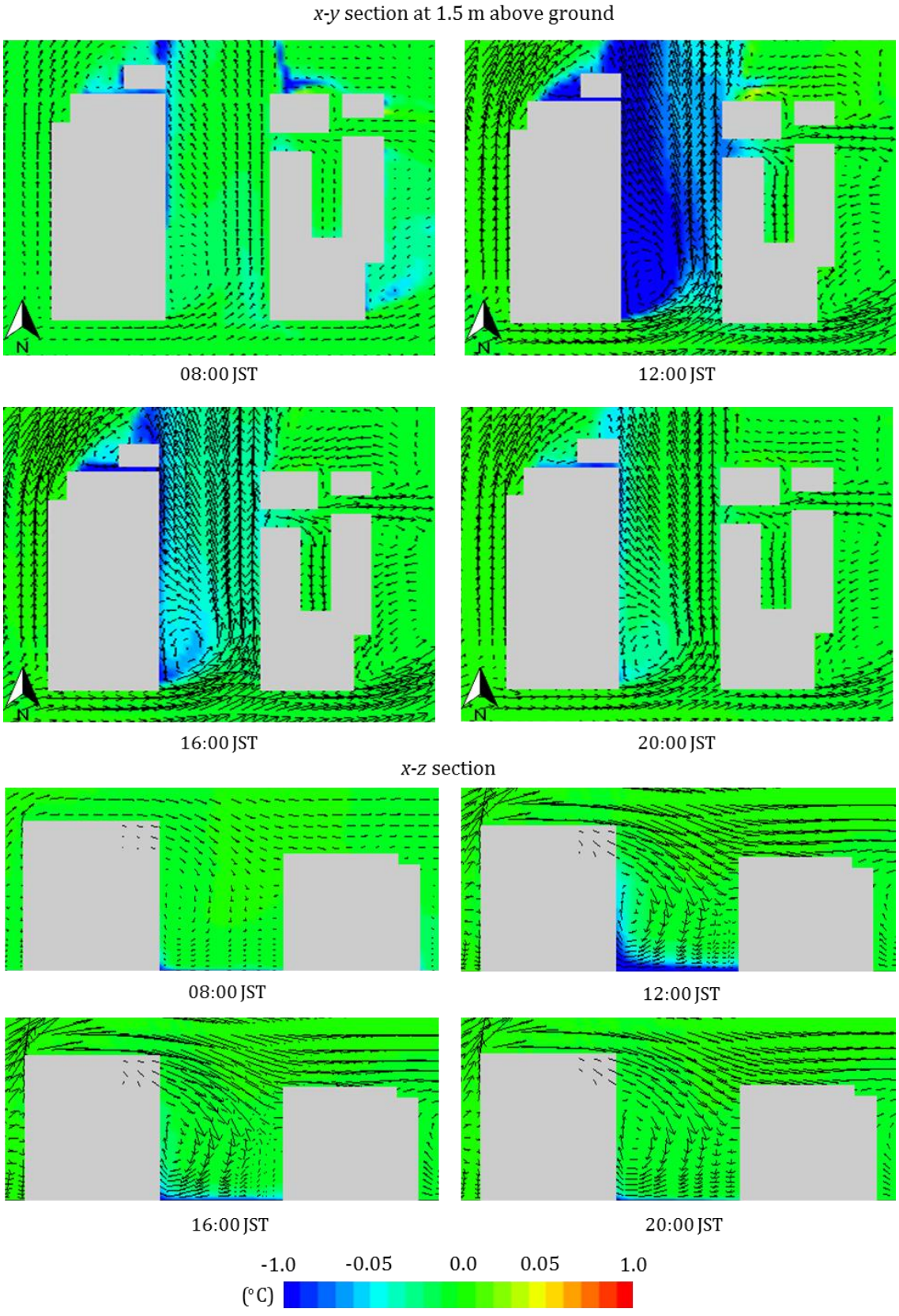


**Figure 49. The wind profile and effect of WRP on air temperature.**

### 5.3.3 Effect on ground surface energy fluxes

Figure 50 shows the diurnal variations in ground surface energy fluxes within the analysis area. Results show an overall increase in latent heat flux and decrease in sensible heat flux, conductive heat flux and upward longwave radiation throughout the day. Due to the significant decrease in main street $T_s$, a comparison of the surface energy fluxes in the same area was also carried out. The ground surface energy flux difference over main street was computed as $c_1$ heat flux – $c_2$ heat flux. The model estimated an average increase in latent heat flux by up to 51 W/m$^2$ at 08:00 JST, 255 W/m$^2$ at 12:00 JST, 68 W/m$^2$ at 16:00 JST and 34 W/m$^2$ at 20:00 JST. This diurnal variation in latent heat flux was also relative to the diurnal variation in water content discussed previously. As the sun started to become intense from morning to noon, evaporation rate also increased dramatically. Consequently, this increase in latent heat flux caused a particularly slight difference between $T_s$ and $T_a$, allowing for a distinct decrease in sensible heat flux. As expected from the increase in latent heat flux, maximum decrease in sensible heat flux occurred at 12:00 JST. During this time sensible heat flux in $c_2$ decreased by 465 W/m$^2$. The longwave radiation also decreased by 97 W/m$^2$.

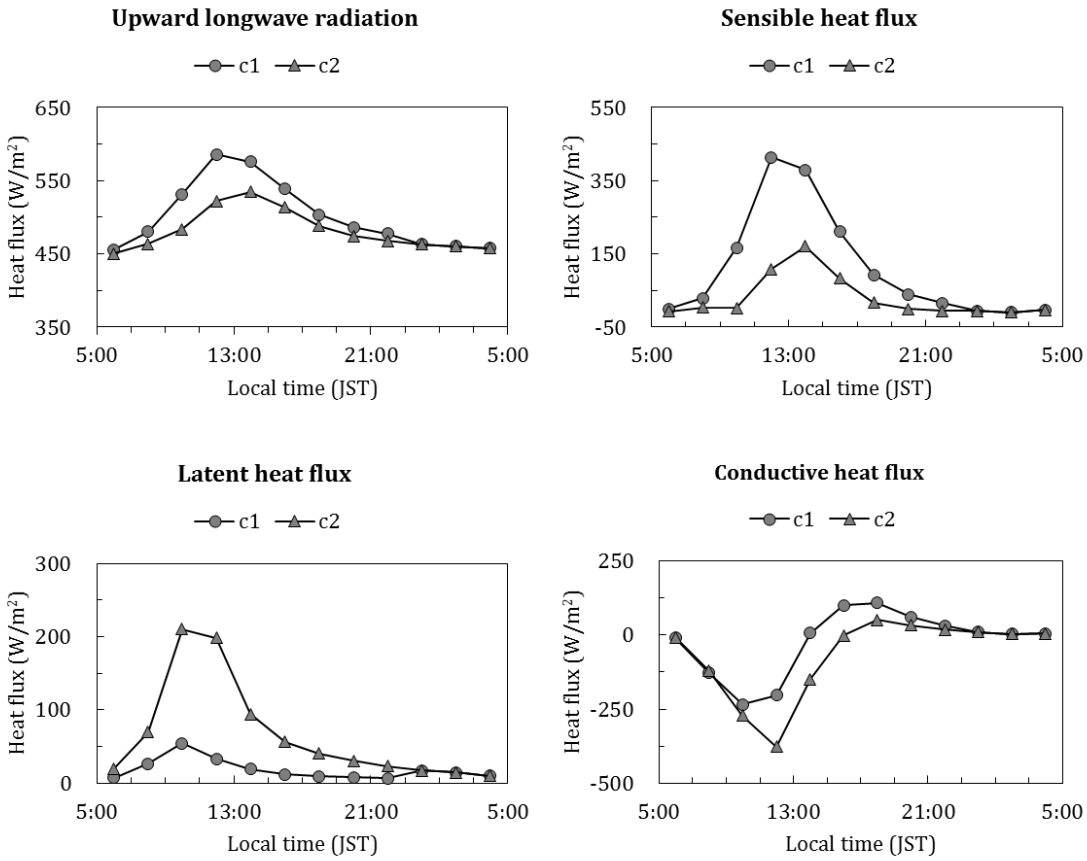


**Figure 50. A comparison of ground surface energy fluxes between $c_1$ and $c_2$.**

## 5.4. Conclusions

Using the coupled CFD-PT model it was proven that WRP as pavement material for main street can cause a decrease in ground surface temperature. This cooling is primarily due to the evaporation of water from WRP surfaces thereby causing an increase in latent heat flux. The increase in latent heat flux minimizes the difference between air temperature and surface temperature which leads to a decrease in sensible heat flux and longwave upward radiation. Other contributing factors to the cooling of WRP surface include shadowing effect, high albedo and lower thermal conductivity. The cooling of ground surface eventually leads to air temperature decrease. Although other factors such as vortex formation also contribute this decrease, it is proportional to the degree of surface temperature decrease.

# 6. REFERENCES

Aoyagi, T., Kayaba, N., & Seino, N. (2012). Numerical Simulation of the surface air temperature change caused by increases of urban area, anthropogenic heat, and building aspect ratio in the Kanto-Koshin area. Journal of the Meteorological Society of Japan, 90B, 11–31.

Asaeda, T., & Ca, V. T. (1993). The subsurface transport of heat and moisture and its effect on the environment: a numerical model. Boundary-Layer Meteorology, 65, 159–179.

Asaeda, T., & Ca, V. T. (2000). Characteristics of permeable pavement during hot summer weather and impact on the thermal environment. Building and Environment, 35(4), 363–375.

Asaeda, T., Ca, V. T., & Wake, A. (1996). Heat storage of pavement and its effect on the lower atmosphere. Atmospheric Environment, 30(3), 413–427.

Baik, J.-J., Kim, J., & Fernando, H. J. S. (2003). A CFD model for simulating urban flow and dispersion. Journal of Applied Meteorology, 42(11), 1636–1648.

Bartak, M., Beausoleil-Morrison, I., Clarke, J. A., Denev, J., Drkal, F., Lain, M. & Stankov, P. (2002). Integrating CFD and building simulation. Building and Environment, 37(8–9), 865–871.

Blocken, B., Stathopoulos, T., & Carmeliet, J. (2007). CFD simulation of the atmospheric boundary layer: wall function problems. Atmospheric Environment, 41(2), 238–252.

Bureau of the Environment Tokyo Metropolitan Government. (2005). Guidelines for heat island control measures (Vol. Summary Ed). https://www.kankyo.metro.tokyo.jp/en/attachement/heat_island.pdf, accessed September 2013.

Böer, K. W. (2001). Self-cooling of photovoltaic cells when power is drawn. Physica Status Solidi (A) Applied Research, 184(1), 201–209.

Cao, L., Li, P., Zhang, L., & Chen, T. (2002). Remote sensing image-based analysis of the relationship between urban heat island and vegetation fraction. The International Archives of Photogrammetry, Remote Sensing and Spatial Information Sciences, 37, 1379–1384.

Chang, C. R., Li, M. H., & Chang, S. D. (2007). A preliminary study on the local cool-island intensity of Taipei city parks. Landscape and Urban Planning, 80(4), 386–395.

Chen, X. L., Zhao, H. M., Li, P. X., & Yin, Z. Y. (2006). Remote sensing image-based analysis of the relationship between urban heat island and land use cover changes. Remote Sensing of Environment, 104(2), 133–146.

Chow, W. T. L., & Roth, M. (2006). Temporal dynamics of the urban heat island of Singapore. International Journal of Climatology, 26, 2243–2260.

Cortes, A., Kondo, A., Shimadera, H. & Sota, H. (2016). Numerical evaluation of the transport of heat and moisture in water retentive pavement. Journal of Japan Society for Atmospheric Environment 51, 103–110.

Cortes, A., Murashita, Y., Matsuo, T., Kondo, A., Shimadera, H., & Inoue, Y. (2015). Numerical evaluation of the effect of photovoltaic cell installation on urban thermal environment. Sustainable Cities and Society, 19, 250–258.

Costanzo, V., Evola, G., & Marletta, L. (2015). Energy savings in buildings or UHI mitigation? Comparison between green roofs and cool roofs. Energy and Buildings.

Daamen, C. C., & Simmonds, L. P. (1996). Measurement of evaporation from bare soil and its estimation using surface resistance. Water Resources Research, 32(5), 1393–1402.

Dimoudi, A., Zoras, S., Kantzioura, A., Stogiannou, X., Kosmopoulos, P., & Pallas, C. (2014). Use of cool materials and other bioclimatic interventions in outdoor places in order to mitigate the urban heat island in a medium size city in Greece. Sustainable Cities and Society, 13, 89–96.

Elsayed, I. S. M. (2012). A study on the urban heat island of the city of Kuala Lumpur, Malaysia. Journal of King Abdulaziz University, 23(2), 121–134.

Fintikakis, N., Gaitani, N., Santamouris, M., Assimakopoulos, M., Assimakopoulos, D. N., Fintikaki, M. & Doumas, P. (2011). Bioclimatic design of open public spaces in the historic centre of Tirana, Albania. Sustainable Cities and Society, 1(1), 54–62.

Genchi, Y., Ishisaki, M., Ohashi, Y., Kikegawa, Y., Takahashi, H., & Inaba, A. (2003). Impacts of large-scale photovoltaic panel installation on the heat island effect in Tokyo. Proceedings of the Fifth International Conference on Urban Climate (Lodz), Poland, 1–4.

Georgakis, C., Zoras, S., & Santamouris, M. (2014). Studying the effect of "cool" coatings in street urban canyons and its potential as a heat island mitigation technique. Sustainable Cities and Society, 13, 20–31.

Golden, J. S. & Kaloush, K.E. (2006). Mesoscale and microscale evaluation of surface pavement impacts on the urban heat island effects. International Journal of Pavement Engineering 7, 37–52.

Google Earth 7.1.5.1557 (2015). Esaka 34°45'29.29" N, 135°29'50.16" E, Elevation 395 m. 3D Buildings data layer, accessed February 2016.

Guntor, N. A., Din, M. Md., M.F., Ponraj, M. & Iwao, K. (2014). Thermal performance of developed coating material as cool pavement material for tropical regions. Journal of Materials in Civil Engineering 26, 755–760.

Hathway, E. A., & Sharples, S. (2012). The interaction of rivers and urban form in mitigating the urban heat island effect: a UK case study. Building and Environment, 58, 14–22.

He, B. J., Yang, L., & Ye, M. (2014). Strategies for creating good wind environment around Chinese residences. Sustainable Cities and Society, 10, 174–183.

Ikejima, K., Akira, K., & Akikazu, K. (2011). The 24-h unsteady analysis of air flow and temperature in a real city by high-speed radiation calculation method. Building and Environment, 46(8), 1632–1638.

Japan Meteorological Agency: Database and materials (2014). http://www.data.jma.go.jp/obd/stats/etrn/view/10min_a1.php?prec_no=62&block_no=0602&year=2014&month=10&day=29&view=p1, accessed November 2015 [*in Japanese*].

Jauregui, E. (1997). Heat island development in Mexico City. Atmospheric Environment, 31(22), 3821–3831.

Karasawa, A., Fujita, H., & Takamori, T. (2006). Study of effect of water-retentive pavement in controlling the temperature rise of surface. Concrete Journal, 44(7), 9–16.

Kawakami, A., & Kubo, K. (2008). Development of a cool pavement for mitigating the urban heat island effect in japan water-retention pavement heat-shield pavement. International Society for Asphalt Pavements Conference 2008 (pp. 1–12).

Kim, Y., & Baik, J. (2005). Spatial and temporal structure of the urban heat island in Seoul. American Meteorological Society, 44(1973), 591–605.

Kinoshita, S., Yoshida, A., & Okuno, N. (2012). Evaporation performance analysis for water-retentive material based on outdoor heat-budget and transport properties. Journal of Heat Island Institute International, 7, 222–230.

Kolokotroni, M., Giannitsaris, I., & Watkins, R. (2006). The effect of the London urban heat island on building summer cooling demand and night ventilation strategies. Solar Energy, 80(4), 383–392.

Kondo, J., Saigusa, N. & Sato, T. (1990). A parameterization of evaporation from bare soil surfaces. Journal of Applied Meteorology, 29, 385–389.

Kubo, K., Kido, H., & Ito, M. (2006). Study on pavement technologies to mitigate the heat island effect and their effectiveness. 10th International Conference on Asphalt Pavements, 223–232.

Kłysik, K., & Fortuniak, K. (1999). Temporal and spatial characteristics of the urban heat island of Łódź, Poland. Atmospheric Environment, 33 (1999), 3885–3895.

Lemonsu, A., & Masson, V. (2002). Simulation of a summer urban breeze over Paris. Boundary-Layer Meteorology, 104(3), 463–490.

Li, D., Bou-Zeid, E., & Oppenheimer, M. (2014). The effectiveness of cool and green roofs as urban heat island mitigation strategies. Environmental Research Letters, 9(5), 1–16.

Li, H., Harvey, J. T., Holland, T. J., & Kayhanian, M. (2013). Corrigendum: the use of reflective and permeable pavements as a potential practice for heat island mitigation and stormwater management. Environmental Research Letters, 8, 1–14.

Macapinlac, O. T. (2011). A role play simulation of urban heat island (UHI) intensity and mitigation. In Asia Geospatial Forum (pp. 1–15).

Maragkogiannis, K., Kolokotsa, D., Maravelakis, E., & Konstantaras, A. (2014). Combining terrestrial laser scanning and computational fluid dynamics for the study of the urban thermal environment. Sustainable Cities and Society, 13, 207–216.

Masson, V., Bonhomme, M., Salagnac, J.L., Briottet, X., & Lemonsu, A. (2014). Solar panels reduce both global warming and urban heat island. Frontiers in Environmental Science, 2(June), 1–10.

Mendonca, F. (2009). Urban heat and urban cool islands: influences of vegetation and soil surface in some cities, southern Brazil. In The Seventh International Conference on Urban Climate (pp. 3–6).

Ministry of Environment. Inter-ministry coordination committee to mitigate urban heat island: outline of the policy framework to reduce urban heat island effects, http://www.env.go.jp/en/air/heat/heatisland.pdf, accessed December 2014.

Ministry of Land, Infrastructure, Transport and Tourism: Road Bureau. http://www.mlit.go.jp/road/road _e/q5_technology.html, accessed February 2016.

Mirzaei, P. a., & Haghighat, F. (2010). Approaches to study urban heat island – abilities and limitations. Building and Environment, 45(10), 2192–2201.

Misaka, I., Narita, K., & Yokoyama, H. (2009). Evaluation of evaporation ability of the system for mitigating urban heat island. 7th International Conference on Urban Climate, (July), 2–5.

Misaka, I., Narita, K., Watanuki, R., Yokoyama, H., Yamaguchi, T., & Ishii, K. (2005). A study of mitigating urban heat island by water retentive pavement system with thermo-sensitive hydro gel. Annual Report of the Tokyo Metropolitan Research Institute for Environmental Protection, 35, 19–24.

Miyatake, N., Sakano, N., Murakami, S., Suna, S., Suzue, T., & Hirao, T. (2011). Comparison of the changes in temperatures among rural, urban and metropolitan areas around the Inland Sea in Japan. Environmental Monitoring and Assessment, 181(1-4), 525–30.

Mochida, A., Murakami, S., Ojima, T., Kim, S., Ooka, R., & Sugiyama, H. (1997). CFD analysis of mesoscale climate in the Greater Tokyo area. Journal of Wind Engineering and Industrial Aerodynamics, 67-68, 459–477.

Montavez, J. P., Rodriguez, A., & Jimenez, J. I. (2000). A study of the urban heat island of Granada. International Journal of Climatology, 20(8), 899–911.

Mualem, Y. (1976). A new model for predicting the hydraulic conductivity of unsaturated porous media. Water Resource Research 3, 513–522.

Nakayama, T., & Fujita, T. (2010). Cooling effect of water-holding pavements made of new materials on water and heat budgets in urban areas. Landscape and Urban Planning, 96(2), 57–67.

Nunez, M., & Oke, T. R. (1977). The energy balance of an urban canyon. Journal of Applied Meteorology, 16, 11–19.

Ohashi, Y., Genchi, Y., Kondo, H., Kikegawa, Y., Yoshikado, H., & Hirano, Y. (2007). Influence of air-conditioning waste heat on air temperature in Tokyo during summer: numerical experiments using an urban canopy model coupled with a building energy model. Journal of Applied Meteorology and Climatology, 46, 66–81.

Ohashi, Y., Ihara, T., Kikegawa, Y., & Sugiyama, N. (2015). Numerical simulations of influence of heat island countermeasures on outdoor human heat stress in the 23 wards of Tokyo, Japan. Energy and Buildings 114, 104–111.

Oke, T. (1973). City size and the urban heat island. Atmospheric Environment Pergamon Press, 7, 769–779.

Oke, T. R. (1982). The energetic basis of the urban heat island. Quarterly Journal of the Royal Meteorological Society, 108(455), 1–24.

Onishi, A., Cao, X., Ito, T., Shi, F., & Imura, H. (2010). Evaluating the potential for urban heat-island mitigation by greening parking lots. Urban Forestry and Urban Greening, 9(4), 323–332.

Ono, M. (2013). Heat stroke and the thermal Environment. Japan Medical Association Journal, 141(2), 199–205.

Pantakar, S.V. (1980). Numerical heat transfer and fluid flow. Taylor & Francis, New York, pp. 126-131.

Peng, L., Nielsen, P. V., Wang, X., Sadrizadeh, S., Liu, L., & Li, Y. (2016). Possible user-dependent CFD predictions of transitional flow in building ventilation. Building and Environment, 99, 130–141.

Priyadarsini, R., Hien, W. N., & David, C. K. W. (2008). Microclimatic modeling of the urban thermal environment of Singapore to mitigate urban heat island. Solar Energy, 82(8), 727–745.

Ramponi, R., & Blocken, B. (2012). CFD simulation of cross-ventilation for a generic isolated building: Impact of computational parameters. Building and Environment, 53, 34–48.

Rizwan, A. M., Dennis, L. Y. C., & Liu, C. (2008). A review on the generation, determination and mitigation of Urban Heat Island. Journal of Environmental Sciences, 20(1), 120–128.

Santamouris, M. (2013). Using cool pavements as a mitigation strategy to fight urban heat island – A review of the actual developments. Renewable and Sustainable Energy Reviews, 26, 224–240.

Shigeta, Y., Ohashi, Y., & Tsukamoto, O. (2009). Urban cool island in daytime — analysis by using thermal image and air temperature measurements. The Seventh International Conference on Urban Climate, (July), 3–6.

Shimadera, H., Kondo, A., Shrestha, K. L., Kitaoka, K. & Inoue, Y. (2015). Numerical evaluation of the impact of urbanization on summertime precipitation in Osaka, Japan. Advances in Meteorology 2015, 1–11.

Skamarock, W. C. & Klemp, J. B. (2008). A time-split nonhydrostatic atmospheric model for weather research and forecasting applications. Journal of Computational Physics 227, 3465–3485.

Stavrakakis, G. M., Tzanaki, E., Genetzaki, V. I., Anagnostakis, G., Galetakis, G., & Grigorakis, E. (2012). A computational methodology for effective bioclimatic-design applications in the urban environment. Sustainable Cities and Society, 4, 41–57.

Steinecke, K. (1999). Urban climatological studies in the Reykjavik subarctic environment, Iceland. In Atmospheric Environment (Vol. 33, pp. 4157–4162). doi:10.1016/S1352-2310 (99)00158-2.

Suita City: environmental information, data collection and business analysis. http://www.city.suita.osaka.jp/var/rev0/0090/2831/201276174559.pdf, accessed on February 2016. [*in Japanese*]

Taha, H. (1997). Urban climates and heat islands: albedo, evapotranspiration, and anthropogenic heat. Energy and Buildings, 25(2), 99–103.

Taha, H. (2013). The potential for air-temperature impact from large-scale deployment of solar photovoltaic arrays in urban areas. Solar Energy, 91, 358–367.

Takahashi, K., & Yabuta, K. (2009). Road temperature mitigation effect of “road cool,” a water-retentive material using blast furnace slag. JFE Technical Report, 13(13), 58–62.

Takahashi, K., Yoshida, H., Tanaka, Y., Aotake, N., & Wang, F. (2004). Measurement of thermal environment in Kyoto city and its prediction by CFD simulation. Energy and Buildings, 36(8), 771–779.

Takebayashi, H., & Moriyama, M. (2012). Study on surface heat budget of various pavements for urban heat island mitigation. Advances in Materials Science and Engineering, 2012.

Takebayashi, H., Kimura, Y., & Kyogoku, S. (2014). Study on the appropriate selection of urban heat island measure technologies to urban block properties. Sustainable Cities and Society, 13, 217–222.

Tian, W., Wang, Y., Ren, J., & Zhu, L. (2007a). Effect of urban climate on building integrated photovoltaics performance. Energy Conversion and Management, 48(1), 1–8.

Tian, W., Wang, Y., Xie, Y., Wu, D., Zhu, L., & Ren, J. (2007b). Effect of building integrated photovoltaics on microclimate of urban canopy layer. Building and Environment, 42(5), 1891–1901.

Tominaga, Y., & Stathopoulos, T. (2013). CFD simulation of near-field pollutant dispersion in the urban environment: a review of current modeling techniques. Atmospheric Environment. Atmospheric Environment, 79, 716–730.

Tominaga, Y., Sato, Y., & Sadohara, S. (2015). CFD simulations of the effect of evaporative cooling from water bodies in a micro-scale urban environment: Validation and application studies. Sustainable Cities and Society, 19, 259–270.

Ueno, T., & Tamaoki, K. (2009). Thermal characteristics of urban land cover by indoor lamp-irradiation experiment. The Seventh International Conference on Urban Climate, (July), 1–4.

Voogt, J. A. How researchers measure urban heat island. University of Western Ontario.https://www.epa.gov/sites/production/files/2014-07/documents/epa_how_to_measure_a_uhi.pdf, accessed June 2013.

Voogt, J. A., & Oke, T. R. (2003). Thermal remote sensing of urban climates. Remote Sensing of Environment, 86 (3), 370–384.

Wan, W., & Hien, W. (2012). A study on the effectiveness of heat mitigating pavement coatings in Singapore. Journal of Heat Island Institute International, 7(2), 238–247.

Wang, X., & Li, Y. (2016). Predicting urban heat island circulation using CFD. Building and

Environment, 99, 82–97.

Wang, Y., Berardi, U., & Akbari, H. (2015). Comparing the effects of urban heat island mitigation strategies for Toronto, Canada. Energy and Buildings.

Wang, Y., Tian, W., Ren, J., Zhu, L., & Wang, Q. (2006). Influence of a building's integrated-photovoltaics on heating and cooling loads. Applied Energy, 83(9), 989–1003.

Yamagata, H., Nasu, M., Yoshizawa, M., Miyamoto, A. & Minamiyama, M. (2008). Heat island mitigation using water retentive pavement sprinkled with reclaimed wastewater. Water Science and Technology 57, 763–771.

Yamamoto, T., Maki, T., & Honda, T. (2006). Discussions on assessment and quality standards of water-retaining concrete block. 8th International Conference on Concrete Block Paving, (November 6-8), 253–262.

Yamamoto, Y. (2005). Measures to mitigate urban heat island. Environmental and Energy Research Unit. Quarterly Review (Vol. 18).

Zhai, Z. J., & Chen, Q. Y. (2005). Performance of coupled building energy and CFD simulations. Energy and Buildings, 37(4), 333–344.

Zhou, Y., & Shepherd, J. M. (2010). Atlanta's urban heat island under extreme heat conditions and potential mitigation strategies. Natural Hazards, 52(3), 639–668.

Zoras, S., Tsermentselis, A., Kosmopoulos, P., & Dimoudi, A. (2014). Evaluation of the application of cool materials in urban spaces: A case study in the center of Florina. Sustainable Cities and Society, 13, 223–229.

van Genuchten, M. (1980). A closed-form equation for predicting the hydraulic conductivity of unsaturated soils. Soil Science Society of America Journal 44, 892–898.

# 7. PUBLICATIONS

**Peer-reviewed publications**

1. Cortes, A., Murashita, Y., Matsuo, T., Kondo, A., Shimadera, H., & Inoue, Y. (2015). Numerical evaluation of the effect of photovoltaic cell installation on urban thermal environment. Sustainable Cities and Society, 19, 250–258.
2. Cortes, A., Kondo, A., Shimadera, H., & Sota, H. (2016). Numerical evaluation of the transport of heat and moisture in water retentive pavement. Journal of Japan Society for Atmospheric Environment, 51(2), 103–110.
3. Cortes, A., Shimadera, H., Matsuo, T., & Kondo, A. (2016) Evaluation of water retentive pavement as mitigation strategy for urban heat island using computational fluid dynamics. Asian Journal of Atmospheric Environment, [*under revision as of July 29, 2016*].

**Conference proceedings and presentations**

(**presenter)

1. Aiza Cortes**, Hidetaka Kogama, Akira Kondo, Hikari Shimadera, Yoshio Inoue. Surface moisture availability of different pavement materials. Kinki Branch of the Society of Heat, Air-Conditioning and Sanitary Engineers of Japan. December 2013 at Osaka University – Nakanoshima Center, Osaka, Japan.
2. Aiza Cortes**, Yuji Murashita, Akira Kondo, Hikari Shimadera, Yoshio Inoue. Modeling of the thermal environment of Osaka City and evaluation on the effect of photovoltaic cell installation by CFD analysis. The 7th Japanese-German meeting on urban climatology. October 2014 at Leibniz University of Hanover, Hannover, Germany.
3. Aiza Cortes**, Hikari Shimadera, Tomohito Matsuo, Akira Kondo. Numerical evaluation of the effect of photovoltaic cell installation on urban thermal environment. The 56th Annual Meeting of Atmospheric Environment Society. September 2015 at Waseda University, Tokyo, Japan.